STUDIES ON GROWTH AND PROMINENT POLARIZATION PROPERTIES OF $SrTiO_3$ THIN FILMS

Mamoru IWABUCHI

January, 1997

Osaka University, Japan

STUDIES ON GROWTH AND PROMINENT POLARIZATION PROPERTIES OF $SrTiO_3$ THIN FILMS

$SrTiO_3$薄膜の作製とその高誘電特性に関する研究

Mamoru IWABUCHI

巖淵　守

January, 1997

Osaka University

Faculty of Engineering Science
Toyonaka, Osaka, Japan

To My Parents

愛する父、母へ

STUDIES ON GROWTH AND PROMINENT POLARIZATION PROPERTIES OF $SrTiO_3$ THIN FILMS

Mamoru IWABUCHI

January, 1997

ABSTRACT

For the purpose of furthering the electronics applications of a highly polarizable material, $SrTiO_3$ (STO), thin film fabrication and investigation of its optical and electrical properties were carried out, and the possibility of obtaining new materials with higher polarizability was pursued on the basis of the obtained results.

Correlation between the structure and the polarization properties of STO was investigated from the microscopic view with the representative cases in the thin film fabrication: STO contains oxygen vacancies and unintentional structures aside from perovskite due to insufficient oxidation and nonstoichiometry, respectively. Stable structures of these two cases were calculated by considering the two-body central force interatomic potential. The permittivities of these obtained STO structures were calculated successively with the corrections of the local field and the ease of each ion dislocation in the interatomic potential. The calculated results of these indicated that the polarization property is degraded as the STO structure diverts from the ideal perovskite. Furthermore, the discussion about the ionicity was carried out in an unprecedented manner through the results of this work. It

disclosed that the bonds in the perovskite structure are not completely ionic in the least, but covalent to a large extent. This is not inconsistent with the result of the improved calculation which employs the theory of molecular orbitals, and proposed the prospect of further investigation of polarization properties in the future. It eventually became clear that there is an intimate relationship between the structure of STO crystals and their polarization properties even in the microscopic view, and the perovskite structure holds the key to the excellent polarizability of the ideal STO crystal.

For the practical STO thin film fabrication, the eclipse method, an innovative technique which uses a shadow mask placed between the target and the substrate, was proposed in place of the conventional laser ablation method which has the intrinsic problem of particles and/or droplets. Despite the simplicity of the eclipse method, it completely solved the problem and led to a remarkable improvement in the surface smoothness of the STO thin films. Moreover, it led to a striking enhancement of success probability of the capacitance observation. Epitaxy of the grown STO thin films was examined by the X-ray diffraction (XRD) and the reflection high-energy electron diffraction (RHEED) methods. Although the STO thin film grown by the eclipse method on (100)Pt did not possess the long-range lattice ordering, it showed the fine (100)-oriented epitaxial growth. On the other hand, both of the STO thin films grown by the rf magnetron sputtering on (100) and (111)-oriented Pt films included a small amount of (110)-oriented composite. However, the STO thin film on (100)Pt substrate exhibited an almost complete streak pattern, which indicated the two-dimensional growth in which long-distance ordering was kept.

Optical properties of the grown STO thin films were investigated by the reflection absorption spectroscopy (RAS), which is one of the most powerful techniques for thin film measurement. The interfacial information between the Pt substrates and the STO films was obtained by reducing the film thickness of the STOs. The observed spectra suggested the existence of the degraded layer on the interface. Electrical properties of the grown STO thin films were investigated by the measurement of the capacitance-voltage curves, and they indicated the internal electric field dependence of permittivity which became most with zero internal field. The permittivity of the STO thin films reached as high as $370\varepsilon_0$ at room temperature. By means of phenomenological treatment, it was disclosed that the induced charge could reach ~10^{14} cm^{-2}, which are two orders higher than in familiar semiconductors. In addition, it became clear that the band diagram, which has no space charge, is appropriate

for the description of the Cr/(100)STO/Pt metal-insulator-metal structure.

Prospect for the higher polarization properties was examined with the genetic algorithm. Two approaches for the creation of new materials were proposed according to the features of the obtained highly polarizable materials. The first one is the realization of a structure in which ionic polarizations enhance one another through the positive-feedback-like mechanism as in the perovskite structure of STO. The second one is the realization of a structure in which it is easy for ions to dislocate on the axes parallel to the applied electric field. It was indicated that such desirable structures may be accomplished with asymmetric crystal structures rather than with symmetric and uniform crystal structures.

ACKNOWLEDGEMENTS

I would like to express my sincere gratitude to Professor Takeshi Kobayashi for his thoughtful and helpful advice and encouragements throughout the course of this thesis work. This thesis could not have been completed without his continuous suggestions and support. I gratefully acknowledge Prof. K. Nishihara at the Institute of Laser Engineering, Osaka University, Prof. M. Okuyama, and Prof. H. Okamoto for their careful reading of the manuscript and fruitful discussions. It is hard to adequately express my gratitude to Prof. A. Hashimoto for his quite helpful suggestions and comments, in particular for Chapter 5 of this thesis. I also wish to express thanks to Prof. emeritus Y. Hamakawa at Ritsumeikan University, Prof. S. Yamamoto, Prof. K. Gamo, Prof. T. Kobayashi, Prof. M. Takai, and Prof. Y. Okamura for their valuable teaching during the course of this thesis study.

This work has benefited enormously from the thoughtful comments and criticisms of Dr. K. Sakuta, Dr. T. Fujii, Dr. T. Maki, Mr. M. Kamishiro, Mr. Y. Sakaguchi, and Mr. X. Fang. I am also indebted to my colleagues, Mr. M. Tachiki, Mr. Y. Yun, Mr. E. Morita, Mr. H. Kawamura, Mr. K. Yamamuro, Mr. K. Sugahara, Mr. T. Yamamoto, Mr. K. Yamada, Mr. M. Noda, Mr. Y. Kurokawa, and Mr. Y. Shirakawa, for their useful advise and discussions.

I would like express special appreciation to Mr. T. Ashida at Toyota Motor Corporation, Mr. K. Okumura at Sharp Corporation, Mr. H. Mizushima at Marubeni Corporation, and Mr. T. Kashiwai who have greatly contributed to this thesis work in partnership with the author. I am also thankful to Mr. K. Matsui at Matsushita Electric Industrial Co., Ltd., Mr. T. Hirano at Sony Corporation, Mr. S. Arisaka at Sumitomo Electric Industries, Ltd., Mr. T. Ohara at Sumitomo Metal Industries, Ltd., Mr. T. H. Kim at Mitsubishi Electric Corporation, Mr. G. L. Hou at Satosen Corporation, Mr. K. Kinoshita at Toyota Motor Corporation, Mr. H. Kobayashi at Toshiba Corporation, Mr. T. Ariki at Mitsubishi Electric Corporation, Mr. S. Shikama at Mitsubishi Electric Corporation, Mr. H. Ishibashi at Matsushita Electric Industrial Co., Ltd., Mr. M. Taga at Sharp Corporation, Mr. N. Izumi at Rohm Co., Ltd., Mr. S. Suzuki at Matsushita Electric Industrial Co., Ltd., and all other people who were and are members of the Kobayashi Laboratory for their considerate advice and invaluable contributions.

This work was partly supported by a Grant-in-Aid for Scientific Research from the Ministry of Education, Science and Culture. In addition, the author was financially supported by the Support Center for Advanced Telecommunication Technology Research (SCAT) throughout the thesis work. I here would like to express my gratitude to these foundations.

I wish to express my special thanks to Mr. W. S. Kolahi, Mr. Y. Ikezumi, Mr. Y. Imura, Mr. Y. Adachi, Ms. K. Kamei, and Ms. M. Tamada. I can never imagine the completion of this thesis without their profound and everlasting encouragements. I also would like to thank Mr. H. Matsumoto, Ms. Y. Kayanoki, and all other friends of mine. They always mentally supported and motivated me so much. Mr. O. D. J. Bayley and Ms. A. Harnish unsparingly gave me a lot of time and effort in correcting my English manuscript. I cannot help appreciating them for their great kindness and generosity.

Finally, I would like to express my greatest gratitude to my parents and sister, Hiroaki, Itsuko, and Hiroko, for their constant encouragement and limitless love.

Mamoru Iwabuchi

CONTENTS

Chapter 1
INTRODUCTION

1.1 Background and Significance of The Present Work

Recent improvements in semiconductor processing technologies have been truly striking. Owing to a large number of innovations, in particular in deposition techniques, fine thin films can be successfully fabricated today. These days, highly polarizable thin films are strongly requested for electronic and/or optical devices. Strontium titanate ($SrTiO_3$) is one of the promising materials for this use. Including this material, $SrTiO_3$, perovskite oxides are familiar for their high permittivities and as they have been intensively studied in pursuit of obtaining good thin films. The perovskite structure is prominent for ionic polarization, as ions enhance each other through mutual interaction. In this work, we shall focus on $SrTiO_3$ and discuss the relationship between its perovskite structure and prominent polarization properties from the point of view of aiming at the realization of quality thin films.

Let us first browse the features of $SrTiO_3$ by starting with the historical background of highly polarizable materials. In the 1920s, a ferroelectric material showing novel properties was first discovered. The first solid which was recognized to exhibit ferroelectric properties was Rochelle salt, the sodium-potassium salt of tartaric acid; it has the chemical formula $NaKC_4H_4O_6 \cdot 4H_2O$.[1] In 1935, Busch and Scherrer discovered ferroelectric properties in potassium dihydrophosphate, KH_2PO_4.[2] This is a typical example of the second group of ferroelectrics, consisting of dihydrogen phosphates and arsenates of the alkali metals. In 1942, Wainer and Salomon observed a number of anomalous dielectric properties of barium titanate ($BaTiO_3$). This brings us to the third group of ferroelectrics, the so-called oxygen octahedron group. This group chiefly consists of the perovskites with the general chemical formula ABO_3, where A is a di- or monovalent metal and B is a tetra- or pentavalent metal. $SrTiO_3$ has exactly this chemical formula and takes the main role of the present work as a representative of the third group.

$SrTiO_3$ has been studied intensively since the 1960s as an important dielectric material

in high-value capacitors. Through the investigation of its structure and electrical and optical properties, its characteristics have been made clear little by little as follows: $SrTiO_3$ is cubic in structure at room temperature, which consists of a small titanium atom at the center, and oxygen atoms in each of the six cube walls forming a cage around the titanium atom, and small strontium atoms at the cube corners.[3] As the temperature is reduced, the crystal structure becomes orthorhombic.[4] The pure crystal is an insulator at room temperature with a band gap of ~3.15 eV.[5, 6] Upon reduction by heating in a hydrogen atmosphere, the clear colorless insulating crystal becomes an *n*-type semiconductor, and the color shifts to a varying shade of blue as a result of the free-carrier absorption.[7] According to systematic studies of polarization properties, which were first started by Neville *et al.*,[8] $SrTiO_3$ has a permittivity as high as $330\varepsilon_0$ at room temperature, and the value reaches a few tens of thousands at cryogenic temperatures. Although $SrTiO_3$ has a Curie Point at 105 K, it doesn't show a ferroelectric transition. Moreover, its permittivity retains a quite high value which is independent of its temperature around liquid-helium temperatures. Barrett tried to explain this phenomenon by the expanded Slater theory with quantum statistics.[9, 10] At present, $SrTiO_3$ is known as a quantum paraelectric by an interpretation of soft-mode theory.[11, 12]

After a variety of deposition techniques have been established, $SrTiO_3$ draws more attention as a promising material for thin films. The recent reduction in cell size of electronic devices along with the improvements in processing technology required reducing the area of the planer storage capacitor area. This, in turn, made it necessary to increase the charge density on the capacitors to maintain adequate signal margins. $SrTiO_3$ is quite hopeful for this use in micro-size capacitors in Si large-scale integration (capacitance, C ~100 $fF/\mu m^2$ is required for 256 Mbits DRAM). Furthermore, owing to its high dielecricity and non-hysteretic polarizability even at low temperatures, $SrTiO_3$ has been extensively studied for application as the gate insulator of the metal-insulator-superconductor (or semiconductor) field effect transistors (MISFETs) with extremely high carrier concentration.[13-15]

The present research situation around $SrTiO_3$ is summarized in Fig. 1-1. In the figure, each subject is located beside others which it strongly relates to. In this work, firstly, the polarization properties of $SrTiO_3$ are discussed with an approach of molecular theory. It gives us a significant view that leads to a fruitful examination of $SrTiO_3$ thin films, and presents an instructive principle for high polarizability. Secondly, crystallographic, optical, and electrical

properties of $SrTiO_3$ fabricated thin films are investigated experimentally. Thirdly, the possibility for higher polarization properties is examined, where the preceding studies give us a probable guideline for creating a whole new material in the future. When all of the studies in this work are connected organically, they can contribute thoroughly to electronics in the next generation.

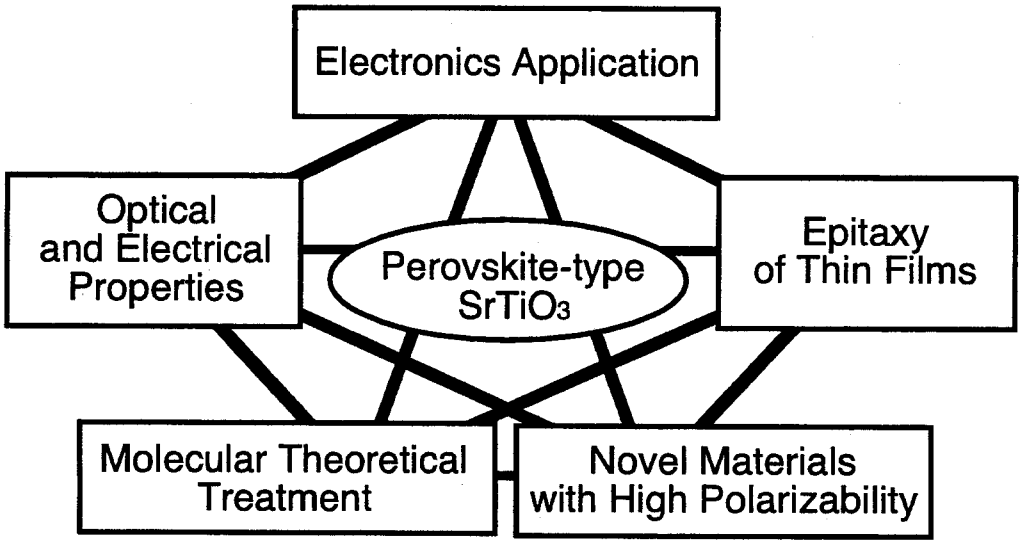

Fig. 1-1. The present research situation around $SrTiO_3$.

1.2 Thin Film Fabrication and Applications of Highly Polarizable Materials

There are presently a considerable number of reports focusing on the growth mechanism and device fabrication aspects of highly polarizable thin films for a variety of applications, such as nonvolatile memories,[16 - 18] ultrasonic sensors,[19] IR detectors,[20] and gate insulators of MISFET.[13 - 15] They work according to many specific properties of these materials, such as extremely high permittivity, spontaneous polarization, piezoelecricity, electrostriction, pyroelectricity, electrooptic effect, and optical second order harmonic

generation.

On the other hand, a number of deposition techniques have been used for producing ferro- and dielectric thin films so far.[21-31] They are rf sputtering, ion-beam sputtering, pulsed laser deposition (PLD) method, co-evaporation, sol-gel, chemical vapor deposition (CVD), and metal organic chemical vapor deposition (MOCVD), and so on. Each of them has some superiorities to the others. The CVD is, for example, expected to present advantages such as good step coverage, good thickness and composition uniformities over large-size wafers and a high deposition rate. The sol-gel method has a large potential for homogeneous distribution of elements at molecular level, ease of chemical composition control, high purity, low-temperature processing, coating of large surfaces, and hybridization of functionalities. The rf sputtering is a physical process operated under the non-equilibrium condition that produces high energy particles, and low temperature synthesis can be conducted because of the physical condition. The PLD technique has striking features such as high-rate growth, transfer of the composition from the target to film, separation of the heat source from the chamber, and capability of deposition in high O_2 ambient pressure in the chamber. Each method is still improving through optimization and/or additional functions. In this work, an innovative PLD technique using a shadow mask placed between the target and the substrate is proposed. It gives us flat surfaces of thin films, and overcomes the droplet problem that was the weakest point of the PLD method.

At present, we can see a lot of intensive work fabricating thin films of highly polarized materials, such as $BaTiO_3$, $PbTiO_3$, Pb(Zr, Ti)O_3 (PZT), (Pb, La)TiO_3 (PLT), (Pb, La)(Zr, Ti)O_3 (PLZT), $SrTiO_3$, KNO_3, $LiNbO_3$, and Li(Nb, Ta)O_3. Most of the useful materials, as represented above, have perovskite structure. Very recently, bismuth layered-structure ferroelectrics, $Sr_{m-3}Bi_4Ti_mO_{3m-3}$, occupy the attention for use of nonvolatile memory application on account of its endurance against fatigue. $SrTiO_3$ is indeed the fundamental element of the bismuth layered-structure ferroelectrics. It also follows that $SrTiO_3$ takes a fundamental and important position in the present research and development of highly polarizable thin films.

References

(1) J. Valasek, Phys. Rev. **17**, 475 (1921).

(2) G. Busch, and P. Scherrer, Naturwiss. **23**, 737 (1935).

(3) R. O. Bell and G. Rupprecht, Phys. Rev. **129**, 10 (1965).

(4) F. W. Lytle, J. Appl. Phys. **35**, 2212 (1964).

(5) H. W. Gandy, Phys. Rev. **113**, 795 (1959).

(6) V. E. Henrich, G. Dresselhaus, and H. J. Zeiger, Phys. Rev. **B17**, 4908 (1978).

(7) W. S. Baer, Phys. Rev. **144**, 734 (1966).

(8) R. C. Neville, B. Hoeneisen and C. A. Mead, J. Appl. Phys. **43**, 2124 (1972).

(9) J. C. Slater, Phys. Rev. **78**, 748 (1950).

(10) J. H. Barret, Phys. Rev. **86**, 118 (1952).

(11) K. A. Müller, and H. Burkard, Phys. Rev. **B19**, 3593 (1979).

(12) A. S. Chaves, F. C. S. Barreto, and L. A. A. Ribeiro, Phys. Rev. Lett. **37**, 618 (1976).

(13) J. Mannhart, D. G. Schlom, J. G. Bednorz, and K. A. Müller, Phys. Rev. Lett. **67**, 2099 (1991).

(14) K. Matsui, T. Awaji, T. Hirano, T. Fujii, K. Sakuta, and T. Kobayashi, Jpn. J. Appl. Phys. **31**, L1342 (1992).

(15) T. Ashida, S. Tomohisa, and T. Kobayashi, Jpn. J. Appl. Phys. **34**, L23 (1995).

(16) C. A. Paz de Araujo, J. D. Cuchiaro, M. C. Scott and L. D. McMillan, Int. Patent Publication No. WO93/12542 (1993).

(17) M. Tachiki, M. Matsutani, T. Fujii, Y. Sakaguchi and T. Kobayashi, Jpn. J. Appl. Phys. **34**, L1145 (1995).

(18) J. F. Scott and D. A. Paz de Araujo, Science **246**, 1400 (1989).

(19) M. Kojima, M. Sugawa, H. Sato, Y. Matsui, M. Okuyama, and Y. Hamakawa, Proc. 2nd Sensor Symp., Tokyo (Springer-Verlag, Tokyo, 1982) p.241.

(20) K. Iijima, I. Ueda, and K. Kugimiya, Jpn. J. Appl. Phys. **30**, 2149 (1991).

(21) M. Oksada, and K. Tominaga, J. Appl. Phys. **71**, 1955 (1992).

(22) G. Yi, Z. Wu, and M. Sayer, J. Appl. Phys. **64**, 2717 (1988).

(23) K. Sreenivas and M. Sayer, J. Appl. Phys. **64**, 1484 (1988).

(24) S. Matsubara, S. Miura, Y. Miyasaka, and N. Sohata, J. Appl. Phys. **66**, 5826 (1989).

(25) N. H. Cho, S. H. Nam, and H. G. Kim, J. Vac. Sci. Technol. **A 10**, 87 (1991).

(26) Z. Xu, H. K. Chae, M. H. Frey and D. A. Payne, Mater. Res. Soc. Symp. Proc. **271**, 339 (1992).

(27) B. S. Kwak, K. Zhang, E. P. Boyd and A. Erbil, J. Appl. Phys. **69**, 767 (1991).

(28) K. Iijima, T. Terashima, K. Yamamoto, K. Hirata, and Y. Bando, Appl. Phys. Lett. **56**, (1990) 527.

(29) M. G. Norton and C. B. Carter, J. Mater. Res. **5**, 2762 (1990).

(30) M. Iwabuchi, K. Kinoshita, H. Ishibashi, and T. Kobayashi, Jpn. J. Appl. Phys. **33**, L610 (1994).

(31) H. Yamaguchi, P. Y. Lesaicherre, T. Sakuma, Y. Miyasaka, A. Ishitani, and M. Yoshida, Jpn. J. Appl. Phys. **32**, 4096 (1993).

Chapter 2
ANALYSIS OF POLARIZATION PROPERTIES AND STRUCTURE OF $SrTiO_3$ CRYSTAL

2.1 Introduction

An ideal stoichiometric $SrTiO_3$ (STO) crystal has cubic perovskite structure at room temperature. STO thin films, on the other hand, have a possibility of containing various conformations due to internal stress or disparity from stoichiometry. Hirano *et al.* have reported that the sliding-in Sr-O plane occurred and the sublattice, perovskite STO in the vicinity of the sliding-in plane, was slightly distorted when non-stoichiometic thin films were grown.[1] Even when STO thin films are stoichiometric, it is conventionally indicated that STO thin films have a tendency to suffer oxygen deficiency and the lowered permittivity due to the lattice distortion with it.[2, 3] One of the physical processes, rf sputtering, uses the advantage of higher energy to realize the low temperature deposition. However, it might lead to unintentional structures inside thin films in several conditions.

In this chapter, microscopic investigation is given, which examines some cases: that the STO crystal causes oxygen deficiency, and that STO has other structures aside from perovskite. This investigation gives us a significant view that leads to a fruitful examination about STO thin films, and presents an instructive principle for the high polarizability discussed in the following chapters.

2.2 Polarization Properties of $SrTiO_3$ Thin Films

The STO crystal has been intensively studied for a long time because of its peculiar quantum paraelectricity. At present, these studies particularly lay on the fabrication and the

investigation of its thin films in pursuit of electronics applications. STO thin films can be fabricated by a number of ways: MOCVD, sol-gel, PLD method, reactive coevaporation, rf sputtering, ion beam sputtering, and so on.[4-10] We have to here take notice that once STO bulks are transformed into thin films through a deposition process, their dielectric properties are drastically changed, and the change, moreover, strongly depends on the atmosphere of the deposition process. In regard to the degradation of the polarization properties of thin films, this means not only the decrease of permittivity itself, but also the lessening of its field dependence, the fluctuation of the temperature at which the permittivity is maximum, and the diminution of break-down voltage. In this study, such degradations are observed in thin films fabricated by PLD method and rf sputtering. The experimental data trying to overcome the problem is discussed in Chapters 3 and 4. Let us summarize here the observed results which are suggestive for speculating about the phenomena that happen inside STO thin films.

1. Physical properties of grown thin films are different between the PLD method and rf sputtering even when the deposition temperatures are identical.
2. Atmospheric oxygen amount is quite an important factor as a deposition parameter in the techniques of both the PLD method and rf sputtering: It brings a complex variation of the mean energy of deposition particles and the amount of activated oxygen.
3. Deviating from the ideal perovskite structure, polarization properties are steeply degraded.[1]
4. There is a strong correlation between dielectric properties and optical phonon properties which reflects STO crystallinity.[11]

One of the most noteworthy points deduced from above is that the polarization properties of STO thin films are intensely dependent on their crystallinity regardless of the variety of deposition techniques. In the following parts, an approach based on molecular theory is undertaken to investigate how crystal structure inside STO thin films relates to their polarization properties.

2.3 Analysis of $SrTiO_3$ Crystal Structure

2.3.1 Calculation principle and parameters

When an STO crystal contains structural defects, its cubic perovskite structure transforms into another stable structure in this condition. The stable configuration has the maximum cohesive energy in each case. We realized the situation by using a computer simulation.

It is currently attempting to obtain detailed information of the STO structure inside thin films, such as how they form under what kind of deposition conditions. In this work, various trials are carried out, in which the initial conditions are supposed to have an abundant probability of existence. In regard to crystals which have the same composition, the most stable structure that has the maximum bond energy is chosen as a prospective one, and its dielectric property is primarily examined in the next section.

In terms of interatomic potential, two-body central force interatomic potential is concerned, which depends only on the positions of ion pairs i and j. So far, many potential models are proposed. The hard core model is the simplest that has an infinite potential inside the atomic radius shell and zero potential outside it. The Lennard-Johns model has been used for the description of an interaction among rear gas atoms. The Born-Mayer model is a good approximation of ionic crystals, and its potential is generally written in the form,

$$U(r_{ij}) = \frac{z_i z_j e^2}{r_{ij}} + U_{ij}^R, \tag{2-1}$$

where U^R is the short-range repulsion energy, and its origin is the electron cloud overlap, which primarily comes from Pauli's exclusion principle. Born and Mayer proposed the next term for it,

$$U_{ij}^R = A \exp\left(-\frac{r_{ij}}{\rho}\right). \tag{2-2}$$

Although the Born-Mayer model gives an agreeable approximation of alkali halide potential, it does not favorably explain the potential of perovskite materials. It is because ionic crystals which have the perovskite structure are not thoroughly ionic. The bonds inside the structure have a covalent feature to a certain extent as discussed later. Kawamura *et al.* proposed modified Born-Mayer-type repulsion with two parameters a and b. The repulsion is given by

$$U_{ij}(r_{ij}) = \frac{z_i z_j e^2}{r_{ij}} + f_0(b_i+b_j)\exp\left(\frac{a_i+a_j-r_{ij}}{b_i+b_j}\right). \quad (2\text{-}3)$$

The quantity f_0 is a constant, 6.9511×10^{-11}, for unit adaptation. The parameters a and b have been decided through trial and error in the molecular dynamics (MD) calculations.[12, 13] Computed data has compared those experimentally obtained at room temperature, and a number of crystals have desirably reached excellent correspondences to actual materials. In Table 2-1, the parameters for some ionic elements at room temperature are given which are taken from refs. (12) and (13).

Table 2-1 Potential parameters of ions.

	z	a	b
O	–2	1.629	0.080
F	–1	1.565	0.085
Na	1	1.260	0.080
Mg	2	1.161	0.080
Cl	–1	1.950	0.090
K	1	1.595	0.080
Ti	4	1.235	0.080
Sr	2	1.632	0.080

We have to consider the charge neutralization condition in which net charge of a crystal must be zero no matter what composition or structure the crystal takes. When STO crystal has a structural defect, its stoichiometry is destroyed in some cases. How is the charge neutralization condition maintained in these cases? Nowadays, the treatment of charge neutralization is still under dispute in the MD calculation of stable structures with defects. Although the mean-field approximation is crude, where charge loss due to ionic atom deficiency is compensated uniformly in the crystal, it has been popularly used and good

correspondences have been obtained to the true structures.[14] In the present work, the mean-field approximation is also employed. When oxygen deficiency arises in the crystal, for example, the charge of the deficient oxygen is distributed to each cation ion in proportion to its charge on the basis of the linear approximation.

As for the periodicity of calculated crystals, the periodic boundary condition is employed and each crystal is thought to have an infinite size. The introduction of the periodicity is essential because Coulomb force influences in long range. For the potential calculation of the infinite-sized crystals, Evjen and Ewald methods are generally applied. In this work, Evjen method is primarily used, and the precision is more than 4 digits.

2.3.2 Results and discussion of stable structures

Some already-known structures were examined at first. Their calculated and observed lattice constants are listed in Table 2-2.[15] We can conclude that agreeable data was obtained with which quantitative discussion can be explored. In other words, this calculation gives us properly stable structures of crystals.

Table 2-2 Calculated and observed lattice constants of ionic crystals.

	Calculated value (Å)	Experimental value (Å)
$SrTiO_3$	3.961	3.904
MgO	4.181	4.2112
NaCl	5.595	5.64056
KCl	6.320	6.29294
NaF	4.716	4.620
KF	5.477	5.347

Next, stable structures of nonstoichiometic STO are discussed. Here are noteworthy points: Though there are some ion distributions which have the same composition, there is only one distribution that is most stable, and the possibility of its existence inside the practical STO thin films is higher than others even when the depositions are carried out under physical processes. Let us examine them in a simple case. Two unit cells that have the same composition are shown in Fig. 2-1. Oxygen vacancies are located uniformly in the case I. On the other hand, they are located on planes in the case II. The calculated stable structure are as follows in Table 2-3, where the total energy is of $Sr_2Ti_2O_5$.

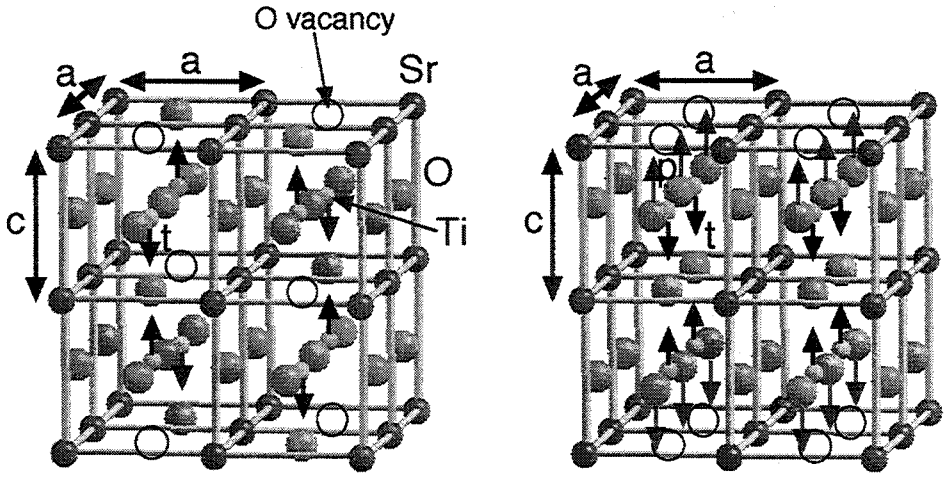

Fig. 2-1 Possible structures of $Sr_2Ti_2O_5$.

Table 2-3 Calculated crystallographic data of $Sr_2Ti_2O_5$.

	Lattice const. (Å)		Dislocation (Å)		Total energy ($\times 10^{-17}$ J)
	a	*c*	*t*	*p*	
Case I	4.004	4.082	0.168	----	−4.122
Case II	3.962	4.102	0.166	0.502	−3.882

The above data indicates that the bond energy of the second case is smaller than that of the first one, and hence, the second structure is an unlikely one. According to the second law of thermodynamics, each system approaches toward the state of larger entropy. Therefore, the vacancies in the oxygen-deficient STO crystals take places as uniformly as possible under the equilibrium condition. This uniform structure, the most stable one, could describe most favorably the properties of practical thin films. Hence, among the structures of the same composition and the same periodicity, the most stable structure is examined hereafter in this section. Unstable structures are discussed later in the Section 5.

Let us examine the case of STO crystals that have oxygen vacancies. According to the above discussions, three crystals consisting of one-oxygen-deficient 2×2×2 , 3×3×3 , and 4×4×4 STO lattices are examined as the most uniform structure among others which have the same compositions. The oxygen vacancy took place at a definite site inside the three types of the lattices. The chemical formula of the three crystals are $Sr_8Ti_8O_{23}$, $Sr_{27}Ti_{27}O_{80}$, and $Sr_{64}Ti_{64}O_{191}$. Figure 2-2 shows the ion distributions of the crystal consisting of one-oxygen-deficient 2×2×2 STO lattices before and after the introduction of the oxygen vacancy. The dislocation parameters symmetrically considered in the computation are also shown on the figure. One can see that larger dislocations occur in the vicinity of the midmost oxygen vacancy: The row of Ti-O ions next to the vacancy rumples greatly. Calculated structural data are summarized in Table 2-4.

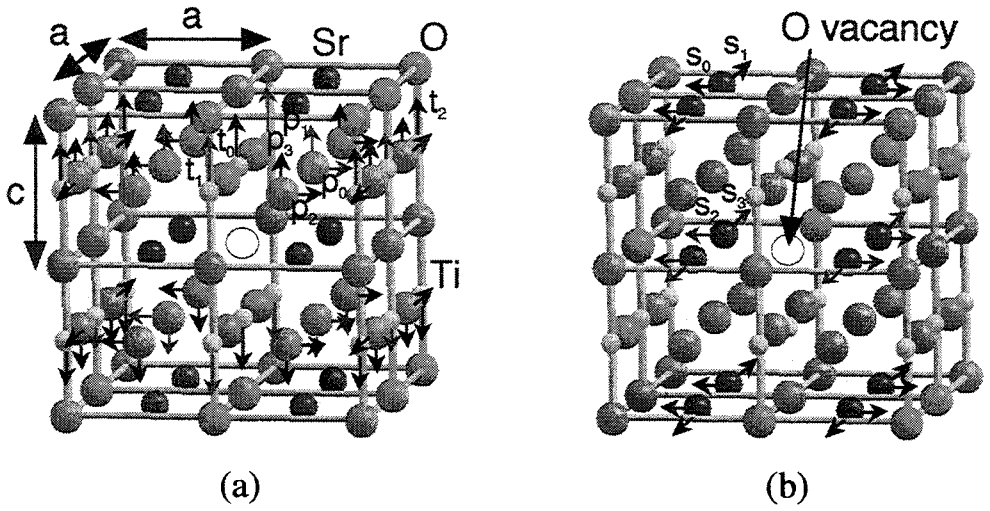

Fig. 2-2 Transformation of 2×2×2 STO lattices inside the crystal. (a) Before the introduction of an oxygen vacancy, and (b) after it.

Table 2-4 Calculated structural data of crystal consisting of one-oxygen-deficient 2×2×2 STO lattices.

Parameter		a	c	p_0	p_1	p_2	p_3
Length (Å)		3.967	4.003	0.079	0.262	0.005	0.026
	t_0	t_1	t_2	s_0	s_1	s_2	s_3
	0.196	0.033	0.018	0.122	0.122	0.200	0.200

The stable structures of crystals consisting of one-oxygen-deficient 3×3×3 and 4×4×4 STO lattices are calculated in the same manner. The number of the dislocation parameters we have to consider increase intensely in these cases. While it is 13 in all in the case of the 2×2×2 system, it is 35 of the 3×3×3 system, and 78 of the 4×4×4 system. Table 2-5 shows the calculated lattice constants of these crystals.

Table 2-5 Calculated lattice constants of one STO cell in the crystals consisting of one-oxygen-deficient 3×3×3 and 4×4×4 STO lattices, respectively.

	a (Å)	*c* (Å)
3×3×3 STO	3.963	3.974
4×4×4 STO	3.960	3.965

Now we can examine the lattice constant dependence on the amount of oxygen vacancies. In the preceding discussion, an oxygen is taken away from the midst of a cubic lump of STO lattices. However, the calculated stable structure with the oxygen vacancy is not cubic. It is because oxygen ions inside the perovskite-type structure do not locate at completely symmetric sites: When the nearest neighbor ions are strontium on a plane including an oxygen ion, for example, the oxygen is held up and down between titanium ions. When the size of the structural period is considerably larger than that taken above, the locations of the oxygen vacancies are dispersed more uniformly, that is, all of the six sites next to the titanium ions equally act as vacancy sites. In accordance with this idea, the observed lattice constants are thought to be approximately described by the mean value of the calculated lattice constants which are deduced by averaging a, b, and c-axis length of STO cells. Figure 2-3 presents the result, and we can conclude that the lattice tends to stretch due to the increase of oxygen vacancies.

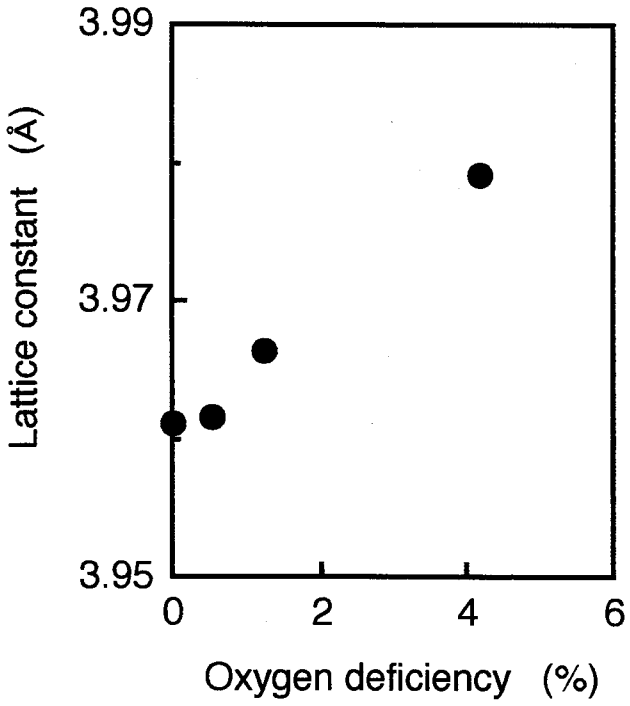

Fig. 2-3 Calculated lattice constant dependence on the amount of oxygen deficiency.

The result depicted in Fig. 2-3 is not inconsistent with the experimental phenomenon. In regard to STO thin films practically grown by the PLD method, the less the oxygen pressure in the deposition process was, the longer the lattice constant was.[2, 3] A more straightforward result of enlarged lattices came from the bulk $SrTiO_{3-\delta}$ fabricated by a reaction of Sr_2TiO_4, TiO, TiO_2 at 1500 °C.[16] We can now reach a conclusion that the reduction of the Coulomb force influences more than the decrease of the short-range repulsion force on the stabilization of the STO structures as oxygen deficiency takes place.

Next, let us discuss the case that STO has a different structure from the perovskite, sliding-in Sr-O plane. This idea comes from the well-known fact that the excess Sr very likely slides into STO cells in the form of a Sr-O plane,[17] resulting in crystal structure deformation. The resultant structure is $SrO(SrTiO_3)_n$, as depicted in Fig. 2-4, where the structure of $n = 3$. Calculated structural data is given in Table 2-6. The length of c_0 is 2.792 (Å) according to the experimental data deduced by X-ray diffraction,[1] and the calculated data shows a good agreement with it. Furthermore, the present calculation supports the experimental result that c_1 tends to shrink and becomes a little shorter than c_2.

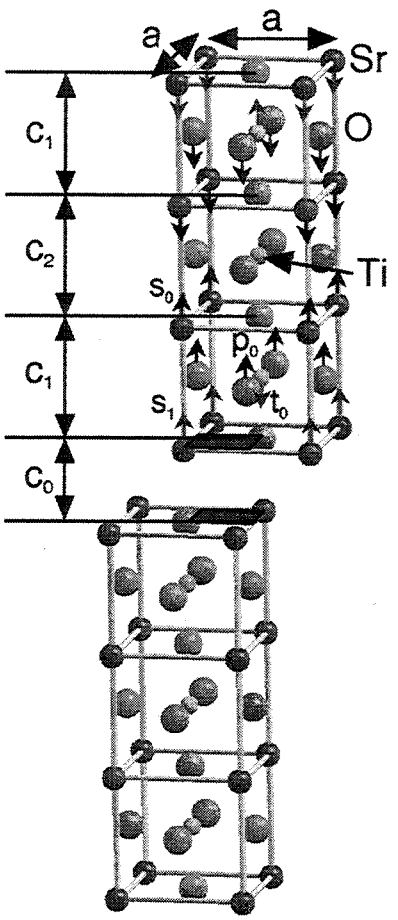

Fig. 2-4 Schematic drawing of the $SrO(SrTiO_3)_3$ unit cell.

Table 2-6 Calculated structural parameters of $SrO(SrTiO_3)_3$ unit cell.

Parameter	a	c_0	c_1	c_2
Length (Å)	3.952	2.523	3.965	3.967
p_0	t_0	s_0	s_1	
0.007	0.005	0.073	0.006	

2.4 Polarization Properties of Structures Related to $SrTiO_3$

2.4.1 Computational manner of permittivity

Permittivity is calculated by the summation of polarization which is induced by application of imaginary electric field to the stable structures obtained in the preceding section.

According to the Lorentz correction, we assume that the field acting on a dipole to polarize it is not $\boldsymbol{E}$, but is $\boldsymbol{E}+4\pi\boldsymbol{P}/3$ (in non-rationalized Gaussian units) when the ion distribution has cubic symmetry, where $\boldsymbol{E}$ is macroscopic electric field and $\boldsymbol{P}$ is induced polarization. Let us assume that the dipole moment induced in a volume v is α times the field, where α is the polarizability. We then have $\boldsymbol{P} = (\alpha/v)(\boldsymbol{E}+4\pi\boldsymbol{P}/3)$. The permittivity is deduced by

$$\varepsilon = 1 + \frac{4\pi P}{E} \tag{2-4}$$

in non-rationalized Gaussian units.

Let us now consider the permittivity of ideal STO crystal as an example. The imaginary electric field is supposed to be applied toward the z direction. The polarization of the Ti ions is defined as P_{Ti}, that of the Sr ions as P_{Sr}, that of oxygen of type a as P_{Oa}, and that associated with the two lattices of oxygen of type b as P_{Ob1} and P_{Ob2}. Type a oxygen is located next to the Ti ions parallel to the imaginary electric field (z direction), and type b oxygen is vertical to the field (x and y directions). By symmetry, we shall find that $P_{\mathrm{Ob1}} = P_{\mathrm{Ob2}}$. Then we have:

$$\begin{aligned}
\text{Field on Ti} &= E + 4\pi\left[\tfrac{1}{3}P_{\mathrm{Ti}} + \tfrac{1}{3}P_{\mathrm{Sr}} + \left(q + \tfrac{1}{3}\right)P_{\mathrm{Oa}} + \left(-\tfrac{1}{2}q + \tfrac{1}{3}\right)\left(P_{\mathrm{Ob1}} + P_{\mathrm{Ob2}}\right)\right], \\
\text{Field on Sr} &= E + 4\pi\left[\tfrac{1}{3}P_{\mathrm{Ti}} + \tfrac{1}{3}P_{\mathrm{Sr}} + \left(-p + \tfrac{1}{3}\right)P_{\mathrm{Oa}} + \left(\tfrac{1}{2}p + \tfrac{1}{3}\right)\left(P_{\mathrm{Ob1}} + P_{\mathrm{Ob2}}\right)\right], \\
\text{Field on Oa} &= E + 4\pi\left[\left(q + \tfrac{1}{3}\right)P_{\mathrm{Ti}} + \left(-p + \tfrac{1}{3}\right)P_{\mathrm{Sr}} + \tfrac{1}{3}P_{\mathrm{Oa}} + \left(\tfrac{1}{2}p + \tfrac{1}{3}\right)\left(P_{\mathrm{Ob1}} + P_{\mathrm{Ob2}}\right)\right], \\
\text{Field on Ob1} &= E + 4\pi\left[\left(-\tfrac{1}{2}q + \tfrac{1}{3}\right)P_{\mathrm{Ti}} + \left(\tfrac{1}{2}p + \tfrac{1}{3}\right)P_{\mathrm{Sr}} + \left(\tfrac{1}{2}p + \tfrac{1}{3}\right)P_{\mathrm{Oa}}\right. \\
&\qquad \left. + \tfrac{1}{3}P_{\mathrm{Ob1}} + \left(-p + \tfrac{1}{3}\right)P_{\mathrm{Ob2}}\right],
\end{aligned} \tag{2-5}$$

where $p = 8.668 / 4\pi = 0.690$, and $q = 30.084 / 4\pi = 2.394$ attributed to asymmetric ion distribution and calculated by the dipole interaction first introduced by Luttinger *et al.*[18] If the structure is not perovskite-type but rock-salt-type, p and q are zero. However, they are finite in the case of STO as in above equations, and therefore, the local field is quite different from $(4\pi/3)P$ because of the finite value of p and q due to the asymmetric configuration. We observe the very large factor q+1/3 by which the Ti ions and the type a oxygen ions interact on each other.

We can now set up simultaneous equations, starting with the fact that the polarization resulting from each type of ion equals the corresponding polarizability per unit volume, multiplied by the appropriate local field. Let the polarizabilities of Ti, Sr, and O be α_{Ti}, α_{Sr}, and α_O, respectively: α_{Ti} are summation of the electronic polarizability and ionic polarizability when we are dealing with low frequencies. Then we have

$$\begin{aligned} P_{Ti} &= (\alpha_{Ti}/v)\left(\text{field on Ti}\right), \\ P_{Sr} &= (\alpha_{Sr}/v)\left(\text{field on Sr}\right), \\ P_{Oa} &= (\alpha_O/v)\left(\text{field on } O_a\right), \\ P_{Ob1} &= (\alpha_O/v)\left(\text{field on } O_{b1}\right), \\ P_{Ob2} &= (\alpha_O/v)\left(\text{field on } O_{b2}\right), \end{aligned} \tag{2-6}$$

where the fields are as given in Eqs. (2-5). Solving the above simultaneous equations, each polarization is decided as functions of the macroscopic electric field, E. We can also solve for the permittivity which we get from the sum of all the polarizations divided by the applied field. In terms of the polarizability, the electronic polarizability, α_{ele}, of each ion is listed in Table 2-7 which is taken from ref. (19), and the ionic polarizability, α_{ion}, is regarded as being proportional to the absolute charge of each ion: $\alpha_{ion} = M \times |Q|$, where Q is the charge of the ion. The value of the coefficient, M, is discussed later in this section.

Table 2-7 Electronic polarizabilities of ions, in 10^{-24} cm^3.

Ion	O^{2-}	F^-	Na^+	Mg^{2+}	Cl^-	K^+	Ti^{4+}	Sr^{2+}
a_{ele}	2.4	0.858	0.290	0.094	2.947	1.133	0.19	1.6

2.4.2 Comparison between calculated and observed permittivity

In the Section 2.3.2, many stable structures were obtained for various substances. Among these structures, crystals which have rock-salt structure have been sufficiently studied and their properties are well-known today. Therefore, it is favorable to compare the calculated permittivities of these crystals to those observed in order to begin the following discussion. As to the rock-salt-type crystals and the ideal STO, the coefficient of ionic polarizability M, the calculated permittivity, and the observed permittivity[20, 21] are listed in Table 2-8. M is decided on purpose for the calculation to obtain good agreement with the experimental values. We shall discuss the permittivity of room temperature because the stable structures were computed with parameters which have been derived from structures observed at room temperature.

Table 2-8 Observed and calculated permittivities of crystals.
M is the coefficient of ionic polarizability used in the calculations.

	Coefficient M	Relative permittivity	
		Calculated	Observed
$SrTiO_3$	0.170	355	330
MgO	0.295	17.0	17–34
	0.376	33.9	
NaCl	1.550	5.62	5.62

Here, we have to note that the coefficient M is strongly dependent on the structure and ionic charge of the objects in the above calculation. Universal discussions for various STO structures cannot be explored under this condition.

We now introduce an improvement to the computation of permittivity as follows. Ionic polarization is caused as a result of the dislocation of ions along the electric field. When a finite electric field is applied to each ion, its dislocation becomes larger as it can move easier in the crystal, that is, as its bond is weaker. Figure 2-5 shows this situation. When the electric field is zero, the net force at which an ion perceives is zero at the stable point. When the local electric field E generates around the ion with the charge of Ze, the force of ZeE occurs, and the ion shifts along the field. The ion shall stop at the point where the short-range repulsion force principally pushes back it and the net force reaches zero again.

When the applied electric field is not so large, the force vs. r curve adjacent to the equilibrium point can be approximated linearly (in practical situations, this discussion is in the range where the permittivity is independent of the electric field amplitude: For STO single crystal, it is ~at least 10^6 V/m). In this range, the dislocation is given by, as in Fig. 2-5,

$$r_0 = -ZeE \,/\, (\text{slope of the approximated line}). \tag{2-7}$$

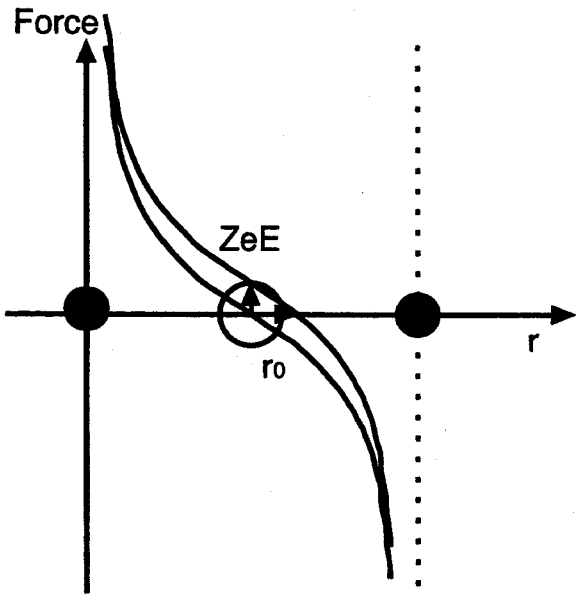

Fig. 2-5 Ion dislocation due to the local electric field.

In the above equation, the slope of the approximated line, the differential of the force, varies. The revision on this point is appended to the previous calculation, in particular to the coefficient M of the ionic polarizability. In the revision, the field is deduced by differentiating the interatomic potential given by the Eq. (2-3). The dislocation of titanium ions in the ideal STO single crystal is taken as a unit, and the dislocation of other ions is expressed by the ratio to it. The calculated dielectric properties with the treatment are shown in Table 2-9. M is decided in order for a good correspondence on the STO permittivity to the observed one, and is kept constant this time according to the idea that the coefficient is universal to all crystals. Although the computed results are smaller than the observed value, acceptable agreements are obtained with the common M.

Table 2-9 Polarization corrections and permittivities of crystals. The coefficient M is constant of 0.1862 in the calculations.

	Dislocation correction	Relative permittivity	
		Calculated	Observed
$SrTiO_3$	Sr : 3.334 Ti : 1.000 O_a : −0.505 O_b : −2.205	329	330
MgO	Mg : 1.563 O : −1.331	14.5	17-34
NaCl	Na : 5.594 Cl : −4.967	3.97	5.62
KCl	K : 6.482 Cl : −6.428	3.27	4.68
NaF	Na : 3.701 F : −3.576	3.00	6.0
KF	K : 4.768 F : −4.769	2.87	6.05

2.4.3 Permittivities of several types of $SrTiO_3$ crystals

By means of the revised calculation introduced in the preceding part, permittivities of several types of STO crystals are computed here. The permittivities are also of those at room temperature as explained above.

At first, the permittivities of STO crystals which contain oxygen vacancies are calculated. They are of three crystals consisting of one-oxygen-deficient 2×2×2, 3×3×3, and 4×4×4 STO lattices, whose stable structures are obtained in Section 2.3.2. Calculated permittivity is shown in Fig. 2-6. Since the vacancy sites of oxygen ions do not locate in complete symmetry, it shows the isotropy in dielectric property. Although an improvement is necessary for a strict discussion in which the calculated value compares directly to the practical one, it seems reasonable to suppose that the current simple calculation reflects the experimental results: The polarization properties become worse when the STO thin films are fabricated in the condition of insufficient oxygen radicals.

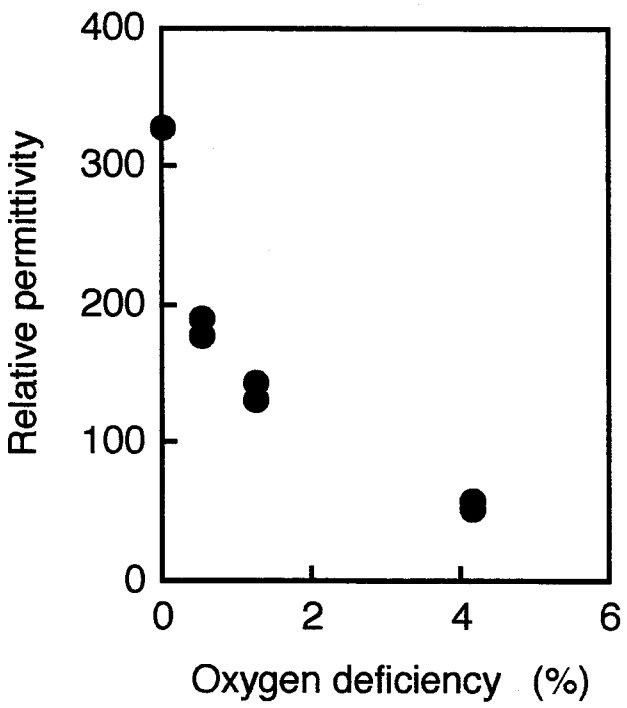

Fig. 2-6 Calculated permittivities of STO single crystals as a function of oxygen deficiency. The upper data at each deficiency correspond to the condition in which the electric field is applied parallel to the *x*-*y* plane of the crystals.

Next, let us discuss the case in which STO has a different structure from the perovskite, sliding-in Sr-O plane. From the work experimentally done before, we can learn that the permittivities of STO crystals decrease steeply when the composition deviates from stoichiometry. The relative permittivity of ~90 has been observed in the corresponding range of $SrO(SrTiO_3)_3$ in the former work. The calculated data of the current calculation is shown in Table 2-10, which depend on the direction of the electric field. The dielectric property is strikingly deteriorated when the sliding-in Sr-O planes are inserted vertically to the field, just the same as the effect of the parallel-plate capacitor of low permittivity connected in series. In terms of the value itself, we may say that the calculation gives a good agreement with the observed one, though it depends upon the direction of crystal axis.

Table 2-10 Calculated permittivities of $SrO(SrTiO_3)_3$ crystal.

Direction of field	*x*	*z*
Relative permittivity	105	20.3

So far, we discussed the polarization property of STO crystals through the evaluation of several representative structures. As described later, the perovskite structure of the ideal STO crystal is a significantly prominent structure for dielectric properties in which each ion enhances other ions' polarization in the mutual interaction. No matter what kind of dislocation would occur in the crystal, it means that the crystal loses the priority. The present calculation indicates it, and also in the following section, the experiment of thin films shows that its polarization properties were deteriorated when the deposition condition was inadequate and the crystallinity was degraded (in the worst case, STO became amorphous). Although we cannot definitely say that the relationship is satisfied in all cases, these results lead to the conclusion that the correlation between the structural transformation and the degradation of polarization property is strong.

2.4.4 Discussion of ionic charge

The permittivity calculation has been carried out on the basis that all atoms are completely ionized in crystals. However, this is not in keeping with physical facts. Let us examine the point hereafter in this part.

The index, ionicity, has been defined as denoting the ionic character of crystals.[22] The ionicity is the ratio of ionic character when one set the summation between it and covalent character is a unit. Its value depends on the crystal structures and the ion types, and is 0.94 for NaCl, and 0.84 for MgO single crystal, for example.[19] In the stable structure calculation discussed above, the empirical parameters of the short-range repulsion energy are determined on the basis of the completely ionized model. Therefore, its calculation implicitly included the notion of the ionicity. On the other hand, however, it is not comprised in the preceding permittivity calculation. Because the calculation of ion polarization takes the ionic charge, the influence of ionicity is reflected directly to the results of permittivity. Let us take the correction of the ionicity into account to the computation of permittivity.

Firstly, we shall set the coefficient M to obtain an accordance between calculated and observed permittivities of NaCl single crystal, where the charge of Na and Cl ions are 0.94 and -0.94, respectively, according to the above-stated ionicity. When M is 0.3322, its calculated and observed permittivities match each other at the value of 5.62.

Secondly, the permittivity of MgO single crystal is calculated with this decided M, where the charge of Mg and O ions are also treated with the ionicity, that is, 1.68 and -1.68, respectively. Its calculated permittivity is 23.5, and we can have a more desirable agreement with the observed one of 17–34. The result tells us that this correction with the ionicity is proper for the permittivity calculation.

Finally, let us discuss the case of STO single crystal. We shall determine its ionicity by following the opposite procedure to the MgO case. In other words, the ionic charge of each ion that reflects ionicity is derived by fitting with the decided M to the already-known relative permittivity of 330. There are two conditions imposed in the calculation. The first one is the fixed Sr charge condition of -2, which is derived from the theoretical result of the *ab initio* MO calculation for the $BaTiO_3$: There is significant hybridization between the Ti and O, but the Ba is quite ionic and is well described as a Ba^{2+} ion,[23] and from the experimental result that $BaTiO_3$ also has the same perovskite-type structure and Sr ion is smaller than Ba

ion. The second condition is the charge neutralization, which is inevitable. On the above-stated conditions, there is only one variable of the ionic charge of Ti or O. When the variable is obtained, another charge is automatically derived with it. The calculated ionic charges are listed in Table 2-11. The validity of these values is discussed later in Section 2.5.3. Here the author only mentions that Ti and O ions inside the perovskite structure have a covalent character to a large extent.

Table 2-11 Calculated ionic charge of each ion in the $SrTiO_3$ single crystal.

Sr	Ti	O
2.00 (fixed)	2.13	−1.38

2.5 Discussion with Molecular Orbital Calculation

2.5.1 Density functional theory

In recent years, a considerable amount of experiments have been done in the first-principle calculation of material properties within the framework of the density functional theory (DFT).[24-27] DF method is a representative of the *ab initio* molecular orbital (MO) calculations to study electron states of atoms and/or molecules. Owing to the advantage that DF method does not use empirical parameters at all, it is regarded as a potent method of treating any substance including whole new materials. The name of molecular orbital calculation suggests the limitation of the application of this method, in particular with reference size. However, when the number of atoms of molecules is increased and the cluster model is used, we can study localized phenomena of crystals. When we employ the periodic boundary condition, the results reflect the physical properties of bulk crystals. At present, DFT is applied to a wide variety of fields with the assistance of the development of computer power.

Strikingly good agreements between first-principle calculations and experimental data have been found for a number of physical properties:[28 - 36] The theory predicts the electron states (static electron distribution and orbital shape), the most stable configuration of atoms, the electron static potential, the charge density, the linear polarizability, the probability of electron transition, the reaction energy, the free energy of molecules, and so on.

In this part, the quantum-mechanical treatment, DFT, is applied to the $SrTiO_{3-\delta}$ crystals and more advanced discussions are given.

Initially, we consider the application of a numerical method to the variational solution of the Schrödinger equation with a one-electron Hamiltonian

$$H(\boldsymbol{r}) = -\frac{1}{2}\nabla^2 + V(\boldsymbol{r}), \tag{2-8}$$

where $V(\boldsymbol{r})$ represents some approximation to the potential for an electron in the crystal. (All energies are given in Hartree atomic units e^2/a_0 and lengths in Bohr radii a_0, where e is elementary electric charge.) $V(\boldsymbol{r})$ consists of Coulomb and exchange terms

$$V(\boldsymbol{r}) = V_c(\boldsymbol{r}) + V_x(\boldsymbol{r}). \tag{2-9}$$

Here the Coulomb potential is the sum of nuclear and electronic contributions

$$V_c(\boldsymbol{r}) = -\sum_v \frac{Z_v}{|\boldsymbol{r} - \boldsymbol{R}_v|} + \int \frac{d\boldsymbol{r}'\rho(\boldsymbol{r}')}{|\boldsymbol{r} - \boldsymbol{r}'|}, \tag{2-10}$$

where $\rho(\boldsymbol{r}')$ is the molecular charge density. The exchange-correlation term is given by statistical local expression and is written as[37]

$$V_x(\boldsymbol{r}) = -3\alpha\left[\frac{3}{8\pi}\rho(\boldsymbol{r})\right]^{1/3}, \tag{2-11}$$

where α is the only parameter used in this model. Optimum values of α have been discussed for many atoms[38] and molecules.[39] Baerends *et al.* have shown that theoretical ionization energies and dipole moments are in excellent agreement with experimental values when α = 0.7 for many molecules and metal complexes.[40] Therefore, we prefer to use $\alpha = 0.7$ through the present calculation.

In the present method, the λth molecular wave functions are given by

$$\psi_\lambda = \sum_i C_{i\lambda}\chi_i, \tag{2-12}$$

where χ_i's are symmetrized linear combinations of atomic orbitals (LCAO), thus

$$\chi_i(\boldsymbol{r}) = \sum_{vlm} W^{il}_{vm} \phi^{v}_{nlm}(\boldsymbol{r}_v), \tag{2-13}$$

where $\boldsymbol{r}_v$ is coordinate referred to the atom v. Here W^{il}_{vm} are the symmetrization coefficients obtained from group theory and basis functions $\phi^{v}_{nlm}(\boldsymbol{r})$ are orbital functions centered on the atomic sites, which can be written as

$$\phi^{v}_{nlm}(\boldsymbol{r}) = R^{v}_{nl}(r) Y_{lm}(\hat{r}), \tag{2-14}$$

where $R^{v}_{nl}(r)$ is radial part of the atomic orbital and is generated by numerical computation of an atomic problem. The angular part of the atomic orbital $Y_{lm}(\hat{r})$ is taken to be real spherical harmonics.

The variational principle leads one to the secular matrix equation,

$$\boldsymbol{HC} = \varepsilon \boldsymbol{SC}. \tag{2-15}$$

In the DFT, the discrete variational (DV) integral method is popular, in which the elements of the Hamiltonian and overlap matrices H_{ij} and S_{ij} are evaluated as weighted sums of integrand values at sample points, instead of the conventional Rayleigh-Ritz method, namely

$$\begin{aligned} H_{ij} &= \sum_k \omega(\boldsymbol{r}_k) \chi^*_i(\boldsymbol{r}_k) h(\boldsymbol{r}_k) \chi_j(\boldsymbol{r}_k), \\ S_{ij} &= \sum_k \omega(\boldsymbol{r}_k) \chi^*_i(\boldsymbol{r}_k) \chi_j(\boldsymbol{r}_k), \end{aligned} \tag{2-16}$$

where $\boldsymbol{r}_k$ is one of a total N sample points in three-dimensional real space and $\omega(\boldsymbol{r}_k)$ is the integration weight or reciprocal of sample point density at $\boldsymbol{r}_k$. These values converge to Rayleigh-Ritz values when the number of sample points N is increased.[41, 42] The eigenvalue problem of Eq. (2-15) can be solved by means of the standard method, providing orbital eigenvalues and eigenfunctions.

The molecular charge density $\rho(\boldsymbol{r})$ can be evaluated from

$$\rho(\boldsymbol{r}) = \sum_{\lambda ij} f_\lambda C^*_{i\lambda} C_{j\lambda} \chi^*_i(\boldsymbol{r}) \chi_j(\boldsymbol{r}). \tag{2-17}$$

In order to obtain information of electron transfer and bonding nature, one can use the Mulliken population analysis, by which the molecular charge of Eq. (2-17) is partitioned into gross population for each orbital,

$$n_i = \sum_{\lambda j} f_\lambda C^*_{i\lambda} C_{j\lambda} \sum_k \omega(\boldsymbol{r}_k) \chi^*_i(\boldsymbol{r}_k) \chi_j(\boldsymbol{r}_k), \tag{2-18}$$

and two-center charge called overlap population is defined as

$$n_{ij} = \sum_{\lambda} f_{\lambda} C_{i\lambda}^{*} C_{j\lambda} \sum_{k} \omega(\boldsymbol{r}_k) \chi_i^{*}(\boldsymbol{r}_k) \chi_j(\boldsymbol{r}_k) . \tag{2-19}$$

These values are very useful for discussions of charge distribution and covalency.

In practical calculations, an initial charge distribution is given, which is generally a simple combination of atomic orbitals. In a series of the above calculation of solving the Schrödinger equation, a new charge distribution is obtained in the potential deduced by the old one. This procedure is iterated until former and latter distributions became identical, and after the convergence, each physical value can be achieved. This calculation manner is shown in Fig. 2-7.

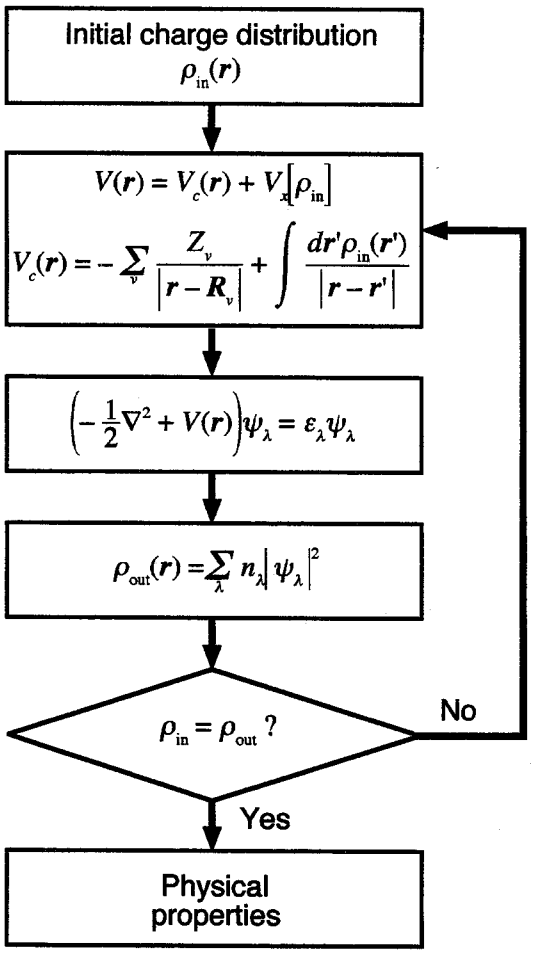

Fig. 2-7 Scheme of calculation using LCAO.

Let us examine the periodicity of lattice in the calculation. In the present work, the cluster approximation is employed. It is a favored method for describing the local electron states of a partial region of crystals when one would like to compute a complicated large system such as solid surfaces where the periodicity ended. In other words, the local electron states of the cluster, which is partly quarried from crystals, are substituted for the states of the partial region practically existing inside the crystals. This approximation is familiar and applied to many molecular calculations at present. Although it had been invented to handle local phenomena, it gives us a satisfactory explanation of electron states not only of large molecules but also of single crystals even when the cluster size is comparatively small.[43] Owing to this advantage, the cluster approximation is employed in the present work.

Ions that locate outside of the cluster are taken into account through the Madelung potential in the calculation using MOs. Therefore, the size of the crystal in this calculation is regarded infinite. The ionic charge of each ion is an important parameter in computing the Madelung potential. We decided its value in the same manner introduced in the preceding section of obtaining the stable structures: The charge ratio of outer cations, Sr to Ti, is fixed of 1:2, and the charge of outer anions, O, is constant of -2. The total charge of cluster can also be deduced eventually by following this manner.

The calculation model discussed in this part is aimed to be included in the preceding program of the permittivity calculation in pursuit of the evaluation method improvement of polarization properties. It can be said that the standing point of this work is different from that of ordinary commercial MO calculation programs. In this thesis, the word "MO calculation" is defined as the theoretical investigation of polarization properties in which MOs are taken into account.

2.5.2 Molecular orbitals of $SrTiO_3$ crystal

Let us think first about atomic radial functions. In the present work, the LCAO tight-binding bases are implemented with exponential Slater-type orbitals. When a one-electron orbital is fitted by only one Slater-type orbital, finite errors arise in the case of heavy atoms. Therefore, the two Slater-type orbital approximation is used in which a one-electron orbital is described by a combination of two Slater-type orbitals, in other words,

$$\begin{aligned} R_i(r) &= \sum_i C_{i1}S_{i1}(r) + C_{i2}S_{i2}(r), \\ S_i(r) &= \left[\frac{(2\kappa_i)^{2n+1}}{(2n)!}\right]^{\frac{1}{2}} r^{n-1}\exp(-\kappa_i r), \end{aligned} \tag{2-20}$$

where i is the sequential number that consists of three quantum numbers of principal number n, orbital quantum number l, magnetic quantum number m, r is radius, C is linear coefficient, $S_i(r)$ is the Slater-type orbital, and κ is orbital exponent and is taken from ref. (44). Some of them are not on the list, and are deduced by the linear least-square approximation. C is decided in the Rayleigh-Ritz variational procedure to make total energy least.

Next, molecular wavefunctions are extended into symmetry orbitals according to the group theory. This scheme decreases the number of elements we have to calculate in the secular matrix Eq. (2-14). That is to say it reduces the computation time and enhances the accuracy.

In regard to the present work, ideal $SrTiO_3$ crystal is described by the $Ti_2O_{11}^{14-}$ cluster according to the cluster approximation. The $Ti_2O_9^{11.33-}$ cluster is also examined as the oxygen-deficient $Sr_2Ti_2O_5$, and compared with the former. These are depicted in Fig. 2-8. Lattice constants and ion configuration of each structure are taken from the results calculated in Section 2.3 for the sake of simplicity.

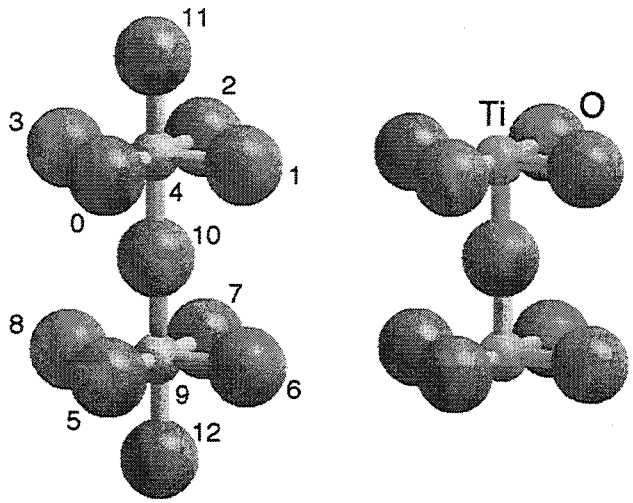

(a) $Ti_2O_{11}^{14-}$ (b) $Ti_2O_9^{11.33-}$

Fig. 2-8 $Ti_2O_{11}^{14-}$ and $Ti_2O_9^{11.33-}$ clusters.

As for the atomic orbitals of two components of the cluster, O and Ti ions, 1*s* - 2*s* for oxygen and 1*s* - 4*p* for titanium are used. Only orbitals which locate adjacent to the valence electron orbital interfere with one another substantially. Therefore, 3*p* - 4*p* orbitals are solely treated for Ti as mutually interacting orbital sets in this calculation (the frozen-core approximation).

2.5.3 Electron states and polarization properties

The calculation program concerning MOs was written by the author according to the procedure explained above. In Figs. 2-9 and 2-10, calculated band diagrams and electron density of states of the two crystals are shown respectively. Although the band diagram of Fig. 2-9(a) successfully describes the insulating property of ideal STO, its band gap is smaller than the experimental data of ~3.15 eV.[45, 46] It is supposed to ascribe to the implementation of the local density approximation (LDA) to the exchange-correlation potential. So far, it has

been pointed out that LDA often produce finite errors in the derivation of band gap and estimate it smaller (*e.g.*, That of Si calculated was ~0.5 eV). When oxygen vacancies occur as in Fig. 2-9(b), levels appear in the band gap which are generally called donor levels, and the highest occupied molecular orbital (HOMO) level locates just below the conduction band. In other words, oxygen-deficient STO behaves as an *n*-type semiconductor. Another group obtained a similar result using the DV-Xα cluster method from a different point of view to investigate the surface defect states.[31] While the polarization properties have been mainly discussed so far, the existence of the conductivity is fatal for the application of gate insulating films and memory cells. It is necessary to include a discussion of conductivity for further studies.

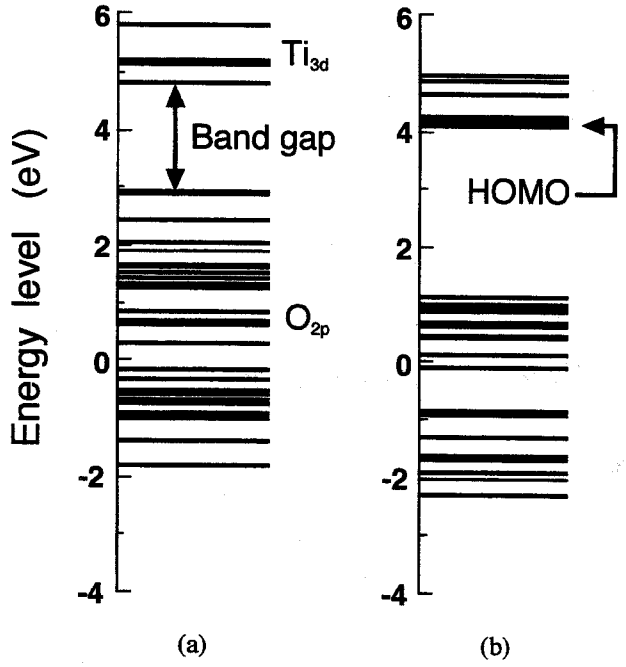

Fig. 2-9 Calculated band diagrams of (a) $SrTiO_3$ and (b) $Sr_2Ti_2O_5$.

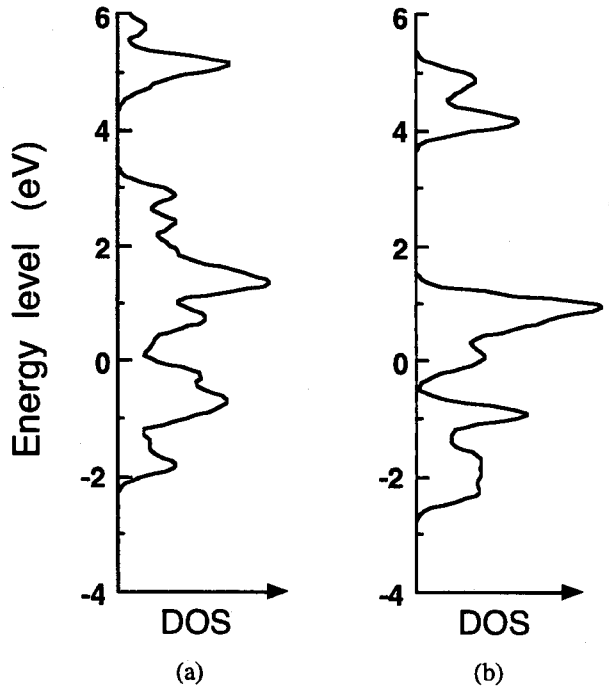

Fig. 2-10 Calculated density of states of (a) $SrTiO_3$ and (b) $Sr_2Ti_2O_5$.

Let us examine the ionic charge, the Mulliken charge, which is directly related to polarization phenomena. In Table 2-12, the Mulliken charge of each ion is summarized, where the site number is depicted in the preceding Fig. 2-8. The data that had been obtained in the former Section 2.4.4 and by other groups' MO calculations are also written in the table for comparison. In terms of the ideal STO single crystal, the ionicity of the present MO calculation is a little bit smaller than others, whereas it gives us a true picture that ions in the STO crystal are not completely ionic, but covalent to large extent. Furthermore, it is noteworthy that the result given in Section 2.4.4 shows a surprisingly good accordance with that of the MO calculation, though it was deduced by the simple manner of polarization calculation. It is the first work to elicit the ionicity in this manner, and can be a companion to enlarging MO calculations in the future.

One important future subject is to design all calculations of stable structures, dielectric constants, and the molecular orbitals in a self-consistent state. After that, we can proceed to

further discussions such as changes of physical properties due to the fairly large decrease of titanium ionic charge in the oxygen-deficient STO crystal.

Table 2-12 Calculated net charge of each ion in STO crystals.
The number in parentheses is its site number.

	O(1-3, 5-8)	O(10)	O(11, 12)	Ti(4, 9)
$Ti_2O_{11}^{14-}$	−1.60	−1.36	−1.72	1.80
$Ti_2O_9^{11.33-}$	−1.56	−1.20	---	1.18
Data from Section 2.4.4	−1.38			2.13
Tukada *et al.* for ideal STO[31]	−1.72	−1.30	−1.72	2.23
Cohen *et al.* for $BaTiO_3$[23]	−1.63			2.89

2.6 Summary

In this chapter, correlation between the structure and the polarization properties of STO has been investigated from the microscopic view. It was discussed with the representative cases in the thin film fabrication: STO contains oxygen vacancies and unintentional structures aside from the perovskite due to the insufficient oxidation and the nonstoichiometry, respectively.

First of all, stable structures of several substances including the above two cases were calculated by concerning the two-body central force interatomic potential. In terms of the structure of well-known materials such as NaCl and MgO, the calculation gave pleasant agreements with the experimental data. On the basis of this propriety, the computation was carried out for the stable structures of those crystals which consist of oxygen-deficient STO lattices and have sliding-in Sr-O planes. As to the former structure, the lattice constant showed an inclination to stretch when the oxygen deficiency increased, which led to a conclusion that the reduction of the Coulomb force influences more than the decrease of the short-range repulsion force on the stabilization of the STO structures as oxygen deficiency takes place. This computation result of the inclination upheld the experimental fact. In regard to the STO crystal that holds the sliding-in Sr-O planes, the calculated lattice in the vicinity of the sliding-in Sr-O plane was slightly distorted as in the experimental result.

The polarization property of the above-calculated crystals was successively investigated. The calculation was carried out with the the local field correction on a reasonable assumption that ionic polarization is proportional to ionic charge. In the simplest model, the proportional coefficient used in the polarization calculation differed from others on various substances, in other words, it became clear that we could not have a universal discussion on the model. Therefore, the improved correction was introduced in which the ease of each ion dislocation in the interatomic potential was considered. Owing to the latter correction, the calculation could explain the observed results of well-known substances with the common value of the proportional coefficient, and the polarization property of the oxygen-deficient STOs and the nonstoichiometic $SrO(SrTiO_3)_3$ were investigated successively. Their calculated results indicated that the polarization property is degraded as the STO structure diverts from the ideal perovskite. Furthermore, the discussion about the ionicity was carried out in an unprecedented manner with the present calculation. It disclosed

that the bonds in the perovskite structure are not completely ionic in the least, but covalent to a large extent.

For further investigation, the improved calculations which employ the theory of MOs were carried out to ideal and oxygen-deficient STO's using the density functional method. Although the calculated band gap of the ideal STO single crystal was smaller than the experimental one, it presented the precise view that ideal STO is an insulator and it becomes conductive when it contains enough oxygen vacancies. By means of the calculation with MOs, the electron distribution was deduced which directly relates to the polarization.

All these studies in this chapter led the conclusion that there is an intimate relationship between the structure of STO single crystals and their polarization properties, and it is sufficiently probable that the degradation of polarization is caused by the deviation from the perovskite structure, which is significantly prominent for ions to enhance each other to polarize through the mutual interaction.

References

(1) T. Hirano, M. Taga, and T. Kobayashi, Jpn. J. Appl. Phys. **32**, L1760 (1993).

(2) M. H. Yeh, K. S. Liu, and I. N. Lin, Jpn J. Appl. Phys. **34**, 2447 (1994).

(3) M. Hiratani, K. Imagawa, and K. Takagi, J. Phhl. Phys. **78**, 4258 (1995).

(4) H. Yamaguchi, P. Y. Lesaicherre, T. Sakuma, Y. Miyasaka, A. Ishitani, and M. Yoshida, Jpn. J. Appl. Phys. **32**, 4069 (1993).

(5) P. C. Joshi, and S. B. Krupanidhi, J. Appl. Phys. **73**, 7627 (1993).

(6) D. Roy, C. J. Peng, and S. B. Krupanidhi, Appl. Phys. Lett. **60**, 2478 (1992).

(7) H. Yamaguchi, S. Matsubara, and Y. Miyasaka, Jpn. J. Appl. Phys. **30**, 2197 (1991).

(8) T. Kuroiwa, T. Honda, H. Watarai, and K. Sato, Jpn. J. Appl. Phys. **31**, 3025 (1992).

(9) K. Abe, and S. Komatsu, Jpn. J. Appl. Phys. **32**, 4186 (1993).

(10) S. Yamamichi, T. Sakuma, K. Takemura, and Y. Miyasaka, Jpn. J. Appl. Phys. **30**, 2193 (1991).

(11) K. Matsui, M. Taga, and T. Kobayashi, Jpn. J. Appl. Phys. **32**, L796 (1993).

(12) I. Okada, and E. Osawa, *Bunshi Simulation Nyumon* (Introduction to Molecular Simulation) (Kaibundo, Tokyo, 1989) p.112 [in Japanese].

(13) K. Kawamura, *Personal Computer Bunshi Simulation* (Molecular Simulation of Personal Computer) (Kaibundo, Tokyo, 1990) p.22, p.56 [in Japanese].

(14) D. W. Kim, N. Enomoto, Z. Nakagawa, and K. Kwamura, J. Am. Ceram. Soc. **79**, 1095 (1996).

(15) F. S. Galasso, *Structure and Properties of Inorganic Solids* (Pergamon Press Ltd., Oxford, 1970).

(16) W. Gong, H. Yun, Y. B. Ning, J. E. Greedan, W. R. Datars, and C. V. Stager, J. Solid State Chem. **90**, 320 (1991).

(17) O. Michikami, and M. Asahi, Jpn. J. Appl. Phys. **30**, 466 (1991).

(18) J. M. Luttinger, and L. Tisza, Phys. Rev. **70**, 954 (1946).

(19) C. Kittel, *Introduction to Solid State Physics 6th Edition* (John Wiley and Sons, Inc., New York, 1986).

(20) A. J. Dekker, *Solid State Physics* (Prentice-hall, Inc., New York, 1957).

(21) R. C. Neville, B. Hoeneisen and C. A. Mead, J. Appl. Phys. **43**, 2124 (1972).

(22) J. C. Phillips, *Bonds and Bands in Semiconductors* (Academic Press, New York, 1973).

(23) R. E. Cohen, and H. Krakauer, Phys. Rev. **B42**, 6416 (1990).

(24) P. Hohenberg, and W. Kohn, Phys. Rev. **136**, B864 (1964).

(25) W. Kohn and L. J. Sham, Phys. Rev. **140**, A1133 (1965).

(26) S. Lundqvist, and N. H. March, *Theory of the Inhomogeneous Electron Gas* (Plenum, New York, 1983).

(27) W. Kohn, and P. Vashista, in *Theory of the Inhomogeneous Electron Gas*, Ref. 2, p.79.

(28) R. M. Martin, *Festkörperprobleme* (Advaces in Solid State Physics), edited by H. J. Quiesser (Pergamon/Vieweg, Braunschweig, 1982), Vol.25, p.3.

(29) M. L. Cohen, Phys. Scr. **T1**, 5 (1982).

(30) S. Baroni, and R. Resta, Phys. Rev. **B33**, 7017 (1986).

(31) M. Tsukada, C. Satoko, and H. Adachi, J. Phys. Soc. Jpn. **48**, 200 (1980).

(32) M. Posternak, A. Baldereschi, A. Catellani, and R. Resta, Phys. Rev. Lett. **64**, 1777

(33) J. Andzelm, and E. Wimmer, J. Chem. Phys. **96**, 1280 (1992).

(34) R. D. King-Smith, D. Vanderbilt, Phys. Rev. **B47**, 1651 (1993).

(35) R. Resta, M. Posternak, and A. Balderschi, Phys. Rev. Lett. **70**, 1010 (1993).

(36) W. Zhong, D. Vanderbilt, and K. M. Rabe, Phys. Rev. Lett. **73**, 1861 (1994).

(37) For a review of the Hartree-Fock-Slater model, see J. C. Slater, *Quantum Theory of Molecules and Solids* (McGraw-Hill, 1974) Vol.4.

(38) K. Schwarz, Phys. Rev. **B5**, 2466 (1972).

(39) E. J. Baerends, and P. Ros, Chem. Phys. **2**, 52 (1973).

(40) E. J. Baerends, and P. Ros, Molecular Phys. **30**, 1735 (1975).

(41) D. E. Ellis, and G. S. Painter, Phys. Rev. **B2**, 2887 (1970).

(42) E. J. Baerends, D. E. Ellis, and P. Ros, Chem. Phys. **2**, 41 (1973).

(43) H. Adachi, *Ryoshi Zairyo Kagaku Nyumon* (Introduction to Quantum Material Chemistry) (Sankyo-Shuppan, Tokyo, 1991) p.138 [in Japanese].

(44) S. Sugano, T. Satoko, S. Ohnishi, *Mitsudo-hankansuu-ho to Sono Oyo* (Density Functional Method and Its Application) (Kodansha, Tokyo,1994) p.66 [in Japanese].

(45) H. W. Gandy, Phys. Rev. **113**, 795 (1959).

(46) V. E. Henrich, G. Dresselhaus, and H. J. Zeiger, Phys. Rev. **B17**, 4908 (1977).

Chapter 3
GROWTH AND CRYSTALLINITY OF HIGHLY POLARIZABLE $SrTiO_3$ THIN FILMS

3.1 Introduction

So far, various deposition techniques have been thoroughly studied and applied to a number of highly polarizable materials. As seen in Chapter 1, those are rf magnetron sputtering, ion-beam sputtering, pulsed laser deposition (PLD) method, co-evaporation, sol-gel, chemical vapor deposition (CVD), and metal organic chemical vapor deposition (MOCVD), and so on. In the present work, the fabrication of high quality STO thin films are carried out with two techniques from among the above, the rf magnetron sputtering and the PLD method. Although both of them are well established today, it needs trial and error to obtain the desirable circumstances for the STO growth. Furthermore, the PLD method has a significant problem of particle and/or droplets which are caused by the explosive spouting of the melted target, and this primitive but intrinsic problem must be solved for the development of many electrical applications of highly polarizable thin films.

In this chapter, we shall review the two deposition methods first. An innovative technique is proposed, which solves the above-stated problem of particle and/or droplets peculiar to the PLD method. Secondly, the preparation technique of substrates is discussed with an interesting phenomenon. Finally, the surface smoothness and epitaxy of the fabricated thin films are investigated by the analysis of scanning electron microscope (SEM), X-ray diffraction (XRD), and reflection high-energy electron diffraction (RHEED).

3.2 Fabrication Technique of $SrTiO_3$ Thin Films

3.2.1 Rf magnetron sputtering

Rf magnetron sputtering is a useful technique for thin film fabrication, in which high energy particles accelerated by an electric field collide with the target material and the sputtered atoms and/or molecules are deposited on a substrate. The rf magnetron sputtering has several advantages to other methods, such as:

- Considerable uniformity of thin films can be obtained in a large area with a small distance between the target and the substrate,
- Reproducibility of identical quality films is quite high,
- Deposition can be carried out in highly dense reaction gas, and in a large range of gas pressure.

On the other hand, the method has some demerits, such as:

- Deposition rate is about one-tenth times smaller than vacuum evaporation or PLD method,
- Apparatus configuration is not simple because of the supply system of rf power,
- Ambient temperature increases due to the thermal radiation from the target and secondary electron emission, which causes difficulty of thermal control.

Figure 3-1 shows the apparatus configuration of the rf magnetron sputtering. High frequency electron field is applied between the two electrodes, and the electrons are accelerated in the atmosphere. There is no electrification of positive ions, therefore, the method can be successfully used for insulating thin films. Moreover, the simultaneous application of electric and magnetic fields leads to the high efficiency of ion generation and enhances the deposition rate.

In the present work, the deposition of STO thin films was carried out in the atmosphere of 5 Pa O_2 and 5 Pa Ar. The substrate temperature was 540 °C and the input rf power was 0.38 W/cm^2. Pressed-powder target was used which was formed under the pressure of 300 kgf/cm^2. The Sr:Ti ratio of the target was 1.0:1.0.

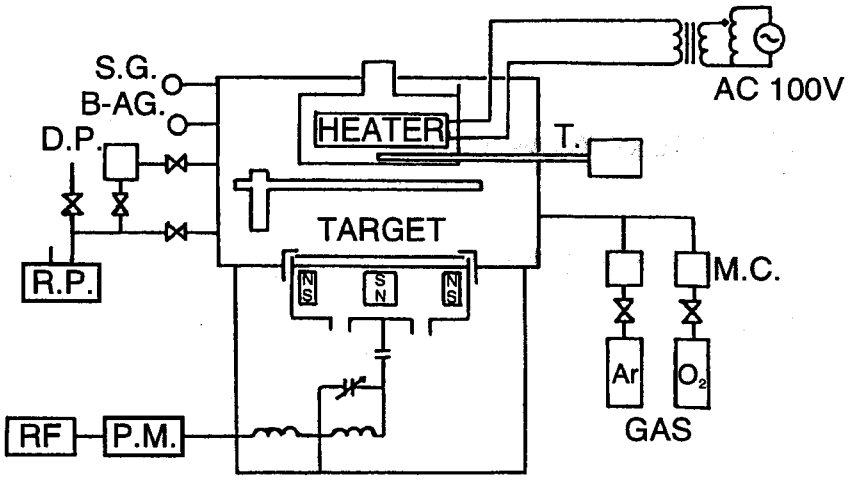

Fig. 3-1 Apparatus configuration of rf magnetron sputtering.

3.2.2 Pulsed laser deposition method

PLD method has been widely used for thin film growth of ferroelectrics and oxide superconductors[1-7] with many advantages, such as high-rate growth and transfer of the composition from target to film. However, it suffers from a significant problem of particles and/or droplets which scatter on the grown surface. The defective morphology brought about by those anomalies is unfavorable for the application of thin films in electronics. As is well known, the target surface temperature can exceed the boiling point in an instant upon pulsed laser irradiation,[8] which, in turn, causes explosive spouting of the melting target which flies directly to the substrate surface. In the present work, pressed-powder targets are used for STO, hence, the explosion of the targets is intense. Even the raw target materials may fly onto the substrate surface.

So far, some attempts to solve the aforementioned problem have been made. The off-axis deposition method is one of them. In this method, the substrate is less likely to receive flying droplets. Holzapfel *et al.*[9] succeeded in obtaining a distinct reduction of droplets and

particles as long as condensed targets (single crystal, glass, and ceramic bulk) are used. There is another method in which the laser power is set near the threshold of the target boiling point and the explosive spouting of the melted target is suppressed to a large extent.[3] However, not only do these methods not achieve complete elimination of particles, but also they are not appropriate for pressed-power targets.

Here an innovative PLD technique using a shadow mask placed between the target and the substrate is proposed aiming at the elimination of particles and/or droplets.[10, 11] The method is called the *eclipse method*, where the substrate, the shadow mask and the target corresponds to the earth, the moon and the sun, respectively. This method is illustrated in Fig. 3-2. The shadow mask plays an important role of blocking the particles which fly straight onto the substrate. Therefore, the deposition proceeds by the species being diffused by the ambient gas. By means of the eclipse method, one can ideally expect droplet- and particle-free films with mirror-like surfaces. In this work, an ArF laser beam ($\lambda = 193$ nm) is focused on the target at the fluence of 1.3 J/cm^2, and the laser pulse rate is 10 Hz. The target-substrate and the substrate-shadow mask distances are 50 and 20 mm, respectively, and the shadow mask size is 10×10 mm^2 while the substrate size is slightly smaller, around 9×9 mm^2.

STO thin films were deposited by the eclipse PLD method at 660 °C on $YBa_2Cu_3O_{7-\delta}$ and 500 °C on Pt substrates in 0.3 Torr oxygen ambient using the pressed-powder target which was formed under the pressure of 300 kgf/cm^2. The Sr:Ti ratio of the target was 1.0:1.1, the stoichiometric ratio of the the deposited films. Since the composition discrepancy from stoichiometry causes a fatal drawback in polarization properties due to an introduction of unintentional conformations, which are different from the perovskite structure as described in Chapter 2, it is quite important to adjust the composition of the target STO. The deposition rate of STO was 20 Å/min and the decrease of the rate compared with that of the conventional PLD was no more than 70 % despite the wholly covering of substrates by the shadow mask.

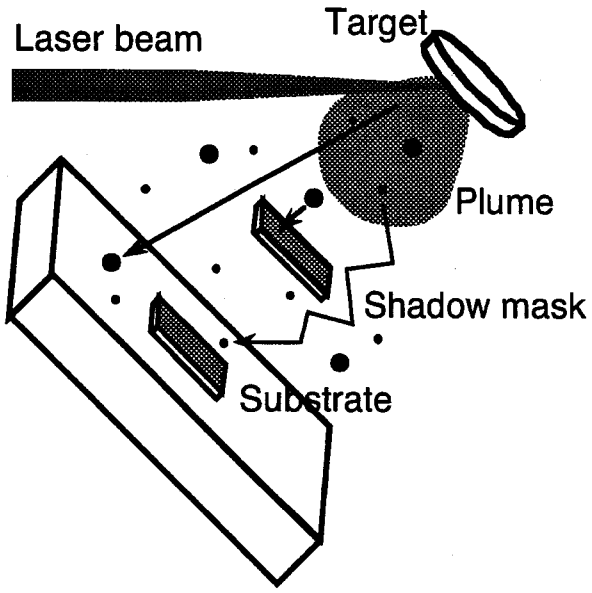

Fig. 3-2 Schematic view of eclipse PLD method.

3.3 Preparation Method of Substrate

We shall discuss the two kinds of substrate thin film materials on (100)MgO single crystal, high-temperature superconductor $YBa_2Cu_3O_{7-\delta}$ (YBCO) and metal Pt.

As to the YBCO, (001)-oriented thin films were deposited on the (100)MgO substrates at 750 °C in 0.3 Torr O_2 ambient, where the MgO substrates were annealed in 1 atm oxygen ambient at 1000 °C for 7 hours prior to the YBCO deposition. Owing to the pre-annealing treatment, MgO surface became atomically smooth, and the grown YBCO thin films on it showed a supereminent superconductivity on the resistance-temperature (R-T) property compared with those on non-annealed MgO.[12] A ceramic bulk target was used for the deposition. Although the substrates were behind the shadow mask, the decrease of the deposition rate to the conventional PLD method was only 70 % in the ambient condition, which was same as in the case of STO.

Pt films were grown by two methods, electron beam evaporation at 570 °C and rf magnetron sputtering at 540 °C. The atmosphere of the latter method was 4 Pa Ar, and the

sputtering power was 0.38 W/cm^2. In the YBCO case, oxygen-annealed (100)MgO single crystals were used as substrates. In the Pt case, on the contrary, fine thin films were obtained on both of annealed and non-annealed MgO. However, a surprising phenomenon was brought about in this case. This is the relationship between the treatment of MgO substrates and the orientation of Pt thin films: We got (111)-oriented Pt films on oxygen-annealed MgO substrates, and on the other hand, (100)-oriented Pt films on non-annealed substrates. This phenomenon was common on both deposition methods of the electron beam evaporation and the rf magnetron sputtering. Figures 3-3 and 3-4 show the XRD and RHEED patterns of Pt films on (a) annealed and (b) non-annealed (100)MgO single crystals, respectively. They reveal that the orientation of Pt films was drastically changed by the oxygen annealing treatment. Though the seemingly same orientation change of Pt films has been reported on MgO substrates with the variation of deposition temperature,[13, 14] this work is the first to disclose that it still changes with and without the pre-annealing treatment even when the deposition temperatures are identical.

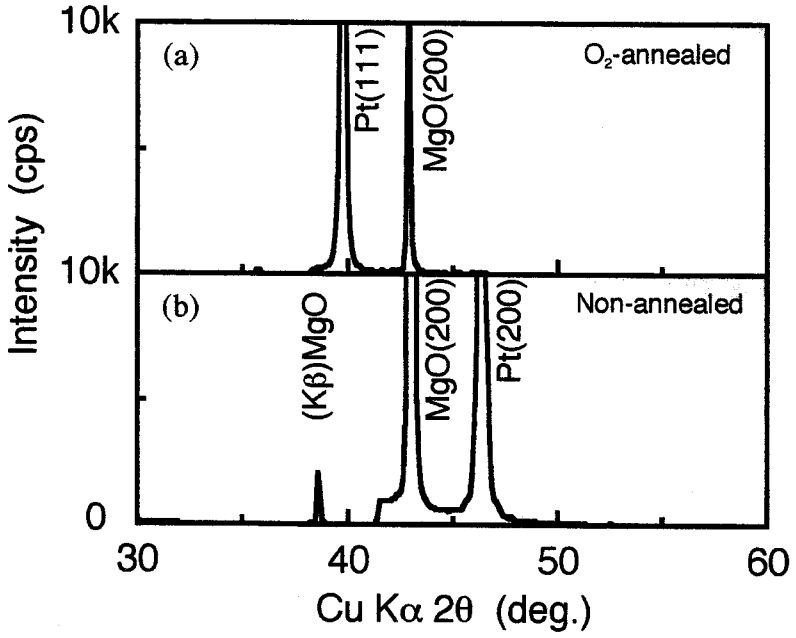

Fig. 3-3 XRD patterns of Pt thin thin films
on (a) annealed and (b) non-annealed (100)MgO.

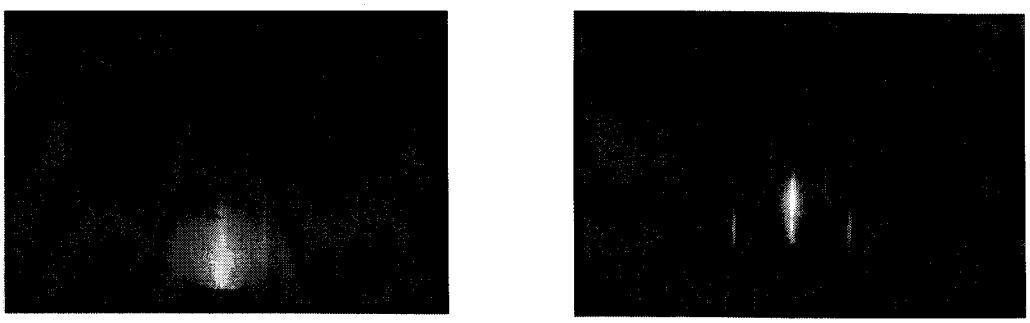

(a) (b)

Fig. 3-4 RHEED patterns of Pt thin thin films on (a) annealed and (b) non-annealed (100)MgO. <100> azimuth.

3.4 Crystallinity Characterization of $SrTiO_3$ Thin Films

3.4.1 Surface condition

In this part, we shall discuss the surface smoothness and a delightful by-product of its improvement which come from the priority of the eclipse PLD method. Figure 3-5 shows the SEM images of STO films which were deposited by the conventional method and the eclipse method, respectively. As for the film deposited by conventional PLD, there is a considerably large amount of droplets on the surface, as is shown in Fig. 3-5(a). They are unique to the PLD technique and cause the formation of pinholes, which allow current leakage even when the STO film itself is a good insulator. On the other hand, in the film deposited by the eclipse method, one can see a drastic reduction of droplets and mirror-like surface in Fig. 3-5(b). A small object is located at the center in Fig. 3-5(b); it is not a droplet but a small dust particle which is released from the target and rebounds on the side bars of the apparatus to reach the substrate. However, the dust rarely deposits onto the substrate and helps to focus the microscope. Consequently, the STO film deposited by the eclipse method can be described as droplet-free.

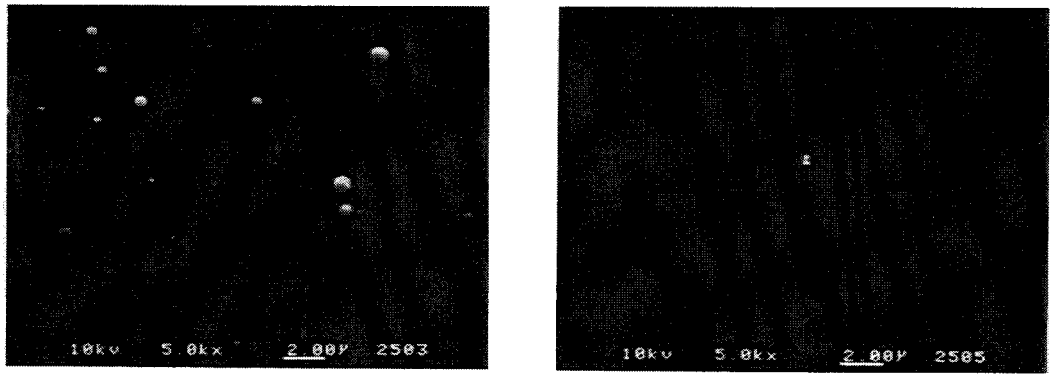

(a) (b)

Fig. 3-5 SEM images of grown STO surfaces : (a) without a shadow mask and (b) with a shadow mask.

So far, a serious situation has often happened to STO thin films grown by the conventional PLD method, in which we could not measure their capacitance in spite of enough thickness for insulation. It is not because the whole part of the films became conductive, but because the leak current was generated through the pinholes as explained above. This fatal defect was swept away by the introduction of the shadow mask in the eclipse PLD method, as is shown in Fig. 3-6. It is worth noting that the capacitance measurement of the samples whose thicknesses are in the range of 64–200 nm was successfully performed when the films were grown with the shadow mask. On the contrary, the films deposited (~200 nm in thickness) without the shadow mask showed low success probability of the capacitance observation. This result suggests the considerable reduction of droplets and particles which form the path of the leakage current.

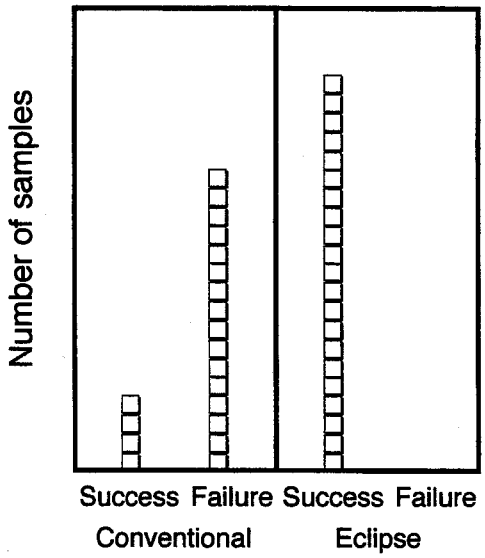

Fig. 3-6 Success probability of capacitance measurement of STO thin films deposited with and without a shadow mask.

3.4.2 Epitaxy of $SrTiO_3$ thin films

In this part, let us focus attention on the crystallinity of STO thin films grown on Pt films. We may leave the details of epitaxial STO thin films on YBCO to the former work reported by Taga *et al.*[15] Three kinds of STO thin films are examined here. They were deposited by (a) the eclipse PLD method on (100)Pt, (b) the rf magnetron sputtering on (100)Pt, and (c) the rf magnetron sputtering on (111)Pt, respectively. Their thicknesses are 40, 150, and 110 nm. For the deposition of the eclipse method in the present case, lowering of substrate temperature down to 500 °C was undertaken in order to prevent the mutual diffusion between the STO thin films and the substrates, and the ambient oxygen pressure was optimized to 0.2 Torr simultaneously. Other deposition parameters are the same as explained so far.

XRD and RHEED patterns which were observed immediately after the deposition of above three kinds STO thin films are shown in Figs. 3-7 and 3-8. As depicted in Fig. 3-7, the

thin films of (a) and (c) are oriented to <100> axis. In terms of the film (b), one can see that it is oriented preferably to <100> axis by taking account of the result of the ASTM cards: The intensity ratio of XRD from (100) to (110) planes of powdered STO polycrystal is 12:100, that is to say, the intensity from the (110) plane is much larger in uniformly oriented thin films.

In the RHEED pattern of the thin film (a), we can see that the STO thin film was grown epitaxially to <100> direction and keeps the ordering in plane, though it shows a three-dimensional growth. Looking at the RHEED patterns, the thin film (b) has the finest surface among them, and it shows the almost complete streak pattern which indicates long-distance ordering of this thin film. Diffraction from (110)-oriented planes does not appear on the pattern of thin film (b). In regard to the thin film (c), diffraction spots from (110)-oriented planes emerge as dimmer spots on the net pattern of the diffraction from (100)-oriented planes, which we cannot observe on its XRD pattern. Such distorted spots reflect a slightly weak ordering of the STO lattice over the entire substrate area. Here, the author must say that many of the samples fabricated in the condition (c) showed a small fraction (a few %) of the (110) orientation in the XRD patterns. Taking this fact into account, we can say the RHEED pattern of the thin film (c) seems to be a reasonable one.

Although there is no condition which is superior to others in every point of crystallinity, it is obvious that to deposit on (100)-oriented Pt is better than (111)-oriented one in the substrate selection from a point of view in which the crystallinity of layer-by-layer-grown thin films is considered. This idea shall be supported by the fact that the lattice constants of Pt and STO are quite similar (Pt: 3.923 Å, Sr: 3.904 Å). The situation of the STO thin films grown by the rf magnetron sputtering locates closer to the goal of the layer-by-layer growth than those by the eclipse method at present. However, it is only recently that the eclipse method has been proposed, and it is still under development today. Therefore, we can expect further improvements to the method in the future.

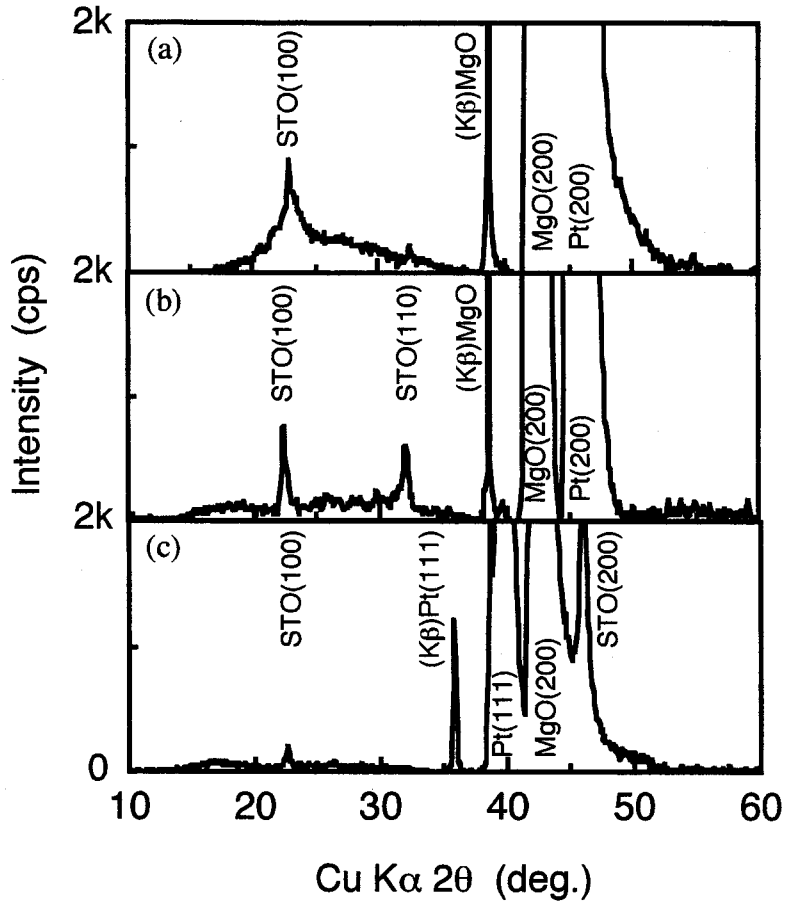

Fig. 3-7 XRD patterns of STO thin films grown by (a) eclipse PLD method on (100)Pt, (b) rf magnetron sputtering on (100)Pt, and (c) rf magnetron sputtering on (111)Pt.

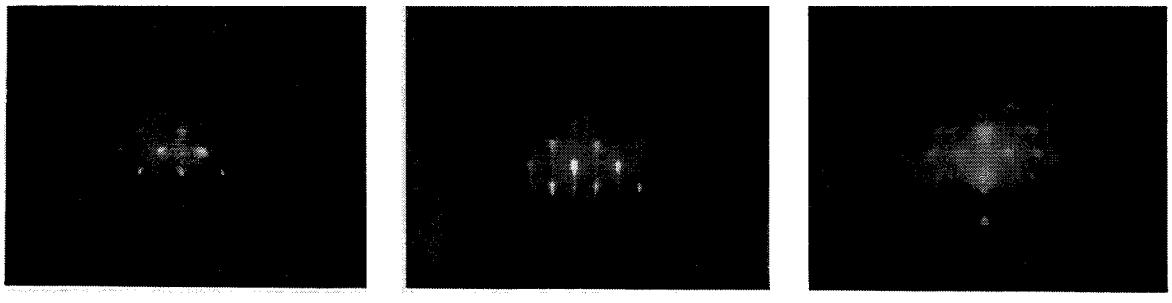

(a) (b) (c)

Fig. 3-8 RHEED patterns of STO thin films grown by (a) eclipse PLD method on (100)Pt, (b) rf magnetron sputtering on (100)Pt, and (c) rf magnetron sputtering on (111)Pt.

3.5 Summary

In this chapter, growth and crystallinity of STO thin films grown by the rf magnetron sputtering and the PLD method are discussed.

First of all, the brief review of both methods was given with an indication of the particles and droplets problem which is peculiar to the PLD method. Hence, in order to solve this intrinsic problem, an innovative technique, the eclipse method, which uses a shadow mask placed between the target and the substrate was proposed. In the technique, the deposition process proceeds with ablated species which are diffused with the assistance of the ambient gas.

Secondly, two substrate materials for the STO thin film growth, YBCO and Pt, were examined. In terms of YBCO, its (001)-oriented epitaxial thin films, which showed an excellent superconductivity, were obtained by the eclipse method on (100)MgO single crystals which were annealed in oxygen ambient at 1000 °C for 7 hours prior to the YBCO deposition. On the other hand, fine epitaxial Pt films were grown successfully on both (100)MgO single crystals which were pre-oxygen-annealed and non-annealed. The deposition of Pt thin films were carried out by electron beam evaporation and rf magnetron sputtering. Moreover, an interesting relationship between the orientation of epitaxial Pt thin films and the treatment of MgO substrates was disclosed: (111)-oriented Pt films are grown on oxygen-annealed MgO substrates, and on the other hand, (100)-oriented Pt films on non-annealed substrates. This work is first to reveal that the orientation of Pt films changes on (100)MgO single crystals with and without the pre-annealing treatment even when the deposition temperatures are identical.

Finally, STO thin films were fabricated on the substrates obtained in the above-mentioned manners, and their crystallinity was investigated by SEM, XRD, and RHEED methods.

The SEM observation made it clear that the surface smoothness was remarkably improved and that the scattered droplets and/or particles on the substrate surface are completely removed which caused the significant problem in the conventional PLD method. Since those anomalies caused or initiated the formation of pinholes which allowed the current leakage, the improvement of surface flatness led to a striking enhancement of success probability of the capacitance observation.

Next, the epitaxy of the STO thin films was examined by the XRD and RHEED patterns. Although the STO thin film grown by the eclipse PLD method on (100)Pt did not possess the long-range lattice ordering, it showed the fine (100)-oriented epitaxial growth. On the other hand, both of the STO thin films grown by the rf magnetron sputtering on (100) and (111)-oriented Pt films included a small amount of (110)-oriented composite. However, the STO thin film on (100)Pt substrate exhibited the almost complete streak pattern which indicated the two-dimensional growth where long-distance ordering was kept.

References

(1) A. Walkenhorst, C. Doughty, X. X. Xi, S. N. Mao, Q. Li, T. Venkatesan, and R. Ramesh, Appl. Phys. Lett. **60**, 1744 (1992).

(2) T. Hirano, T. Fujii, K. Fujino, K. Sakuta, and T. Kobayashi, Jpn. J. Appl. Phys. **31**, L511 (1992).

(3) J. Gong, M. Kawasaki, K. Fujito, U. Tanaka, N. Ishizawa, M. Yoshimoto, H. Koinuma, and M. Kumagai, Jpn. J. Appl. Phys. **32**, L687 (1993).

(4) T. Fujii, K. Sakuta, T. Awaji, K. Matsui, T. Hirano, Y. Ogawa, and T. Kobayashi, Jpn. J. Appl. Phys. **31**, L612 (1992).

(5) D. Roy, C. J. Peng, and S. B. Krupanidhi, Appl. Phys. Lett. **60**, 2478 (1992).

(6) H. Tabata, O. Murata, T. Kawai, S. Kawai, and M. Okuyama, Jpn. J. Appl. Phys. **31**, 2968 (1992).

(7) M. Tachiki, K. Yamamuro, and T. Kobayashi, Jpn. J. Appl. Phys. **35**, L719 (1996).

(8) H. Ishibashi, S. Arisaka, K. Kinoshita, and T. Kobayashi, Jpn. J. Appl. Phys. **33**, 4971 (1994).

(9) B. Holzapfel, B. Roas, L. Schultz, P. Bauer, and G. S. Ischenko, Appl. Phys. Lett. **61**, 3178 (1992).

(10) K. Kinoshita, H. Ishibashi, and T. Kobayashi, Jpn. J. Appl. Phys. **33**, L417 (1994).

(11) M. Iwabuchi, K. Kinoshita, H. Ishibashi, and T. Kobayashi, Jpn. J. Appl. Phys. **33**, L610 (1994).

(12) T. Awaji, K. Sakuta, Y. Sakaguchi, and T. Kobayashi, Jpn. J. Appl. Phys. **31**, L642 (1992).

(13) J. Narayan, P. Tiwari, K. Jagannadham, and O. W. Holland, Appl. Phys. Lett. **64**, 2093 (1994).

(14) P. C. McIntyre, C. J. Maggiore, and M. Nstasi, J. Appl. Phys. **77**, 6201 (1995).

(15) M. Taga, H. Miyake, and T. Kobayashi, Jpn. J. Appl. Phys. **33**, L1534 (1994).

Chapter 4
OPTICAL AND ELECTRICAL PROPERTIES OF HIGHLY POLARIZABLE $SrTiO_3$ THIN FILMS

4.1 Introduction

The optical properties of STO have been studied for a long time, and in particular in the 1960s, intensive studies on STO single crystals were promoted.[1 - 6] This material has strong absorption peaks in the infrared (IR) region. By the observation of these peaks, we can obtain information on atomic arrangements and interatomic forces in the crystal lattices because the absorption spectrum directly reflects the mutual interaction between the light (photon) and the lattice vibration of the crystal (phonon). Therefore, when considered inversely, one can see that a drastic change shall appear in the optical properties of STO crystal when its crystallinity is degraded. As discussed in Chapter 3, the ordering of STO crystal tends to loosen during thin film formation. Is it possible to detect a change in the crystal by the observation of its optical properties? In addition, it is suggested in Chapter 2 that the polarization properties become worse when the crystal contains a distortion. Is there a certain correlation between the optical properties and the electrical properties such as polarization?

While a lot of studies have also been done on the electrical properties of STO bulk so far, STO thin films have become the center of interest with the technological improvements in thin film fabrication in recent years, and the number of reports about STO thin films is growing year by year. Taking the electronics applications into account such as micro-size capacitors in ULSI-DRAM, we can say that obtaining a higher permittivity itself is significant. Further studies on electrical properties, such as polarization property dependence on each physical parameter or electrical behavior of carriers inside STO, can also contribute strikingly to the development of this material application.

In this chapter, IR spectra are observed and investigated by reflection absorption spectroscopy which is one of the most powerful techniques for thin film measurement, and its

relationship to the crystallinity is discussed. Subsequently, further studies on the electrical characteristics, including polarization properties, are investigated, and in addition, prominent polarization properties of STO thin films are introduced, which were obtained in the present work.

4.2 Analysis of Fourier Transform Infrared Spectroscopy

4.2.1 Reflection absorption spectroscopy

It is well-known that the sensitivity of spectrum observation of thin films increases when the they are coated on a flat surface of metals or semiconductors and the incident angle is large. The method using this advantage is called reflection absorption spectroscopy (RAS). It has recently been applied to studies on the optical properties and the orientation of considerably thin films (~a few 10 Å) of organic and inorganic substances.

As in Fig. 4-1(a), when a light vertically polarized is incident on a metal surface, the phase of the light wave is shifted at the reflection. The phase shift is about π, which is independent of the incident angle, and the polarized vectors of the incident and reflected lights cancel each other because of their opposite directions. Therefore, there is no mutual interaction between the light and the covering thin film, and the absorption does not appear on the spectrum.

In the opposite case, when a light parallel polarized is incident to a metal surface as in Fig. 4-1(b), the phase shift of the incident light varies and depends on the incident angle, which is zero when the angle is zero, and π when the angle is 90 degrees. The light forms a standing wave which is polarized vertically to the metal surface and undergoes absorption due to mutual interaction with the covering thin film. When the incident angle is large, the amplitude of the standing wave is also large, which leads to a strong interaction, hence the sensitivity increases.

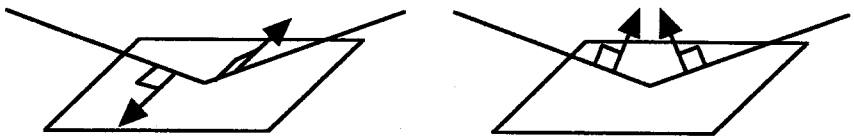

(a) (b)

Fig. 4-1 Reflection on a metal surface.

Because no electric field can exist parallel and adjacent to the metal surface and transverse modes cannot propagate in a very thin film on metal, one can principally observe the change of *p*-polarized reflectance which is essentially determined by the excitation of the longitudinal mode in the film.[7] The *p*-polarized reflectance with the frequency ω is expressed as

$$R \simeq 1 - \frac{8\pi d}{\lambda}\left(\mathrm{Im}\,\frac{1}{\tilde{\varepsilon}(\omega)}\right)\frac{\sin^2\psi_0}{\cos\psi_0}, \tag{4-1}$$

where d is the thickness of the film, λ is the wavelength, $\tilde{\varepsilon}(\omega)$ is the complex dielectric constant of the film ($\tilde{\varepsilon}(\omega) = \varepsilon_1(\omega) - i\varepsilon_2(\omega)$), and ψ_0 is the incident angle.

4.2.2 Deposition temperature dependence

In this part, a review is made of the fourier transform infrared (FTIR) spectrum characteristics of STO thin films, observed by the above-stated RAS method, and the spectrum dependence on the deposition temperature which was examined by Matsui *et al.*[8] Figure 4-2 shows the FTIR spectra of STO thin films deposited by rf magnetron sputtering on the (111)Pt/MgO substrates at temperatures ranging from 350 to 710 °C. The thickness of the

films ranged from 130 to 230 nm. Absorption peaks at 790 and 470 cm^{-1} are apparent in all spectra. These peaks are due to resonance with the longitudinal optic (LO) phonon modes associated with crystallinity of STO thin films. A number of optical analyses to single crystal STO bulk have been taken using the dispersion equation, and we can find one of them for STO thin films on Pd which was reported by Myoren *et al.*[9] The wave numbers of the spectra shown in Fig. 4-2 completely agree with those in these former reports. We can recognize readily a series of change of the FTIR absorption spectra against the deposition temperature in Fig. 4-2: The higher the deposition temperature until 665 °C, the higher and narrower the absorption peaks at 790 and 470 cm^{-1} wave numbers. The STO thin film deposited at 665 °C has the sharpest absorption peaks. With further increases in the deposition temperature, the peaks become lower and broader. According to the FTIR spectra and the dielectric properties of the STO thin films in the ref. (8), it is finally specified that the absorption intensity stems from the mutual interaction between the light and the thin films as explained above, and the absorption peak sharpness reflects the crystallinity of thin films and also becomes the measure of the quality of polarization properties. In this work, on the basis of the fact, film thickness dependence of the FTIR spectra is investigated and the crystallinity change inside the thin films is discussed in the next part.

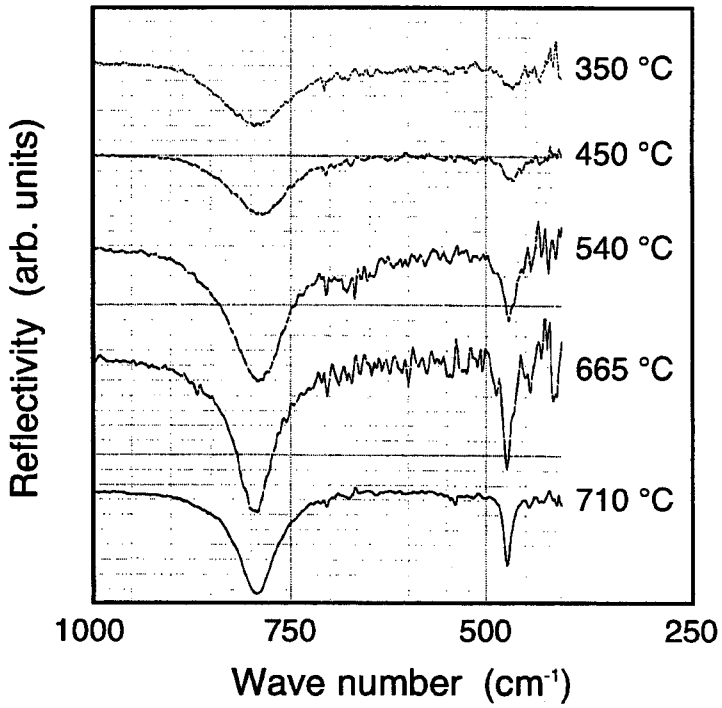

Fig. 4-2 FTIR absorption spectra from STO thin films deposited at various temperatures. Measurements were made in the reflection mode.

4.2.3 Film thickness dependence

It has been pointed out that when STO thin films are fabricated on Si or metal substrates, the degraded layer with low permittivity appears on the interface due to the lattice mismatch and/or the mutual inter-diffusion between the thin films and the substrates. The degraded causes a drop in the apparent polarization properties of the films. Thinking over the origin of the occurrence of the deteriorated layer adjacent to the interface, the lattices inside this layer are likely to deviate from the perovskite structure of ideal STO crystal. The existence of these distorted lattices is examined by the optical absorption spectra in this part. The information of the crystallinity alongside the interface was attempted to be obtained by decreasing the STO film thickness. In the present work, the incident angle of the RAS

method is 70 °, and it leads excellent sensitivity with which to observe quite thin films (~ a few 10 Å in principle).

Figure 4-3 shows the film thickness dependence of the FTIR spectra. All STO thin films were deposited by rf magnetron sputtering at 540 °C on (111)Pt/(100)MgO substrates as explained in Chapter 3. The film thickness was deduced by the direct measurement of the scanning tunneling microscope (STM): The STO films were selectively etched off by HF acid, and then covered by gold. The STO thicknesses grown were observed in the range of 3.5–262 nm. As in the last subsection, one can also see the obvious absorption peaks around 790 cm^{-1} in all spectra as well as some small peaks at 470 cm^{-1} in this figure. Even when the STO thickness is reduced as far as 11 nm, there is no drastic change in the peak wave number, the peak sharpness (the full width at half-maximum of the spectra), the ratio of the two peak intensities and so on. However, when the thickness is decreased to less than 11 nm, the absorption peak at 790 cm^{-1} is broadened to higher wave numbers. What does this phenomenon mean? Remaining internal stresses inside the STO thin films can not favorably explain the phenomenon, which was caused by the expansion coefficient gap between Pt and STO. It is because the STO film thicknesses are thin enough and there may be internal stresses of the same strength in all films in this experiment. The phenomenon of the spectra suggests the existence of a degraded layer on the interface between the STO thin films and the Pt substrates, which is also supported by the polarization properties of the films as shown later.

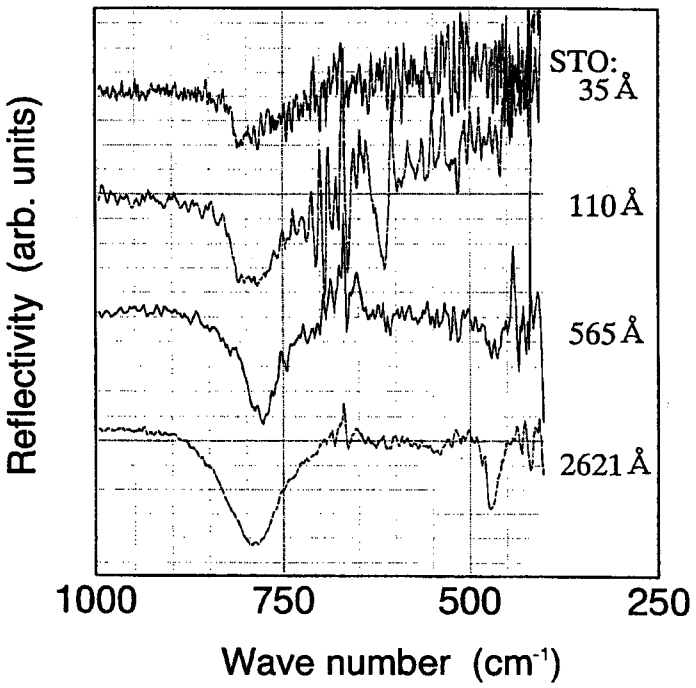

Fig. 4-3 FTIR absorption spectra from STO thin films. Measurements were made in the reflection mode.

4.3 Film Thickness Dependence of Dielectric Properties and Realization of Prominent Polarizability

Prior to the electrical measurement, Cr electrodes (0.0257 mm^2) were deposited by resistive-heat evaporation on the STO films which were fabricated on (111) and (100)Pt substrates. In addition, Pt was also deposited by means of electron beam evaporation at room temperature as another kind of upper electrode for the comparison. The current-voltage (*I-V*) and the capacitance-voltage (*C-V*) characteristics of the specimens were observed at room temperature. The measuring frequency of the capacitance was 1 MHz. The bias voltage was swung forward and backward, and it took 1 sec to make a round trip.

Figure 4-4 shows the *C-V* characteristics of the specimens that have various STO thicknesses *w* on (111)Pt. STO films on (100)Pt gave us the same characteristic as shown in this figure. Unfortunately, for the specimens with 3.5 and 11 nm STO thicknesses, the capacitance could not be measured because of the immense current leakage. This figure

indicates the internal electric field dependence of STO polarization which appears mostly with zero internal field. In other words, because of the work function difference between Cr (work function ϕ_{Cr} ~4.6 eV) and Pt (ϕ_{Pt} ~5.5 eV), the built-in field existed even at zero bias voltage, and the STO layer reached the flat band state which showed maximum capacitance C_{max} when –1 - –2 V was applied to the upper Cr electrode. This voltage magnitude is larger than the expected value that is deduced from the work function difference between Cr and Pt (~0.9 eV). This phenomenon can be understood if one knows the experimental result of the Pt/(100)STO/(111)Pt structure as shown in Fig. 4-5. As for the *C-V* curve of the Pt/STO/Pt metal-insulator-metal (MIM) system, there should be a maximum at the zero bias voltage because the upper and bottom electrodes have the same work function. However, the Pt/(100)STO/(111)Pt structure shown in Fig.4-5 needs an applied voltage of ~–0.7 V to reach the electric-field-free state. The peak shift might stem from the discrepancy between two interface conditions that arise from different fabrication processes. Taking this shift into account, the large magnitude of the above-stated voltage shift (1 - 2 V) of the Cr/STO/Pt structure can approach the expected value by a compensation of –0.7 V.

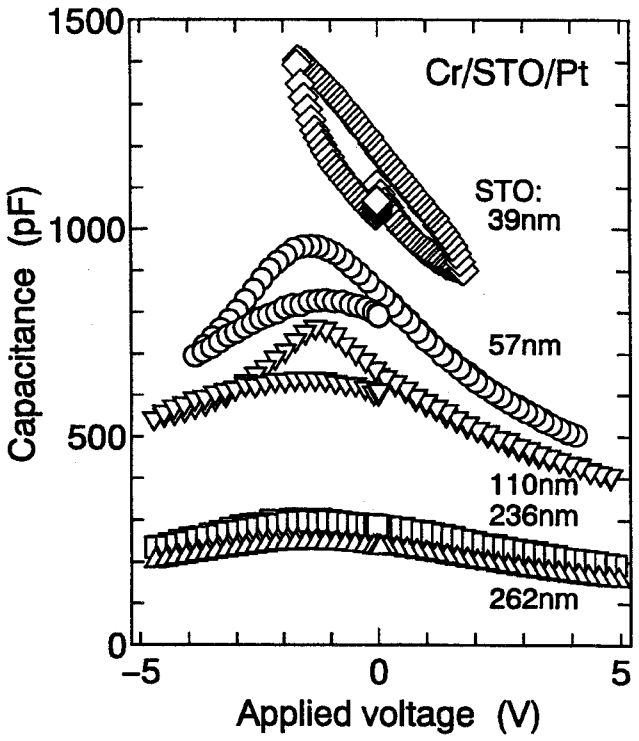

Fig. 4-4 Capacitance vs. voltage curves with various STO thicknesses.

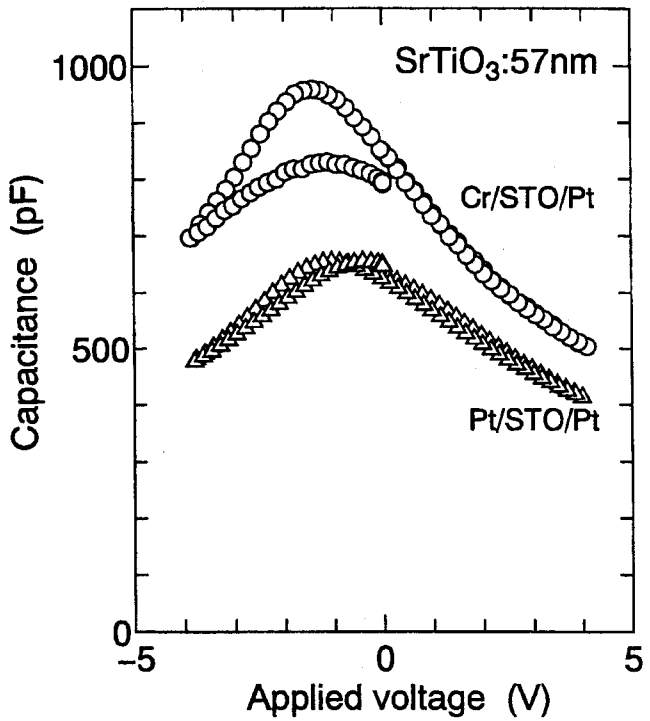

Fig. 4-5 Capacitance vs. voltage curves of Pt/STO/Pt and Cr/STO/Pt structures.

Strictly speaking, the STO thin films in this work exhibit hysteretic behavior to a certain extent, although it is a quantum paraelectric as mentioned before. The *C-V* curves of 57-nm- and 110-nm-thick STO layers transformed into others with smaller values of capacitance when the applied voltage made a round trip to and from the negative values. The insufficiency of STO crystallinity was thought to be slightly related to the decrease of capacitance. However, in the main, this phenomenon might be attributed to the occurrence of the high leakage current. In fact, appreciable leakage current was generated when the bias voltage of ~–4 V was applied to the specimen of a 57-nm-thick STO layer (see Fig. 4-6). The capacitance of these two specimens could never reach their former high values again after the leakage current. As for the *C-V* characteristics of the 39-nm-thick STO layer, we could not observe the capacitance at a deeply negative bias voltage because of the immense current flow.

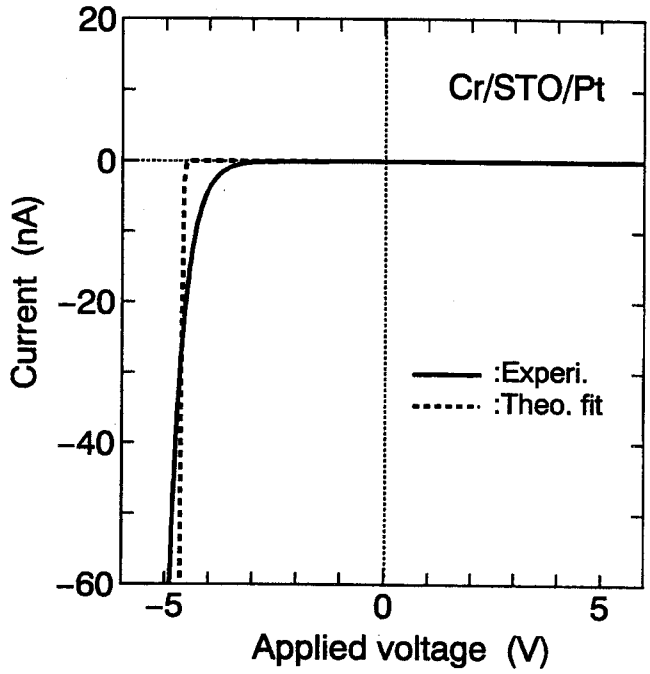

Fig. 4-6 Leakage current vs. voltage properties of Cr/(100)STO/Pt structure. Experimental data (—) and theoretical fitting curve (- -).

By using the elementary equation of a parallel-plate capacitor,

$$C_{max} = \varepsilon_{STO} S/w , \tag{4-2}$$

the permittivity of the STO layer ε_{STO} can be deduced, where S is the area of the Cr electrode of 0.0257 mm^2. Deduced permittivities of the STO films are indicated in Fig. 4-7. Although the figure seems to show a mountainous characteristic, it is attributed to the crystallinity randomness and does not exactly represent the polarization property of the STO thin films. In addition, the error which may occur during the measurement is negligible on the figure. As we see in the following discussion about the degraded layer with low permittivity, the STO thin films on the Pt substrates are supposed to show a sub-linear permittivity dependence on film thickness in which the permittivity increases steeply from the region of small thicknesses and saturates to a constant value, the permittivity of the fine part of the STO thin films, with larger thicknesses. The permittivity of $370\varepsilon_0$ was obtained in the 110-nm-thick film on (111)Pt, which is the highest value reported so far. Actually, the permittivity of the (100)-

oriented STO single-crystal bulk is ~357ε_0 at 10 °C,[10] being comparable or slightly lower than our present result. Consequently, we could say that we are reaching the top limit of the permittivity of STO thin films.

In addition, the thinner the STO film is, generally the more difficult it is to obtain a high permittivity.[11 - 13] A similar phenomenon has also been reported for films of other dielectric materials.[14] With regard to our films, the difficulty might be due to the existence of the thin degraded layer with a low permittivity at the interface between Pt and STO that was introduced during the deposition process. This poor quality layer acts as a series parallel-plate capacitor and pulls down the total value of the capacitance, thus concealing the high permittivity of the good quality STO region. This view came from a plot whose vertical and horizontal lines correspond to the reciprocal of capacitance, $1/C$, and the film thickness, w, respectively. This $(1/C)$-w plot becomes a straight line that lies on the origin when the STO permittivity is constant in the films. However, when we plot the data of this work and fit them with a straight line, the plotted data shifts upwards, away from the fitted line as the STO films become thinner. This makes it obvious that the parts of the STO layer adjacent to the interface have smaller permittivities. Moreover, in the previous section, we got an indication of the degraded layer in the FTIR spectra of the ultrathin STO films. Despite the general difficulty in obtaining a high permittivity for ultrathin STO films, which stems from the interfacial degraded layer, a fairly thin STO film of 39 nm showed a large value of 240ε_0.

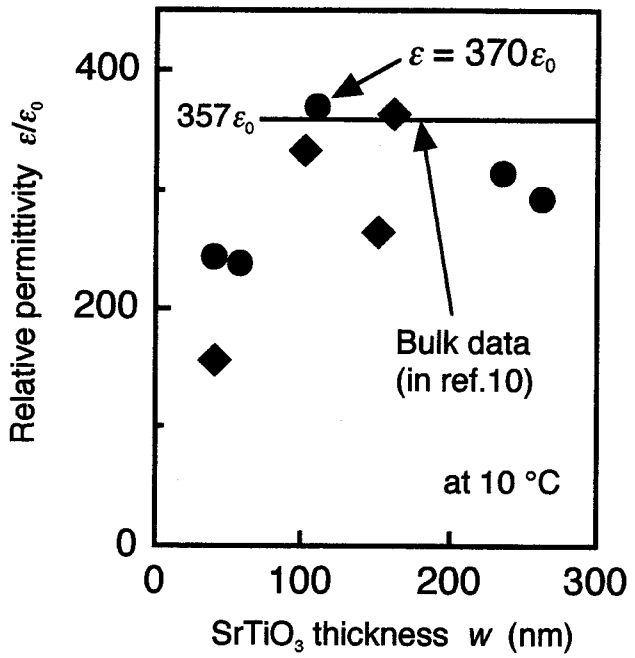

Fig. 4-7 Permittivities of various STO thicknesses. Circle is for STO films on (111)Pt substrate, and diamond is for STO on (100)Pt.

4.4 Analysis of Polarization Properties

4.4.1 Phenomenological approach and estimation of induced charge

Let us here consider phenomenological expressions for the description of the permittivity vs. electric field relation. The permittivity of STO is nonlinear.[15 - 18] It depends strongly on the internal field as well as the temperature. The dielectric properties of the (100)STO films have been studied intensively. As regards to materials such as STO that show nonlinearity of dielectric properties, it is much better to deal with the electric polarization P instead of the permittivity under the applied electric field E. Some papers have treated STO films in this way.[19] To describe the polarization behavior from the observed ε_{STO}-E data on Fig. 4-4, we shall use the polynomial approximation (in MKS units) given as follows, adding one more higher order term than before.

$$F = AP^2 + BP^4 + CP^6 + DP^8, \tag{4-3}$$

$$E = \frac{\partial F}{\partial P} = 2AP + 4BP^3 + 6CP^5 + 8DP^7, \tag{4-4}$$

$$\varepsilon_{STO} = \varepsilon_0 + \frac{\partial P}{\partial E} = \varepsilon_0 + \left(2A + 12BP^2 + 30CP^4 + 56DP^6\right)^{-1}, \tag{4-5}$$

where F is the free energy in the dielectrics. Parameters A, B, C, and D can be determined using the experimental data. As for the 110-nm-thick STO films, which showed the strongest polarizability, these four parameters at 10 °C were deduced as follows: A: 1.53×10^8, B: 2.0×10^9, C: -1.6×10^{10}, D: 1.0×10^{11}.

By applying the four deduced parameters to Eqs. (4-4) and (4-5), we obtained the internal electric field dependence of the permittivity and the total amount of polarization, which are plotted in Fig. 4-8 for the 110-nm-thick STO film. It shows that the polarization of the film in this work can reach a magnitude almost as great as 10^{14} cm^{-2}, which is very advantageous to the current modulation in the carrier-rich FETs, such as YBCO-MISFET (YBCO has very high sheet carrier densities of ~10^{14} cm^{-2} which are two orders higher than in familiar semiconductors).

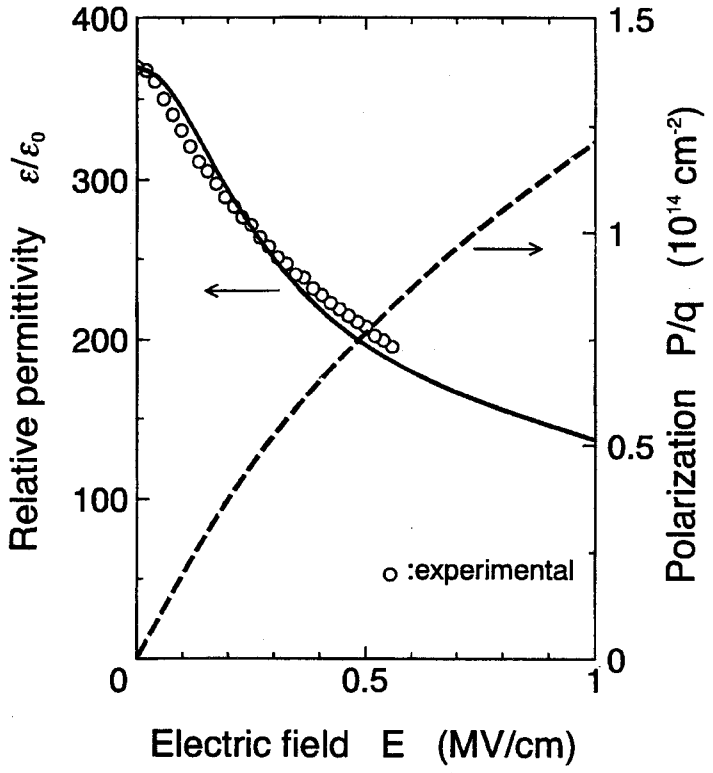

Fig. 4-8 Electric field dependence of STO permittivity and polarization.

4.4.2. Discussion of electrical properties of $SrTiO_3$ thin films

Asymmetric *I-V* curves have been obtained that showed the rectification of some MIM[20] or metal-STO-superconductor (MIS) junctions.[21-23] In the present work, the same result was also observed for the Cr/STO/Pt structure with a 57-nm-thick STO film, as plotted in Fig. 4-6. From the rectifying curves, one group suggested that a band model of the MIM structure where the STO film served as an n^+-type semiconductor and a Schottky barrier was contained within the STO layer.[20] If it were true, this model would warrant reconsideration of the problem. In other words, we have to use an equation different from Eq. (4-2) of a parallel-plate capacitor to deduce the STO permittivity. In particular, we have to note that the local field varies and depends on the distance from the surface, and so does the permittivity in

the Schottky band model. All these things make it clear that the determination of the band model of STO thin film is essential for its physical investigation.

Figures 4-9(a) and 4-9(b) represent the possible band diagram with a Schottky barrier of the metal-insulator-other metal (MIM') structure and its equivalent circuit, respectively. When we measure the capacitance of the junction, the real circuit can be regarded as a schematic one illustrated in Fig. 4-9(c), and we measure the net capacitance C_{net}, which consists of the capacitance of the depletion layer C_d, the junction resistance R_j, the capacitance of the residual area of STO C_r, and the resistance of the residual area of STO R_r. In the residual region, the charges are in the neutral state with zero bias voltage. Consequently, it is not until we solve the complicated equation of the net capacitance where many factors are mixed (given later in Eq. (4-9)), that we can deduce the real STO permittivity. If the Schottky barrier model were valid, all STO permittivity that have been reported before would have to soon be revised by the above equation. Therefore we could say it again that there is a strong need to investigate and manifest the exact band diagram of the STO MIM' structure.

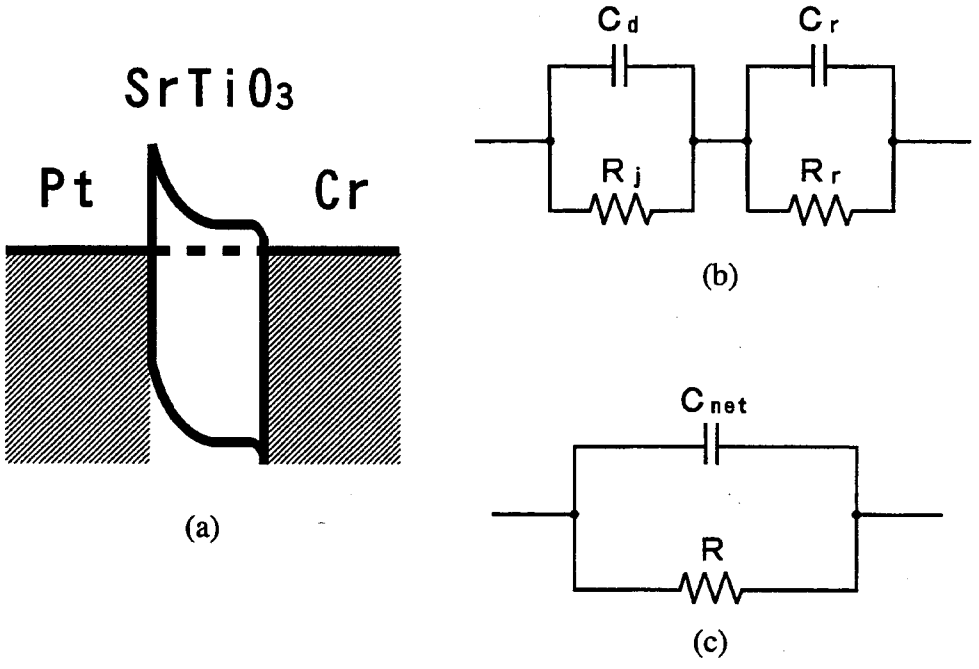

Fig. 4-9 Possible band diagram of Cr/(100)STO/Pt structure and its equivalent circuits. (a) STO layer contains space charges, and as a result, a Schottky barrier is built up inside it, (b) equivalent circuit, and (c) regarded circuit in the capacitance measurement. The capacitance meter actually shows C_{net}.

It is worth noting that another ordinary band model that includes no space charge, on the other hand, is not inconsistent with the asymmetric *I-V* curves. The model shown in Fig. 4-10(a) agrees well with the rectification in the following way. As for ordinary oxide insulators such as SiO_2, the leakage current is determined mainly by the tunneling effect. However, comparing the energy gap of STO single crystal with that of SiO_2, STO has a much smaller value of ~ 3.2 eV,[24,25] whereas SiO_2 has an energy gap as large as 8.8 eV. In fact, it is also true for other oxide ferroelectrics such as $BaTiO_3$ and $CaTiO_3$ that have much smaller energy gaps. In addition, the electron affinity of the STO single crystal is close to that of Cr.[26] The leakage current is thought to be governed by another mechanism. Figure 4-10 represents the rectification of the Cr/STO/Pt structure. In the equilibrium state, as illustrated in Fig. 4-10(a) with zero bias voltage, currents have the same value flow in opposite directions. Hence, the net current is zero. When negative or positive voltages are applied to Cr, as shown in Figs. 4-10(b) and 4-10(c), respectively, the carrier distribution is changed according to Boltzmann statistics. If the current direction from Cr to Pt is chosen as positive and the Pt electrode is chosen as the ground level, the leakage current I is given by

$$I = -I_0\left\{\exp\left(-\frac{qV}{k_B T}\right) - 1\right\}, \tag{4-6}$$

where I_0 is the saturation current, q is the elementary charge, k_B is the Boltzmann constant, and T is the temperature. This expression ignores the injection of carriers to the STO layer from the side metals and the scattering effect inside the STO layer for the sake of simplicity. The leakage current characteristic of the space-charge-free model is identical to that of the aforementioned Schottky barrier model. Finally, with regard to the *I-V* curve, one can conclude there is no difference between the two models.

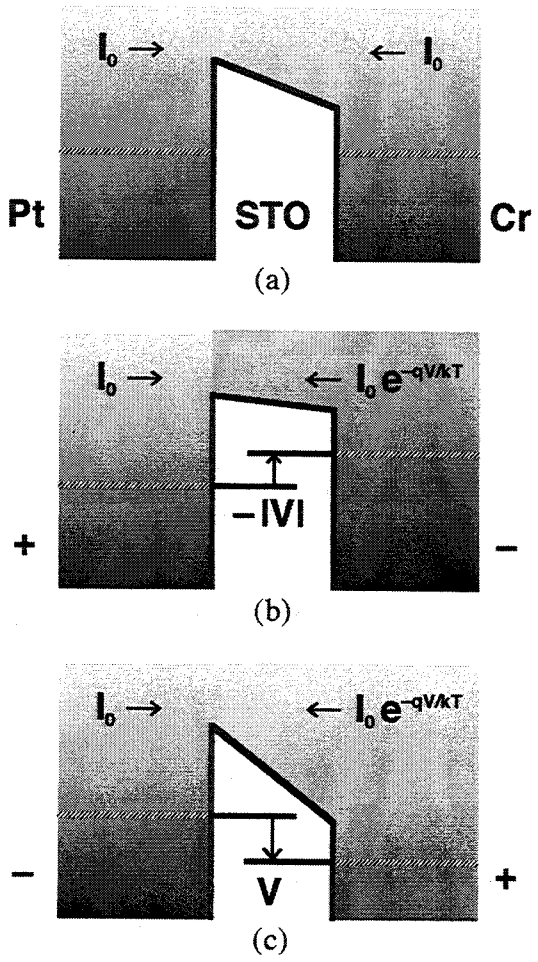

Fig. 4-10 Possible band diagram concerning the rectification of Cr/(100)STO/Pt structure. STO layer has no space charge. (a) No bias voltage, (b) negative, and (c) positive bias voltages applied to Cr.

Incidentally, it is of importance to examine whether the former equation matches the observed *I-V* curve. Because of the considerably high resistivity of our STO films, the confirmable leakage current does not occur up to high negative voltages, as indicated in Fig. 4-6. Therefore the theoretical equation cannot fit the observed curve at high voltages because of the steep rise due to the exponential term in Eq. (4-6). One can see the moderate rise of the observed result. This property might stem from the spatial smearing of the STO band gap. In addition, the possibility of other mechanisms of leakage current such as the space-charge-limited current or Poole-Frenkel emission[12, 13] were considered. Figure 4-11 shows the

experimental *I-V* curve and a theoretical fit in the applied voltage levels under –2 V (this figure is drawn with absolute values). Ideally, the space-charge-limited current is proportional to the square of the applied voltage. On the contrary, the result of this work is proportional to about the fourteenth power of the applied voltage. Moreover, the magnitude of the experimental leakage current in the voltage levels of Fig. 4-11 is actually much smaller than the theoretical one (in Fig. 4-11, the theoretical curve of space-charge-limited current is drawn only for comparison of the slope). Therefore the experimental data in this figure is out of the scope where we can treat the leakage current as the space-charge-limited current. The *I-V* curve, in accordance with Poole-Frenkel emission, cannot fit the experimental one either. The discrepancy between the experimental data and the theoretical curves might be explained by assuming the existence of many local levels at the interface. These local levels might relate to the unintentional introduction of the degraded interfacial layer with low polarizability as pointed out earlier that pulled down the measured capacitance, especially of the thinner STO films.

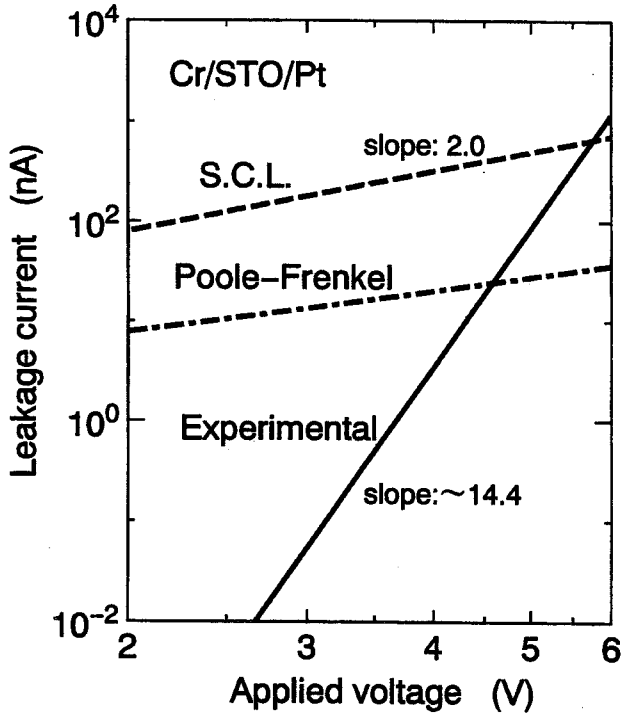

Fig. 4-11 Leakage current vs. voltage properties of Cr/(100)STO/Pt structure (absolute values). Experimental data (—) and theoretical fitting curves (space-charge-limited current: broken line, Poole-Frenkel emission: dashed-and-dotted line).

Although the details of the *I-V* property are still open to discussion, there is no principal difference between the theoretical *I-V* property of the two band models as mentioned before. Let us focus on the *C-V* property next. There is a pronounced difference between the theoretical *C-V* curves of the two models.

Figure 4-12(a) shows the theoretical *C-V* curves of the Schottky band model. One can explain the rectifying *I-V* curve by the formation of a Schottky barrier at the STO/Pt interface by treating the STO as an n^+-type semiconductor. Therefore we consider the donor concentration of the n^+-STO layer. In the calculation, the Schottky barrier height $q\phi_b$ was set at about 1 eV from another group's experimental result.[20] As for the permittivity, the preceding four dielectric parameters (*A*, *B*, *C*, and *D*) were used. Regarding other parameters for STO, pertinent values were chosen as follows: temperature T : 300 K, measuring frequency f: 1 MHz, density of donors N_D: 1×10^{19} cm^{-3}, and mobility μ : 7 cm^2/Vs.

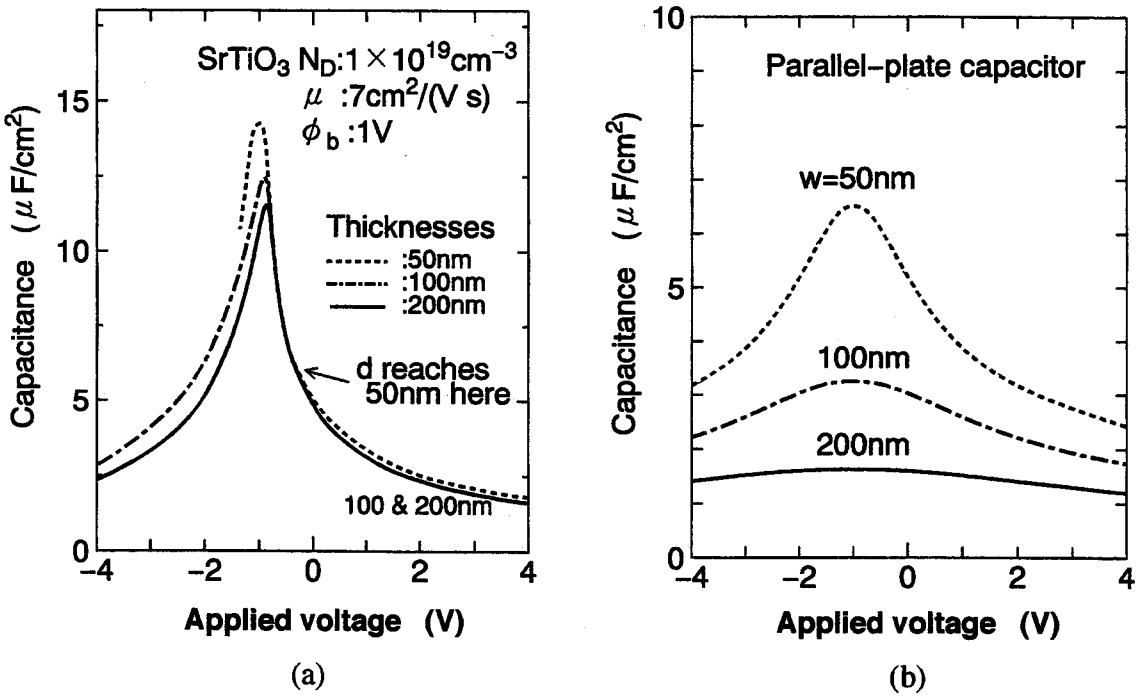

Fig. 4-12 Theoretical capacitance vs. voltage curves.
(a) Schottky band model and (b) space-charge-free model.

In Fig. 4-12(a), there are three curves for different thicknesses of the STO layer. These curves were calculated on the basis of the following equations:

$$\nabla\cdot(\varepsilon_{STO}E) = qN_D, \tag{4-7}$$

$$J = -A^*T^2\exp(-\beta\phi_b)[\exp\{-\beta(V - V_r)\} - 1], \tag{4-8}$$

$$C_{net} = \frac{G_j^2C_r + G_r^2C_d + \omega^2C_dC_r(C_d + C_r)}{(G_j + G_r)^2 + \omega^2(C_d + C_r)^2}, \tag{4-9}$$

where J is the current density, $A^* = 120$ A/cm^2/K^2 is the Richardson constant, V_r is the voltage of the STO neutral charge area, and $\omega = 2\pi f$ is the angular frequency. C_d and C_r are the capacitances of the depletion layer and the residual layer, respectively, depending on the internal field of each layer. G_j and G_r are conductances which are given as $G_j = 1/R_j$ and $G_r = 1/R_r$. In the calculation, one can decide the distribution of the internal electric field using ε_{STO}, q, and N_D from Gauss' theorem with Eq. (4-7). Then the width of the depletion layer can be decided by making the integration of the deduced internal electric field equal to the magnitude of the voltage placed between both sides of the depletion layer. One must consider the nonlinearity of the dielectric property in the calculation at all times because the internal electric field and the permittivity change constantly, even in a small area, due to the nonlinearity.

The density of donors looks large, but if we make this number smaller, the depletion width d increases proportionally to the reciprocal of the square root of the donor concentration. If the number is small enough, the depletion layer reaches the thickness of the STO film w and exceeds it. This situation where d is larger than w does not meet the condition of the Schottky band model in which the Schottky barrier is contained within the STO layer. In the present condition, the density of donors is large enough for a depletion layer thinner than the 50-nm-thick STO film at zero bias voltage. However, despite this large number of donors, d can reach w by applying reverse (it is positive in Fig. 4-12(a)) bias voltages. This behavior is shown in the same figure for the 50-nm-thick STO layer. After the depletion layer contacts the Cr electrode metal, the nature of the C-V curve changes. Inversely, if we make the density of donors larger to fit the experimental results, it may be impossible to measure the capacitance because a large amount of current begins to flow when we raise the applied forward bias (it is negative in the figure). This condition does not

conform to the actual situation. Consequently, we assigned the density of donors as 1×10^{19} cm^{-3} in the calculation. Even in this condition, the current density of the 50-nm-thick STO film reaches more than 1×10^{6} A/cm^{2} at the left end of the applied voltage of –1.3 V.

In addition, one can see a slight decrease of the maximum capacitance as the thickness becomes larger in Fig. 4-12(a). These calculated results of the Schottky band model are completely inconsistent with the experimental results (see Fig. 4-4). In fact, the experimental result demonstrates that the maximum capacitance is inversely proportional to the STO thickness as drawn in Fig. 4-13. Moreover, one can see steep slopes of these theoretical curves of the Schottky model. This feature is not consistent with the experimental one either. It stems not only from the internal field dependence of the STO permittivity, but also from the rapid change in the depletion layer width with the applied voltage.

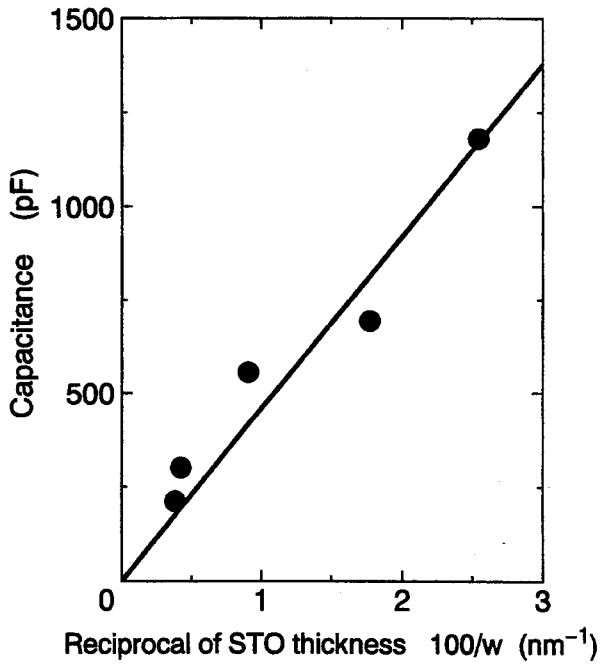

Fig. 4-13 Inversely proportional relationship of STO thickness vs. capacitance.

Let us examine the band model without space charges next. Figure 4-12(b) shows the theoretical *C-V* curves of this model. In the calculation, the Cr/STO/Pt structure is equivalent to a parallel-plate capacitor. Concerning the STO permittivity, the identical method is used with the former equations and the four parameters, A, B, C, and D. In Fig. 4-12(b), one can see the inverse proportionality of the capacitance against the STO thickness which can be easily described by Eq. (4-2). The characteristics of these curves resemble the experimental results of the present work (see Figs. 4-4 and 4-13) and others' fairly well. Finally, we can conclude that the STO thin films are substantially without space charges. The author strongly supports the space-charge-free band diagram of Fig. 4-10(a) as appropriate.

4.5 Summary

In this chapter, IR spectra were observed and investigated by RAS, which is one of the most powerful techniques for thin film measurement, and their relationship to the crystallinity was discussed.

In review, the absorption intensity stems from the mutual interaction between the light and the thin films, and the absorption peak sharpness reflects the crystallinity of thin films and also becomes the measure of the quality of polarization properties. On the basis of this fact, film thickness dependence of the FTIR spectra was investigated and the crystallinity change inside thin films was discussed.

Obvious absorption peaks were seen around 790 cm^{-1} in all spectra as well as some small peaks at 470 cm^{-1} which are in complete agreement with previous reports. Even when the STO thickness was reduced as far as 11 nm, there was no drastic change in the peak wave number, the peak sharpness , the ratio of the two peak intensities and so on. However, when the thickness was decreased to less than 11 nm, the absorption peak at 790 cm^{-1} broadened to higher wave numbers. It suggested the existence of a degraded layer on the interface between the STO thin films and the Pt substrates.

Subsequently, further studies on the electric characteristics, including polarization properties, were carried out.

The *C-V* curves of the STO films indicated the internal electric field dependence of permittivity which became most with zero internal field. The permittivity of the STO thin films reached as high as $370\varepsilon_0$ at room temperature. Moreover, despite the general difficulty in obtaining a high permittivity for ultrathin STO films, a fairly thin STO film of 39 nm also showed a large value of $240\varepsilon_0$.

Phenomenological expressions were given for the description of the permittivity vs. electric field relation. By means of the expressions, it was disclosed that the polarization of the STO thin films in the present work could reach a magnitude almost as great as 10^{14} cm^{-2}.

Comparing the experimental *I-V* and *C-V* curves of the Cr/(100)STO/Pt MIM' structure to theoretical results, two possible band models, with and without space charges were discussed, and finally, it was concluded that the band diagram which has no space

charge is appropriate for the description of the Cr/(100)STO/Pt MIM' structure.

References

(1) A. S. Barker, and M. Tinkham, Phys. Rev. **125**, 1527 (1962).

(2) W. G. Spitzer, R. C. Miller, D. A. Kleinman, and L. E. Howarth, Phys. Rev. **126**, 1710 (1962).

(3) A. S. Barker, and J. J. Hopfield, Phys. Rev. **135**, A1732 (1964).

(4) M. Cardona, Phys. Rev. **140**, A651 (1965).

(5) W. S. Baer, Phys. Rev. **144**, 734 (1966).

(6) M. I. Cohen, and R. F. Blunt, Phys. Rev. **168**, 929 (1968).

(7) D. W. Berreman, Phys. Rev. **130**, 2193 (1963).

(8) K. Matsui, M. Taga, and T. Kobayashi, Jpn. J. Appl. Phys. **32**, L796 (1993).

(9) H. Myoren, T. Matsumoto, and Y. Osaka, Jpn. J. Appl. Phys. **31**, L1425 (1992).

(10) R. C. Neville, B. Hoeneisen, and C. A. Mead, J. Appl. Phys. **43**, 2124 (1972).

(11) S. Yamamichi, T. Sakuma, K. Takemura, and Y. Miyasaka, Jpn. J. Appl. Phys. **30**, 2193 (1991).

(12) T. Kuroiwa, T. Honda, H. Watarai, and K. Sato, Jpn. J. Appl. Phys. **31**, 3025 (1992).

(13) P. C. Joshi, and S. B. Krupanidhi, J. Appl. Phys. **73**, 7627 (1993).

(14) C. Feldman, J. Appl. Phys. **65**, 872 (1989).

(15) D. Roy, C. J. Peng, and S. B. Krupanidhi, Appl. Phys. Lett. **60**, 2478 (1992).

(16) T. Hirano, M. Ueda, K. Matsui, T. Fujii, K. Sakuta, and T. Kobayashi, Jpn. J. Appl. Phys. **31**, L1345 (1992).

(17) K. Abe, and S. Komatsu, Jpn. J. Appl. Phys. **32**, 4186 (1993).

(18) R. A. van der Berg, P. W. M. Blom, J. F. M. Cillessen, and R. M. Wolf, Appl. Phys. Lett. **66**, 697 (1995).

(19) J. H. Barrette, Phys. Rev. **86**, 118 (1952).

(20) K. Abe, and S. Komatsu, Jpn. J. Appl. Phys. **31**, 2985 (1992).

(21) J. Mannhart, J. G. Bednorz, K. A. Müller, and D. G. Schlom, Z. Phys. **B83**, 307 (1991).

(22) T. Fujii, K. Sakuta, T. Awaji, K. Matsui, T. Hirano, Y. Ogawa, and T. Kobayashi, Jpn. J. Appl. Phys. **31**, L612 (1992).

(23) A. Walkenhorst, C. Doughty, X. X. Xi, S. N. Mao, Q. Li, and T. Venkatesan, Appl. Phys. Lett. **60**, 1744 (1992).

(24) K. W. Blazey, Phys. Rev. Lett. **27**, 146 (1971).

(25) J. Gerblinger, and H. Meixner, J. Appl. Phys. **67**, 7453 (1990).

(26) V. E. Henrich, G. Dresselhaus, and H. J. Zeiger, Phys. Rev. **B17**, 4908 (1978).

Chapter 5
INVESTIGATION FOR HIGHER POLARIZATION PROPERTIES

5.1 Introduction

Most materials which have been discovered so far to exhibit excellent polarization properties have perovskite and related structures. STO is one of them. It has been indicated that the reason why the perovskites can show such good properties attributes to the occurrence of the effective local fields which are caused by their structural asymmetry. Is it impossible to create a new material in which this effect of polarization is successfully enhanced? To date, a number of attempts have been considered to create noble materials with supereminent physical properties. In regard to materials with higher polarization properties, there were several trials such as the replacement of ions in crystals, structural control with superlattices, and so on.[1-5] These attempts are still under development at present. However, a difficulty arises here: There are countless candidates for new materials, and no one can clearly define the best way to obtain these outstanding new materials. The real world where we live has the same nature – the "non-equilibrium open system" where anything may happen. Hence no one can predict exactly what will happen in the future in this world. In spite of infinite possibilities, living things seems to exist in a state of equilibrium (i.e., holding beneficial shapes which adapt themselves to surroundings) when we pick a certain period. This phenomenon is owed to biological evolution. The central theme from now is to include the idea of evolution in the above-stated creation of new materials.

In this chapter, firstly, we shall discuss the expected features of noble materials, how superb polarization properties are realized, through the investigation of perovskite as a representative of highly polarized materials. This discussion is quite important and provides a guiding principle to the quest for new materials. Secondly, this quest is executed in two systems with genetic algorithm which came from the idea of evolution. The first system is a simplified model of crystals and the second one is of crystals which consist of real ions.

Finally, proposals for new materials with prominent polarizability are presented according to the results obtained by the quest simulation.

5.2 Origin of Prominent Polarization Properties

As explained in Chapter 2, perovskite structure shows quite excellent polarization properties. Why or how can it display such good properties? The asymmetry of the local field holds the key to the question. Let us look back at Eq. (2-5). There are two finite values, p and q, which are zero in symmetric structures such as rock-salt. Because the two parameters are large, the Lorentz field greatly differs from $(4\pi/3)P$. In particular, we can see that the mutual interaction between dipoles of Ti and O_a ions is strong in Eq. (2-5). Practically, the value of $4\pi(q+1/3)$ is about as much as 8.2 times larger than $4\pi/3$. Let us here concretely examine the situation. We shall firstly suppose a case in which the dipoles on the O_a sites become larger. It leads the increase of the local fields on the Ti sites. Due to the local field increase, the dipoles on the Ti sites are enlarged. It causes growth of the local fields on the O_a sites. Finally, the grown local fields enlarge the dipoles on the O_a sites, and the situation returns to the starting condition. In short, the mutual interaction between Ti and O_a dipoles stands on a positive-feedback relation, and the more the dipoles polarize, the more the polarizations enhance each other. This is exactly the key to the outstanding polarization properties for the perovskite structure. In fact, it has been proposed in a previous paper that a large part of the net polarization comes from that of Ti-O_a chains in the perovskite structure.[6]

In the following parts of this chapter, a new technique of pursuing superior polarization properties is introduced on the basis of the idea of the origin of prominent polarizability which was obtained here.

5.3 Discussion of Superb Polarizability with Genetic Algorithm

5.3.1 Principle of genetic algorithm[7-10]

Darwin reached a notion of *natural selection* through his experiences on the Beagle and the concept of Multhus' theory, and after the more-than-20-year development of his idea, he finally published *The origin of Species* in 1859. As he pointed out in his book, the real world we live in is changing every moment and living things adapt themselves to their surroundings and survive through the process of evolution in this continuous change. After Darwin, as represented by the elucidation of the DNA double helix structure of Watson and Crick in 1953, studies on molecular gene biology have been energetically advanced and the detailed process of evolution has become clearer. For example, it is well-known today that antibiotics are designed against certain kinds of viruses, and yet viruses evolutionally acquire patience against newly organized antibiotics. In this case, it can be said that the circumstances around antibiotics have changed. Inversely, viruses do not know previously what kind of antibiotics shall be injected. We can see that viruses cope with antibiotics with the help of the evolutionary effect. The evolution is one of the satisfactory answers to the problems like this. No matter how much the surroundings may change, some species can successfully cope with them through processes such as mutation or recombination of DNA.

Genetic algorithm (GA) is an engineering technique which has been developed from the idea of the above-explained biological evolution. In the GA, firstly, groups are prepared consisting of individuals that have randomly selected genes. Each individual is created according to the gene sequence. Secondly, it is evaluated how much they can adapt themselves to the surroundings. The more they can adjust, the easier it is for them to survive and leave their descendants. Thirdly, they choose their own partners, mate with them and reproduce a new generation. During the reproduction, some genes suffer from the transformation due to the mutation. These processes are repeated over and over again, and through the iteration, the group members eventually improve to adapt to the circumstances.

Let us examine the GA with a simple example here. We shall set the genes of individuals which can be described by five digits like "01001", for example, which consists of the two numbers, 0 and 1. The adaptation in the surroundings is supposed to be expressed by an equation. In the case here, we shall evaluate that the more they have the element "1" in their genes, the superior they are in the world. Properly speaking, an individual called a

phenotype is created by genes, and the evaluation of its adaptation depends on its activities in the world. However, for the sake of convenience, we shall directly evaluate the gene information in this simple example. For instance, the evaluation is 1.0 when the gene sequence is "11111", and is 0.0 when the sequence is "00000".

Let us decide the first generation at random as shown in Fig. 5-1. In this case, according to the way of thinking that the more an individual has the element "1" in its gene, the higher the evaluation is, the evaluation values of individuals are derived as shown in the figure. Next, we have to think of reproduction, and we shall suppose that the higher the evaluation of an individual, the higher its possibility to leave descendants. The individuals with low evaluations cannot be selected, and the individual which has the "00100" gene cannot leave its descendants in the first generation in the case of Fig. 5-1. Selected individuals cross over their own genes with mates. In the example, the location of the crossover is decided randomly, and the individuals with genes of "10100" and "11001" are rearranged together. Finally, mutation is involved at casual sites on the genes. The result after all procedures is the second generation. When we assess the second generation, the average evaluation is 0.65 which is much greater than that of the first generation of 0.4, and one can see that adaptation to the surroundings occurs. Repeating the shift of generation many times, the group grows, which consists of individuals successfully adapting to the given world.

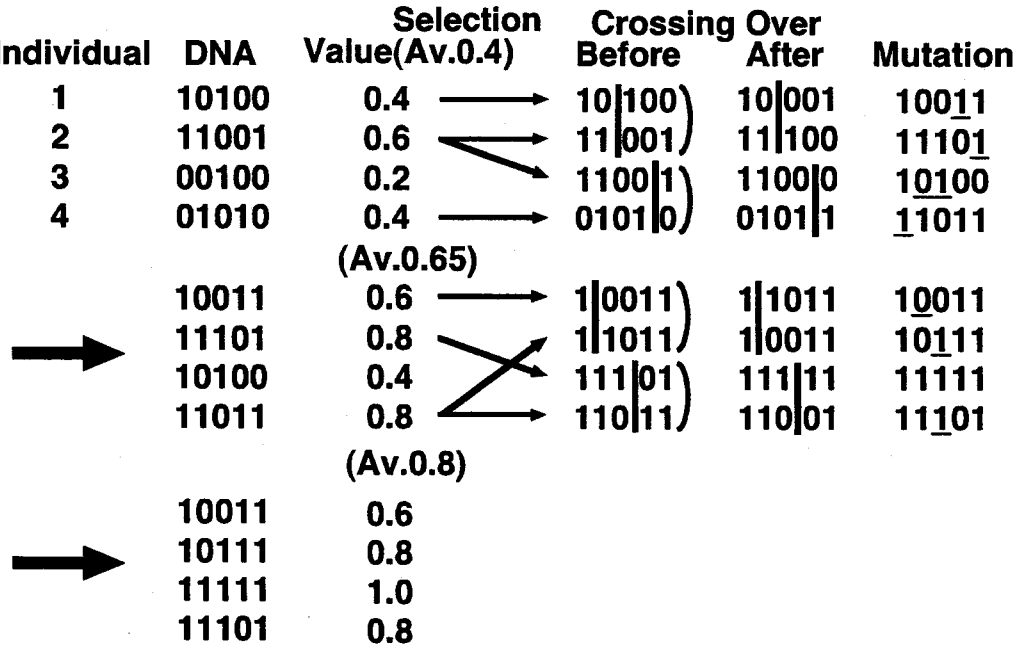

Fig. 5-1 Principle of genetic algorithm with generation shifts.[7]

The GA is a technique which automatically operates these procedures on a computer. It is desirable for us to be able to apply the GA with the defined evaluation to a problem even when the best answer for it is unknown. This process is exactly evolution. Although no one knows the best answer for adapting to our environment, we have acquired rather adequate forms through the evolutionary process of trial and error. Here we have to note that the GA takes modeling for simplicity. In reality, the biological evolution comprises more complicated processes. Despite the simplicity, the GA still has succeeded in a number of fields because the algorithm only treats the core idea of evolution and refines it in the manner of engineering.

5.3.2 Pursuit of excellent crystals

Here, a technique to pursue highly polarizable crystals is introduced, whose concept has been proposed by the author according to GA techniques.

How can we apply the notion of biological evolution to inorganic crystals? From now on, we shall treat crystals as living things. Of course, they cannot walk or eat, but we will consider that the prominence in polarization properties brings them a serenity in their lives. They organize groups which consist of members whose features are identical. Among these groups, the superiors prosper and their number of constituent members grows. We shall become a god and sometimes give them a harsh ordeal such as mutation. However, in principle, we have only to observe the transition of their generations. They will evolve spontaneously. When, after a long time, we pick up and look over the characteristics of members of groups which have thrived, we will ascertain a great number of keys to prominent polarizability among them.

Let us move on to a concrete discussion. Figure 5-2 describes the scheme of the quest for high polarizability with GA which is carried out in this work. Because the concept of this algorithm was created by the author, there are some intentional ideas. Yet the main point of view of the simulation is firmly situated on evolution. Further discussion of detailed refinement will be presented later. For now let us focus attention on the basic concept of the quest for highly polarizable crystals with the explanation of each procedure in the calculation.

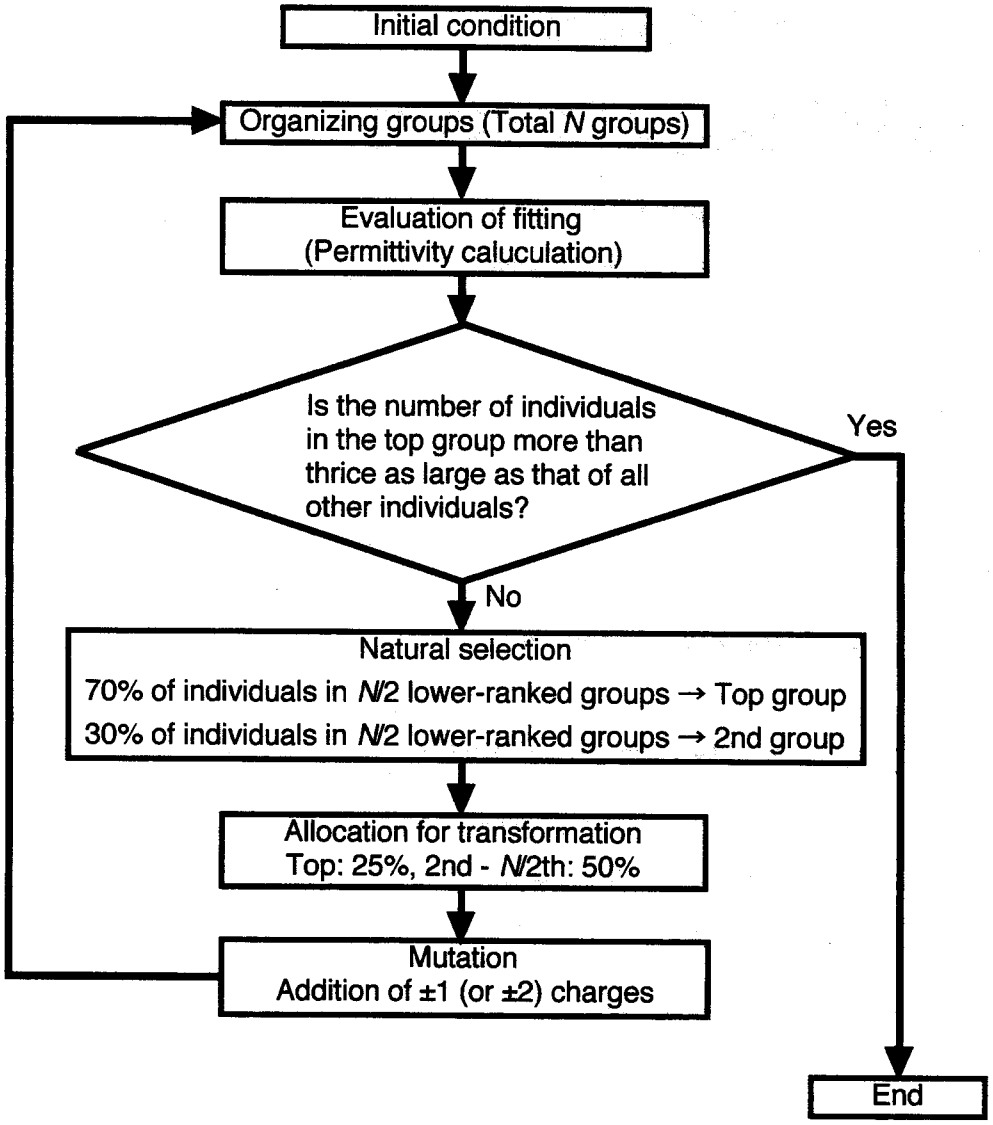

Fig. 5-2 Scheme of quest for highly polarized materials with genetic algorithm.

First of all, a primitive world is given as the initial condition, which is set at naught in the calculation. In other words, no crystals have ions at all at the initial stage. The permittivity of these crystals is that of free space, ε_0, and it means the poorest polarization properties. Secondly, groups are organized consisting of members whose characteristics, including their orientations, are identical. Although all crystals must belong to one group at the initial stage according to this treatment since no crystals have ions, only the completely-

ion-less crystal is decided not to flock together. Thirdly, the permittivity of each crystal is calculated, where the electric field is applied toward the z direction. The derived permittivity represents the adaptability of the crystal creatures to the surroundings in the world, and the more it is, the more the survival probability is set to be. Each group is ranked in accordance with the evaluation of adaptability. In the fourth procedure, we will act as "God", that is to say, we will check whether several species which successfully adapted to the world were born and flourished or not. When there exist such crystals, the simulation is ended. On the other hand, when crystals are not in a stable stage, we will move on to the next step. Fifthly, natural selection is carried out. In other words, we shall consider that lower-ranked groups become extinct and the top two groups thrive and immigrate into the vacant region where the extinct species dwelt before. From the sixth procedure, preparation for the next generation starts. In this stage, some descendants of each group are assigned to change their forms from those of their parents. On account of the efficient convergence of this calculation due to the application of scientific principles, the ratio of the transformation is smaller in the top group than others, and in all groups, its value is much larger than that in the real world. Finally, the transformation is carried out by the mutation. The sites on which we impose the charge modification are chosen at random. We here have to note that just any transformation is not always allowed. In other words, unless they are shaped as living things, they cannot survive in the virtual world. In this calculation, one of the conditions to be a living thing is the charge neutrality of ionic crystals. Others are that they cannot have too large or too small charges and that the nearest neighboring ions have opposite charge. After all the above-stated procedures, the second generation is born. The same steps are repeated in their lives, and through this reiteration, species that develop prominent polarizability evolve.

5.3.3 Realization of prominent polarizability in a simple system

In this part, we shall discuss a practical example of the GA calculation. In regard to the simplification, the conditions below are attached.

- The form of each crystal is decided by the ion arrangement on the eight vertex sites which is shown in Fig. 5-3(a). The cube with the eight vertices represents the region of x, y, z ≥ 0 of 1 unit cell when the midst of a crystal is set as the origin. In terms of the STO single crystal, for example, it has the form shown in Fig. 5-3(b). Though this model is quite simple, we can treat not only perovskites but also many other structures such as rock-salt, face-centered, and body-centered structures.
- Ions have charge of integers from –2 to 4.
- The lattice constant is common and set around that of the STO single crystal of 4.0 Å no matter what kind of arrangement is occurred.
- Polarizability of ions, α, is proportional to ionic charge, that is to say, electronic polarizability, α_{ele}, is zero and only ionic polarizability, α_{ion}, is concerned (i.e., $\alpha = \alpha_{ion} = M \times |Q|$, where M is the coefficient of ionic polarizability and Q is the charge of ions as explained in Chapter 2).
- The polarization correction introduced in the Subsection 2.4.2 with the consideration of interatomic potential is not taken because the lattice constant is kept constant in the model.

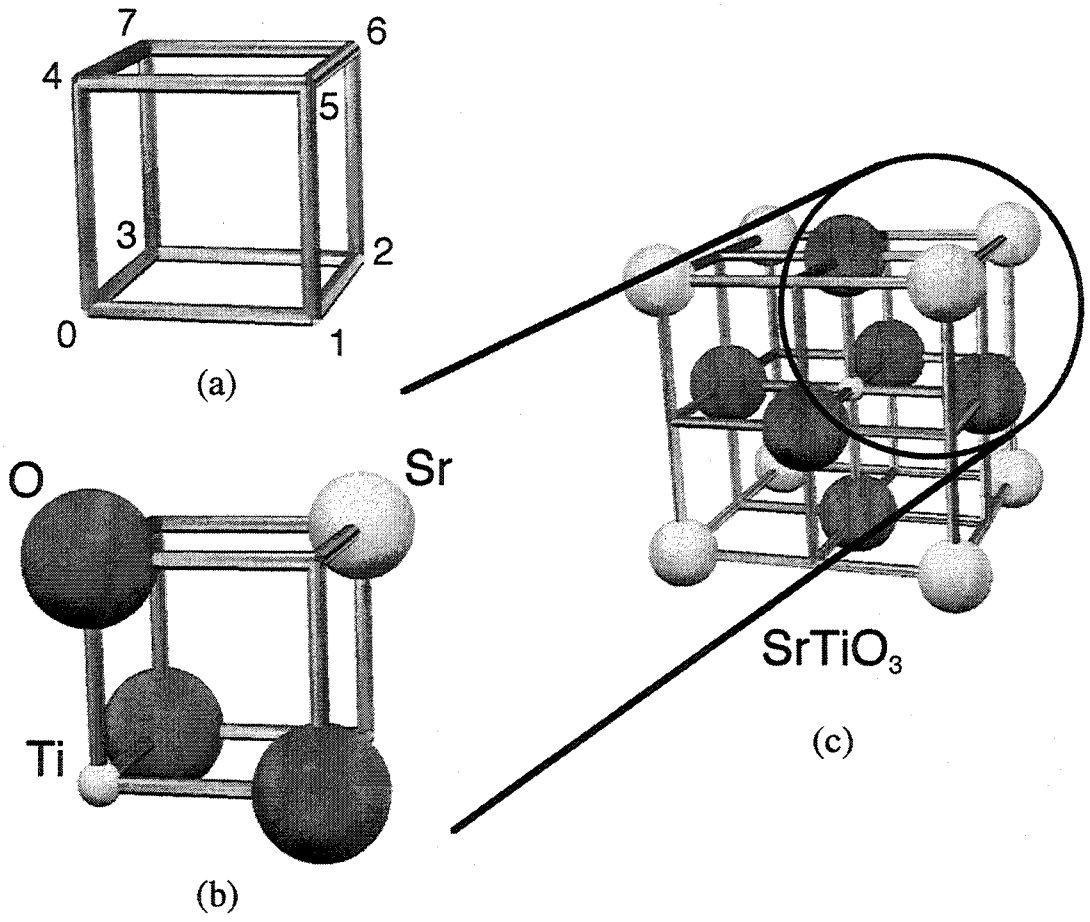

Fig. 5-3 Form of species of crystal. (a) Cubic frame of crystal form which is taken in the region of x, y, z ≥ 0, where the numbers represent each site and the site 0 is the center of crystals. (b) In the case of ideal STO, and (c) its unit cell in the complete form.

The evolutional transition which is calculated under these conditions is depicted in Figs. 5-4 and 5-5 where the total number of groups and individuals are set 100 and 1000, respectively. The coefficient of ionic polarizability, *M*, is set 0.56 and is common for all crystals in the calculation. This value is adjusted in order to obtain an appropriate permittivity for the ideal STO single crystal, and its obtained permittivity is 23.9. Although the permittivity looks small, it is purposely set smaller in order to carry out this discussion within a range where calculated permittivity does not diverge because the favorably polarizable crystals still have higher permittivity with smaller *M* and the derived permittivity

itself does not have realistic meaning in the calculation of this simplified model. In other words, we shall primarily fix our eyes upon what kind of arrangement the excellent crystals have. In Fig. 5-4, the transition of the number of individuals in the top five groups is shown. The numbers drastically change in each period, however, the top group steadily increase its constituent members. In Fig. 5-5, transition of adaptability (permittivity) of the top five groups is depicted. We can see that this virtual crystal world reached a stable state and achieved a superb polarization property in a short period.

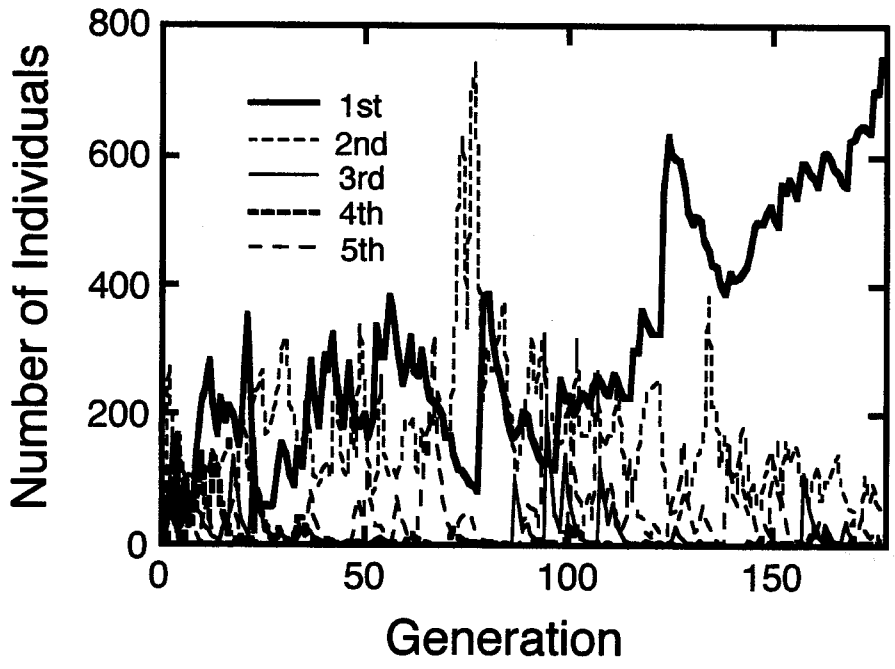

Fig. 5-4 Transition of number of individuals in the top five groups.

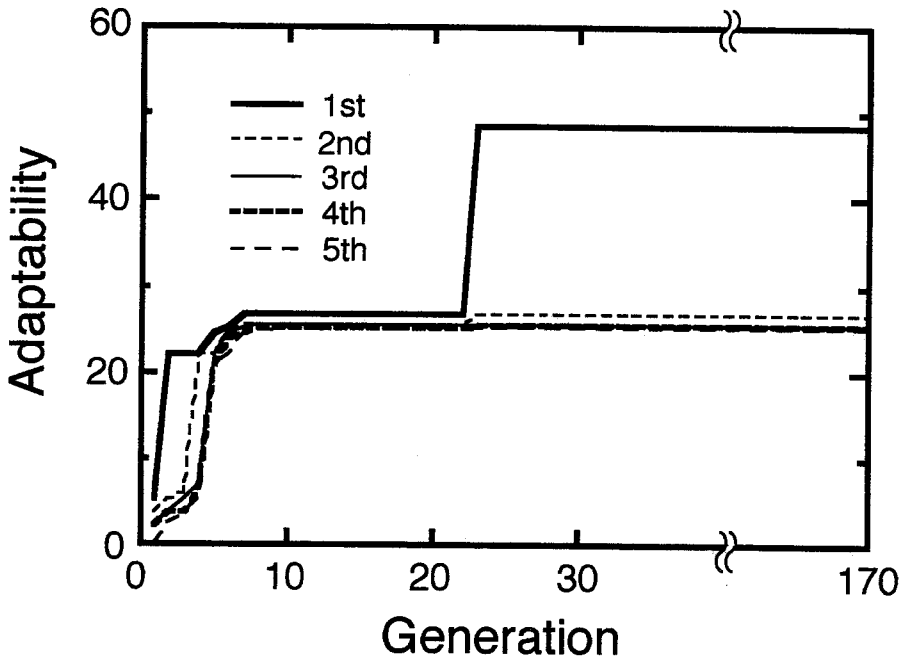

Fig. 5-5 Transition of adaptability of the top five groups.

Crystal characteristics of the top five groups are illustrated in Fig. 5-6. In this simple model, all of these five groups are superior to STO crystal. What kind of features do they have? Let us look at the top group first. If we regard the ions with a charge of +4 and –2 as Ti and O, respectively, we can see that this crystal is constructed as a multiple structure of Ti-O_6 octahedron, which includes as many as two Ti-O_a chains that are able to polarize efficiently with the positive feedback mechanism as explained above. Practically, the permittivity of the crystal is about twice as large as that of ideal STO. As for the group from no.2 to no.4, they have the same ion arrangement, however, they are treated as distinct groups because of the directional difference of the applied electric field. No matter what group we take a look at, the arrangement of the ion with charge of +4 on the site 0 and the ions with charge of –2 on the sites of 1, 3, 4, and 6 is identical among these five groups. Because the polarizability is proportional to the absolute value of ionic charge and charges of +2 and –2 contribute equally to permittivity in this model, we can understand that they exactly include the perovskite structure when we regard the ion on site 6 as Sr ion with charge +2 and the ions

with charge of +4 and −2 as Ti and O ions, respectively. The reason why these top five groups can show superior polarization property to STO is some additional ions contained in the perovskite structure which are a source of polarization. Finally, we could conclude from the above discussions that it is represented again that the perovskite structure is quite suitable for prominent polarization properties.

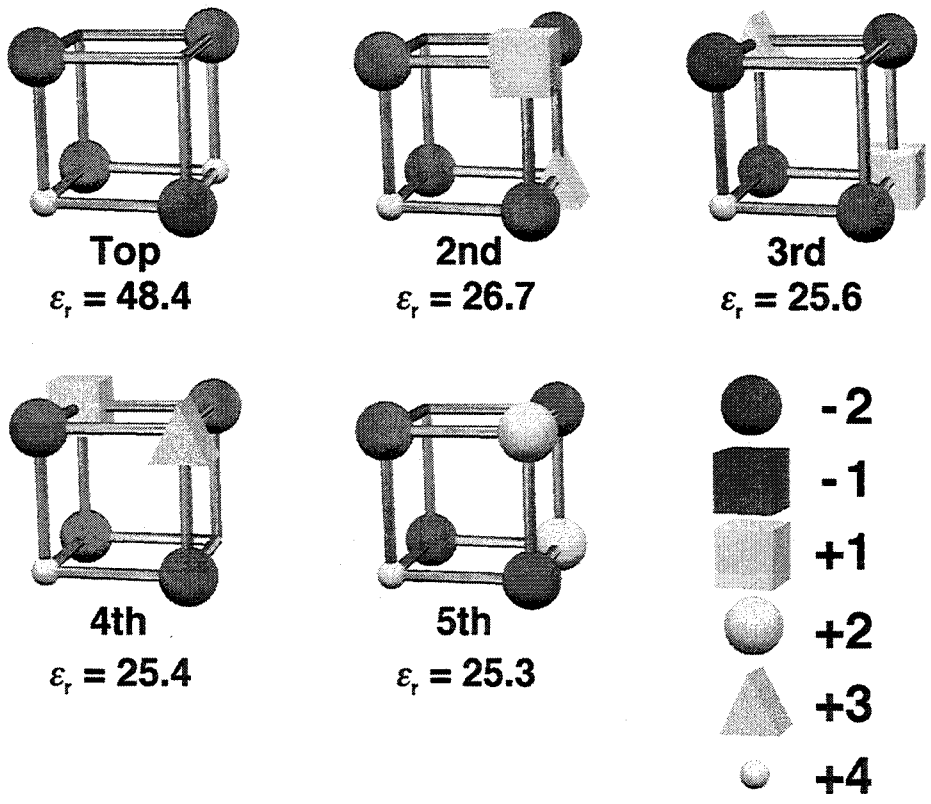

Fig. 5-6 Crystal characteristics of the top five groups.

In addition, let us discuss further important points. They are about the validity of results and the calculation time. In the GA calculation, it is very difficult to judge whether the obtained data is the best or not. In the present model, are the above-stated results of the top five groups really the best five among all thinkable cases? In order to work out the answer to the question, the author checked all possible cases and compared their permittivity one by one. Even the present simple model is quite troublesome and we have to treat a considerable number of crystal forms. There are totally seven ion cases for each site in which an ion with charge of from –2 to +4 locates on it (six patterns) or no ion takes the place. Therefore, with eight vertex sites, we have to consider 7^8 = 5,764,801 cases as possible crystal forms. In terms of the top five groups, the results obtained by thoroughly systematic calculation reached a complete agreement with those of the above GA calculation. In short, the results of the GA calculation were truly the best five in this simplified model.

One more notable result is about the calculation time. These simulations were carried out on a personal computer with a Pentium 120 MHz CPU, and it took about 2,000 sec to check all possible cases. On the other hand, by using GA, it took less than 10 sec for the same best five groups to appear. This result tells us how desirable evolution is in nature as a strategy. Calculations which are more complicated and have a larger number of conceivable cases will, in the future, benefit greatly from this high efficiency.

5.3.4 Results and discussion of crystals with real ions

Let us here examine the GA calculation on systems with real ions next. Considered ions are as follows: O^{2-}, Cl^{1-}, K^{1+}, Sr^{2+}, and Ti^{4+}. Although the fundamental way of thinking is the same as the above simplified model, for a stricter discussion, the lattice constant of each crystal is deduced by the calculation of stable structure as explained in Chapter 2. Moreover, in terms of the derivation of permittivity, the polarization correction with the interatomic potential is taken into account as well as the electronic polarizability. In short, the

permittivity calculation manner is just the same as in Chapter 2. The author has to mention one more revision in the present case. This concerns mutation. We shall add a new condition of living things, which is that the charge neutrality is kept in each layer vertical to the z-axis in all crystals. This stipulation takes into account the fact that, in the future, we would like to perfect treated crystal structures in practical thin films by the layer-by-layer growth technique.

As for the coefficient of polarizability, M, there are some species whose permittivity diverge with a small M. Their polarization property transforms to a distinct one with a little bit larger M (the divergence of permittivity corresponds to the ferroelectric phase transition). Their potential as an outstandingly polarizable material is high, and not to overlook them, M is set three types of smaller values of 0.02, 0.10, and 0.17 than that of in Chapter 2.

The obtained characteristics of the top five groups for each M are shown in Fig. 5-7 and Table 5-1. The notable points from the results are as follows,

- The ideal STO crystal is included among the top five groups in all cases (Group 2),
- About half of those of higher-ranked groups have perovskite or related structures (Group 1, 2, 3, 6, and 7),
- In regard to other highly polarizable crystals, the fact that ion dislocation is easier due to the asymmetry is a common feature.

According to the above results, we could say that the key to superb permittivity is not only having the perovskite structure, but also the easiness of ion dislocation on the axes along to the direction of the electric field. It is indicated that asymmetric crystal structures have a higher possibility of having such ion chains which vigorously contribute to the polarization rather than symmetric and uniform crystal structures.

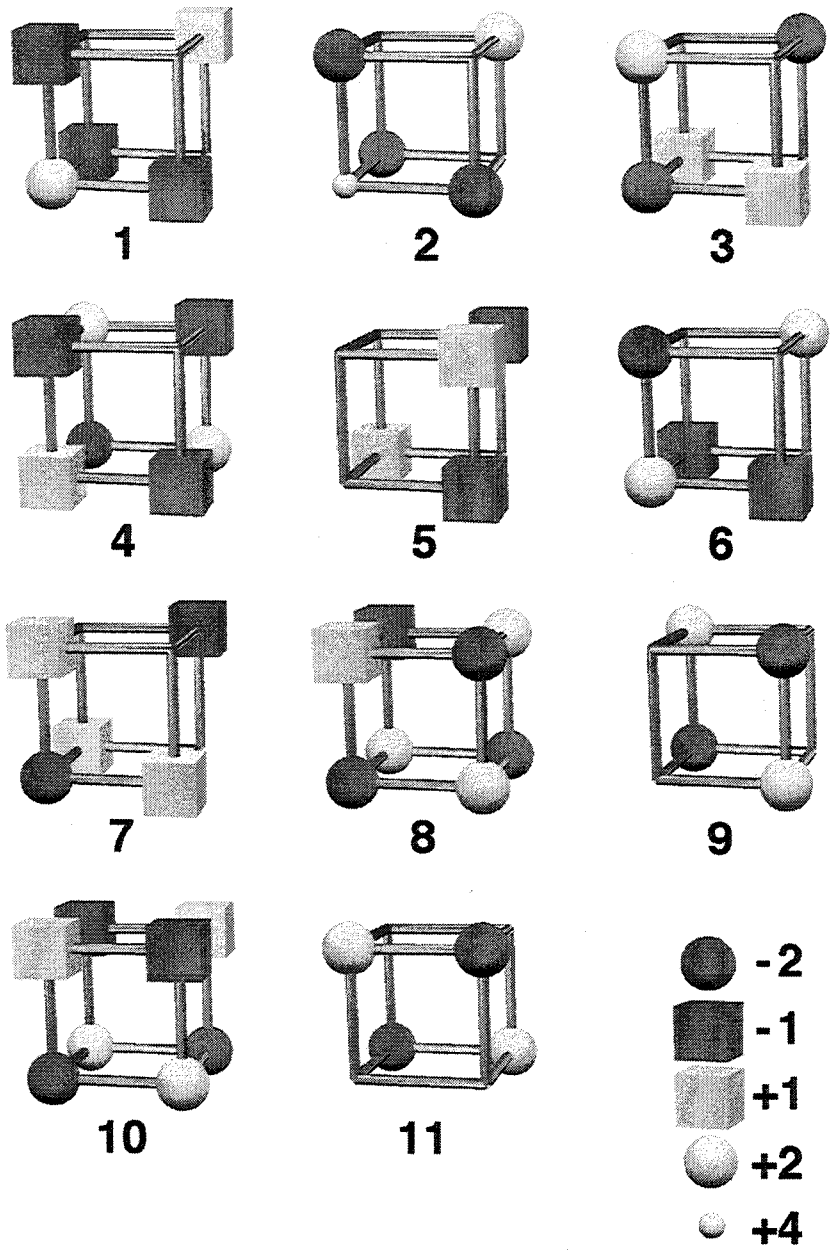

Fig. 5-7 Schematic view of grown prominent species of crystal.

Table 5-1 Calculated permittivities of the top five groups in each calculation.

M	Group										
	1	2	3	4	5	6	7	8	9	10	11
0.02	70	6.5	4.5	4.0	3.9	---	---	---	---	---	---
0.10	---	11	---	---	---	59	7.6	7.0	4.9	---	---
0.17	---	38	---	---	---	---	---	90	6.2	9.2	6.2

5.3.5 For further discussion

This part is an additional discussion in which several points that we must consider are summarized for the improvement of GA calculation in the future. Some strategies to elaborate the present calculation are listed below:

- Not to kill all members of the lower-ranked groups. Some of them should survive even if the number is small because there is a possibility they may transform themselves into an outstanding species with just a little modification of their forms.
- To introduce the notion of the gene crossover and enhance the convergence.
- To discuss strictly whether it is possible or not to practically fabricate the crystals which are treated in the calculation.
- To introduce an "operator" which shows the way to desirable systems in the transformation procedure. The concept such as artificial intelligence (AI) is included.
- To enlarge the size of crystal and make it possible to treat complex structures such as the fluorite structure, zinc-blend structure, and so on.
- To accept the transition of ionic characteristics according to the bonds inside the crystals. In order to accomplish this request, the introduction of the consideration of ionicity and/or the MO calculation can be one of the solutions.
- Not to restrict the number of groups and individuals. In other word, to make the situation close to the real world which is an open system.

5.4 Proposal for New Materials with Prominent Polarizability

In this section, favorable future approaches for new materials with prominent polarizability are proposed. Broadly considered, there are two proposals.

The first one is the realization of a structure in which ionic polarizations are enhanced by one another through a positive-feedback-like mechanism as in the perovskite structure,

which was described in Section 5.2 and Subsection 5.3.4. The author has an idea in terms of this point to improve polarization properties. It is the realization of multiple positive feedback loops inside a structure, and it may be achieved by the introduction of the concept of *fractals*. Fractal is the geometrical pattern, and we always see the same design on it no matter how large or small the areas are that we look at.[11] In the future, if the localized charge distribution and the inequitable local electric field are purposely realized in a crystal as we hope, a micro-sized positive feedback loop can be embedded inside a macro-sized positive feedback loop, and we can expect higher polarization due to the synergy.

The second proposal is the realization of a structure in which it is easy for ions to dislocate on the axes parallel to the applied electric field. It has been indicated in the last section that asymmetric crystal structures have a higher possibility of having such ion chains which vigorously contribute to the polarization rather than symmetric and uniform crystal structures. In the symmetric structures, the looseness of the ionic bonds is distributed equally, and as a result, it leads the densely packed structure and makes the ion dislocation difficult. We can easily comprehend the second proposal with the comparison of the three perovskites, $CaTiO_3$ (CTO), STO, $BaTiO_3$ (BTO). Although the main contributor to the polarization in these crystals is Ti-O_a, a chain which is common among them, the polarization properties at room temperature is experimentally in the order of CTO < STO < BTO.[12] The polarization disparity seems to be explained by the difference of ionic radius among three alkaline-earth metals, Cr, Sr, and Ba, which locate on the A-site. In other words, in the BTO single crystal with the greatest polarizability, the perovskite lattices are expanded by the Ba ions which have the largest ionic radius among these three elements, and consequently, it becomes easier for Ti and O_a ions to move. Strictly speaking, we must consider that many causes are involved, of course, because the shape of these three crystals (CTO, STO, and BTO) are different (orthorhombic, cubic, and tetragonal, respectively). However, this interpretation still seems not to be too far from the truth.

The author hopes these two proposals will contribute to the creation of new materials in the future.

5.5 Summary

In this chapter, the possibility of higher polarization properties was examined on the basis of the concept of evolution, and two proposals as a future approach for the creation of new materials were presented.

Firstly, the origin of the superb polarization properties of perovskites was investigated and a guideline was given to the quest for new materials.

Secondly, the GA program of the quest was produced and investigated, whose application to the polarizable substances was originally proposed by the author. The obtained ion arrangements of the top five groups in the simplified crystal model calculation were completely identical to the results of the thoroughly systematic calculation in which all possible cases were examined. Moreover, there was a huge gap of as much as two hundred times about the total calculation time between the two calculations. These facts support the effectiveness of the GA.

Thirdly, the simulation where real ions are considered was carried out. In this case, the stable structures of each crystal were calculated by using the two-body central force interatomic potential, and their permittivities were computed in the same manner of Chapter 2, in which the correction according to the ease of each ion dislocation in the interatomic potential was considered.

Finally, two proposals for the creation of new materials were given on the basis of the features of the obtained highly polarizable materials in these two representative cases. The first proposal is the realization of a structure in which ionic polarizations enhance one another through a positive-feedback-like mechanism as in the perovskite structure. The second one is the realization of a structure in which it is easy for ions to dislocate on the axes parallel to the applied electric field. It was indicated that such desirable structures may be accomplished with asymmetric crystal structures rather than with symmetric and uniform crystal structures.

References

(1) E. N. Bunting, G. R. Shelton, and A. S. Creamer, J. Am. Ceram. Soc. **30**, 114 (1947).

(2) J. G. Bednorz, and K. A. Müller, Phys. Rev. Lett. **52**, 2289 (1984).

(3) H. Tabata, H. Tanaka, and T. Kawai, Appl. Phys. Lett. **65**, 1970 (1994).

(4) D. L. Decker, and Y. X. Zhao, Phys. Rev. **B39**, 2432 (1989).

(5) R. Amirez, M. F. Lapena, and J. A. Gonzalo, Phys. Rev. **B42**, 2604 (1990).

(6) J. C. Slater, Phys. Rev. **78**, 748 (1950).

(7) M. Yoshinari, S. Tonegawa, H. Kitano, G. Matsumoto, T. Yoroh, *Kokoro to Computer* (Mind and Computer) (Just System Ltd., Tokyo, 1995) p.128 [in Japanese].

(8) H. M. Cartwright, *Application of Artificial Intelligence in Chemistry* (Oxford Publishing Ltd., New York, 1993).

(9) R. Belew, and B. Lashon, eds., *Genetic Algorithm in Search, Optimization, and Machine Learning* (Morgan Kaufmann, San Francisco, 1991).

(10) J. H. Holland, "Genetic Algorithms", Scientific American, July 1992, p.66.

(11) B. Mandelbrot, *The Fractal Geometry of Nature* (W. H. Freeman, San Francisco, 1982).

(12) *Landolt-B rnstein New Series* III/16a, Editor in Chief: K.-H. Hellwege (Springer-Verlag, New York, 1981).

Chapter 6
CONCLUSIONS

The principal results obtained in this thesis work on growth and prominent polarization properties of STO thin films are summarized as follows:

(1) Correlation between the structure and the polarization property of STO was investigated from the microscopic view with representative cases in the thin film fabrication: STO contains oxygen vacancies and unintentional structures aside from the perovskite due to the insufficient oxidation and the nonstoichiometry, respectively. Stable structures of these two cases were calculated by concerning the two-body central force interatomic potential. As for the oxygen-deficient structure, the lattice constant showed an inclination of stretching when the oxygen deficiency increased, which led to a conclusion that the reduction of the Coulomb force influences more than the decrease of the short-range repulsion force on the stabilization of the STO structures as oxygen deficiency takes place. This computation result of the inclination upheld the experimental fact. In regard to the STO crystal that holds the sliding-in Sr-O planes, the calculated lattice in the vicinity of the sliding-in Sr-O plane was slightly distorted as in the experimental result. (Chapter 2)

(2) On the basis of the validity of the permittivity derivation of well-known substances with the corrections of the local field and the ease of each ion dislocation in the interatomic potential, the permittivities of the above-obtained STO crystals were calculated. The calculated results indicated that the polarization property is degraded as the STO structure diverts from the ideal perovskite. Furthermore, the discussion about the ionicity was carried out in an unprecedented manner with the calculation of this work. It disclosed that the bonds in the perovskite structure are not completely ionic in the least, but covalent to a large extent. It was not inconsistent with the result of the improved calculation which employs the theory of MOs, and proposed the possibility for further investigations in the future. These above results led to the conclusion that there is an intimate relationship between the structure of

STO crystals and their polarization properties even in the microscopic view, and the perovskite structure has the key to the excellent polarizability of the ideal STO crystal. (Chapter 2)

(3) For the STO thin film growth, two substrate materials, YBCO and Pt, were fabricated on (100)MgO single crystals. In order to obtain high quality YBCO films, the MgO single crystals were annealed in oxygen ambient at 1000 °C for 7 hours prior to the YBCO deposition. On the other hand, fine epitaxial Pt films were grown successfully on both (100)MgO single crystals which were pre-oxygen-annealed and non-annealed. Moreover, an interesting relationship between the orientation of epitaxial Pt thin films and the treatment of MgO substrates was disclosed: (111)-oriented Pt films are grown on oxygen-annealed MgO substrates, and on the other hand, (100)-oriented Pt films on non-annealed substrates. This work is first to reveal that the orientation of Pt films changes on (100)MgO single crystals with and without the pre-annealing treatment even when the deposition temperatures are identical. (Chapter 3)

(4) To the conventional PLD method which has the intrinsic problem of particles and/or droplets, an innovative technique, the eclipse method, which uses a shadow mask placed between the target and the substrate was proposed. Despite the simpleness of the eclipse method, it completely solve the problem and led to a remarkable improvement in the surface smoothness of the STO thin films. Moreover, it led to a striking enhancement in the success probability of the capacitance observation. (Chapter 3)

(5) Epitaxy of the STO thin films was examined by the XRD and the RHEED methods. Although the STO thin film grown by the eclipse PLD method on (100)Pt did not possess the long-range lattice ordering, it showed the fine (100)-oriented epitaxial growth. On the other hand, both of the STO thin films grown by the rf magnetron sputtering on (100) and (111)-oriented Pt films included a small amount of (110)-oriented composite. However, the STO thin film on (100)Pt substrate exhibited the almost complete streak pattern which indicated the two-dimensional growth in which long-distance ordering was kept. (Chapter 3)

(6) Optical properties of the grown STO thin films were investigated by the RAS which is

one of the most powerful techniques for thin film measurement. On the basis of the fact that the absorption peak intensity and sharpness reflect the crystallinity of thin films and also become the measure of the quality of polarization properties, the interfacial information between the Pt substrates and the STO films was obtained by attempting to reduce the film thickness of the STOs. The observed spectra suggested the existence of the degraded layer on the interface. (Chapter 4)

(7) Electrical properties of the grown STO thin films were investigated by the measurement of the *C-V* curves, and they indicated the internal electric field dependence of permittivity which became greatest with a zero internal field. The permittivity of the STO thin films reached as high as $370\varepsilon_0$ at room temperature. By means of the phenomenological treatment, it was disclosed that the induced charge could reach almost 10^{14} cm^{-2}, which is two orders higher than in familiar semiconductors. In addition, it became clear that the band diagram which has no space charge is appropriate for the description of the Cr/(100)STO/Pt MIM' structure. (Chapter 4)

(8) Possibility for higher polarization properties was examined with GA whose application to the polarizable materials was proposed by the author on the basis of the concept of evolution. Two approaches for the creation of new materials were proposed according to the features of the obtained highly polarizable materials. The first one is the realization of a structure in which ionic polarizations enhance one another through the positive-feedback-like mechanism as in the perovskite structure. The second one is the realization of a structure in which it is easy for ions to dislocate on the axes parallel to the applied electric field. It was indicated that such desirable structures may be accomplished with asymmetric crystal structures rather than with symmetric and uniform crystal structures. (Chapter 5)

VITA

Mamoru IWABUCHI was born in Kagawa, Japan, on October 22, 1970. He graduated from Tsu High School, Mie, Japan, and entered Osaka University, Osaka, Japan, majoring in electrical engineering in 1989. He skipped the fourth grade of the Bachelor course, and entered the Graduate School in 1992. He received the M.S. degree from Osaka University in 1994. He has been engaged in the investigation of high-temperature superconducting MIS (metal-insulator-superconductor) structure, the epitaxial growth of thin films, and the analysis of the prominent polarization properties of strontium titanate. He is a member of the Japan Society of Applied Physics and the Japan Chemistry Program Exchange.

LIST OF PUBLICATIONS

I. FULL PAPERS

1. M. Iwabuchi, T. Fujii, and T. Kobayashi:
"Photo- and Electron-Beam-Induced Currents from Epitaxial $YBa_2Cu_3O_y$ Metal-Insulator-Superconductor (MIS) Structure in the Normal State",
Jpn. J. Appl. Phys. **32**, L491 (1993).

2. M. Iwabuchi, K. Kinoshita, H. Ishibashi, and T. Kobayashi:
"Reduction of Pin-hole Leakage Current of $SrTiO_3$ Films by ArF Excimer Laser Deposition with Shadow Mask ("Eclipse Method")",
Jpn. J. Appl. Phys. **33**, L610 (1994).

3. M. Iwabuchi, and T. Kobayashi:
"Growth and characterization of epitaxial $SrTiO_3$ thin films with prominent polarizability",
J. Appl. Phys. **75**, 5295 (1994).

4. T. Kobayashi, T. Ariki, M. Iwabuchi, T. Maki, S. Shikama, and S. Suzuki:
"Analytical studies on multiple delta doping in diamond thin films for efficient hole excitation and conductivity enhancement",
J. Appl. Phys. **76**, 1977 (1994).

II. INTERNATIONAL CONFERENCE

1. M. Iwabuchi, T. Fujii, and T. Kobayashi:
"Photo-Response of $YBa_2Cu_3O_y$ MIS Structure",
Advances in Superconductivity V, Y. Bando, and H. Yamauchi (Eds.),
Proceeding of the 5th International Symposium on Superconductivity (ISS '92), 1169 (Springer-Verlag, Tokyo, 1993).

2. M. Iwabuchi, K. Matsui, M. Taga, and T. Kobayashi:
"Growth and characterization of epitaxial $SrTiO_3$ thin films with supereminent polarizability",
Advanced Materials '93, I/B, *Proc. of 3rd IUMRS Advanced Materials, Tokyo, 1993*, Trans. Mat. Res. Soc. Jpn. **14B**, 1647, (Elsevier Science B. V., Amsterdam, 1994).

3. M. Iwabuchi, H. Kobayashi, T. Ashida, M. Taga, and T. Kobayashi:
"Electron-Beam-Induced-Current (EBIC) Image of YBaCuO-MISFETs with $Ba_xSr_{1-x}TiO_3$ Ferroelectric Gate Insulator",
Advanced Materials '93, VI/A, *Proc. of 3rd IUMRS Advanced Materials, Tokyo, 1993*, Trans. Mat. Res. Soc. Jpn. **19A**, 555, (Elsevier Science B. V., Amsterdam, 1994).

4. T. Kobayashi, T. Ashida, M. Taga, and M. Iwabuchi:
"IMPROVED INTERFACE IN YBCO-MISFETs BY $SrTiO_3/BaTiO_3$ COMPOSITE GATE INSULATOR",
FED-136, Extended Abstracts, INTERNATIONAL WORKSHOP ON HIGH-TEMPERATURE SUPERCONDUCTING ELECTRON DEVICES, Whistler, British Columbia, Canada (1994), p.74.

5. M. Iwabuchi, K. Kinoshita, and T. Kobayashi:
"INNOVATIVE LASER DEPOSITION TECHNIQUE WITH SHADOW MASK ("ECLIPSE METHOD") SUITABLE FOR PREPARATION OF HTSC-MIS AND LAYERED STRUCTURE",
FED-136, Extended Abstracts, INTERNATIONAL WORKSHOP ON HIGH-TEMPERATURE SUPERCONDUCTING ELECTRON DEVICES, Whistler, British Columbia, Canada (1994), p.96.

III. REVIEW PAPERS

1. T. Kobayashi, K. Matsui, and M. Iwabuchi:
"Electric field effect in YBaCuO thin films"
OYO BUTSURI (Applied Physics) **62**, 471 (1993) [in Japanese].

2. M. Iwabuchi, and T. Kobayashi:
"Special Issue : *For Future Applications of Superconductors*, I. New Electronic Devices with Superconductors",
J. IEE Japan **114**, 214 (1994) [in Japanese].

IV. DOMESTIC CONFERENCE

1. M. Iwabuchi, T. Fujii, and T. Kobayashi:
"Al/$SrTiO_3$/YBaCuO MIS Structure : Photo Response Properties",
Extended Abstracts (The 53rd Autumn Meeting, 1992); The Japan Society of Applied Physics No.1, p.136 [in Japanese].

2. M. Iwabuchi, T. Ashida, T. Fujii, and T. Kobayashi:
"Al/$SrTiO_3$/YBaCuO MIS Structure : Investigation by EBIC (Electron-Beam-Induced-Current)",
Extended Abstracts (The 40th Spring Meeting, 1993); The Japan Society of Applied Physics and Related Societies No.1, p.139 [in Japanese].

3. M. Iwabuchi, K. Matsui, M. Taga, and T. Kobayashi:
"Fabrication and Electrical Properties of Highly Dielectric Epitaxial $SrTiO_3$ Thin Films",
Extended Abstracts (The 40th Spring Meeting, 1993); The Japan Society of Applied Physics and Related Societies No.2, p.482 [in Japanese].

4. M. Iwabuchi, T. Ashida, and T. Kobayashi:
"Fabrication of Epitaxial $YBa_2Cu_3O_y$-MISFET (VIII) ~ EBIC Change of YBCO-MIS Structure with Applied Biases ~",
Extended Abstracts (The 54th Autumn Meeting, 1993); The Japan Society of Applied Physics No.1, p.138 [in Japanese].

5. T. Ashida, M. Iwabuchi, and T. Kobayashi:
"Fabrication of Epitaxial $YBa_2Cu_3O_y$-MISFET (IX) ~ Advantage of using $BaTiO_3$ as a buffer layer ~",
Extended Abstracts (The 54th Autumn Meeting, 1993); The Japan Society of Applied Physics No.1, p.139 [in Japanese].

6. Y. Sakaguchi, M. Iwabuchi, and T. Kobayashi:
"Fabrication of Epitaxial $YBa_2Cu_3O_y$-MISFET (XI) ~ Fabrication of $BaTiO_3$-$SrTiO_3$ Superlattice Gate ~",
Extended Abstracts (The 54th Autumn Meeting, 1993); The Japan Society of Applied Physics No.1, p.139 [in Japanese].

7. M. Iwabuchi, K. Matsui, and T. Kobayashi:
"Correlation between Fourier-Transform-Infrared (FTIR) Spectra and Dielectric Properties of Epitaxial $SrTiO_3$ Thin Films",
Extended Abstracts (The 54th Autumn Meeting, 1993); The Japan Society of Applied Physics No.2, p.445 [in Japanese].

8. M. Iwabuchi, Y. Sakaguchi, and T. Kobayashi:
"Fabrication and Characterization of $(SrTiO_3)_m$-$(BaTiO_3)_n$ Superlattice",
Extended Abstracts (The 54th Autumn Meeting, 1993); The Japan Society of Applied Physics No.2, p.445 [in Japanese].

9. M. Iwabuchi, T. Ashida, and T. Kobayashi:
"Growth and Characterization of Epitaxial $SrTiO_3$ Thin Films with Prominent Polarizability",
TECHNICAL REPORT OF IEICE, SCE-93-44, 79 (1993).

10. M. Iwabuchi, K. Okumura, and T. Kobayashi:
"Fabrication and Characterization of $(SrTiO_3)_m$-$(BaTiO_3)_n$ Superlattice (II) ~ Thin Film Growth by Eclipse PLD and Evaluation of Interfaces ~",
Extended Abstracts (The 41st Spring Meeting, 1994); The Japan Society of Applied Physics and Related Societies No.2, p.375 [in Japanese].

11. M. Iwabuchi:
"Effect of Excimer Laser Anneal on $SrTiO_3$ Thin Films (IV) ~ Analysis of Laser Anneal with Internal Stress ~",
Extended Abstracts (The 55th Autumn Meeting, 1994); The Japan Society of Applied Physics No.2, p.349 [in Japanese].

12. M. Iwabuchi, and T. Kobayashi:
"Quest for New Material of High Polarizability with Learning Algorithm",
Extended Abstracts (The 56th Autumn Meeting, 1995); The Japan Society of Applied Physics No.1, p.72 [in Japanese].

13. M. Iwabuchi, T. Kashiwai, and T. Kobayashi:
"Analysis of Polarization Properties and Structure of $SrTiO_3$ Thin Films using Density Functional Theory",
Extended Abstracts (The 43rd Spring Meeting, 1996); The Japan Society of Applied Physics and Related Societies No.2, p.413 [in Japanese].

15. M. Iwabuchi, T. Kashiwai, and T. Kobayashi:
"Analysis of Polarization Properties and Structure of $SrTiO_3$ Crystal"
Extended Abstracts of The 13th Meeting of Ferroelectric Materials and Their Applications (FMA-13), Kyoto, p.165 (1996) [in Japanese].

16. M. Noda, M. Yoshida, M. Tachiki, M. Iwabuchi, and T. Kobayashi:
"Preparation of $La_xSr_{1-x}TiO_3$ Thin Films by Laser Ablation Method",
Extended Abstracts (The 44th Spring Meeting, 1997); The Japan Society of Applied Physics and Related Societies, to be published [in Japanese].